UNIVERSITY OF SOUTHAMPTON

Mechanical properties of woodpile lattice materials fabricated using additive manufacturing

by

Enrique Cuan Urquizo

A thesis submitted in partial fulfillment for the
degree of Doctor of Philosophy

in the
Faculty of Engineering and the Environment
Computational and Engineering Design research group

March 2017

UNIVERSITY OF SOUTHAMPTON

Abstract

Faculty of Engineering and the Environment
Computational and Engineering Design research group

Doctor of Philosophy

by Enrique Cuan Urquizo

The relationship between the structure and the property of lattice materials and structures fabricated using fused filament fabrication process is studied analytically, computationally and experimentally. Lattices with specified structural parameters were fabricated in a controlled manner using customised G-codes that generate the tool path as desired. The characterisation of the parent material to fabricate lattices was carried out by tensile testing of single filaments. Single filament properties were then used to predict the response of woodpile lattice bars in tension, when the loading direction is along the filaments. Good agreement with experimental measurements was observed.

Following the simplest loading case of tension along the fibres, more complex scenarios of structures made of filaments in woodpile arrangement under bending and torsion were considered. It was shown that woodpile beams in flexure, as opposed to solid beams, are extremely sensitive to shear deformation. The contributions of the bending and shear stiffness were identified and analytical models were developed to account for these two primary mechanisms of filament deformation. The apparent shear of the woodpile lattice resulted to be dominated by the bending of the individual filaments. An analytical expression for the apparent shear modulus of lattice beams was derived on the basis of filament bending. Contribution from apparent bending and apparent shear in the transverse response of lattice beams was quantitatively brought out. The twist of beams in woodpile arrangement was also studied. The deformation mechanism was identified as twist and flexure of the filaments. The torsional stiffness found to be extremely sensitive to the amount of overlap at the location of bonding between filaments. Analytical models for displacement-only-constraint and displacement and relative rotation constraints were developed.

The compressive response along the stacking direction of structures in woodpile arrangement was also studied. The so-called aligned and the staggered stacking of filaments was considered. While the compression of the staggered arrangement resulted to be bending-dominated, the aligned configuration is dominated by the elastic compression at each junction of filaments. Analytical models were derived accounting for filament flexure and discs diametrically compressed. Excellent agreement with numerical results was obtained.

Contents

List of Figures

List of Tables

Declaration of Authorship

I, ENRIQUE CUAN-URQUIZO, declare that this thesis titled, 'Mechanical properties of woodpile lattice materials fabricated using additive manufacturing' and the work presented in it are my own. I confirm that:

- This work was done wholly or mainly while in candidature for a research degree at this University.
- Where any part of this thesis has previously been submitted for a degree or any other qualification at this University or any other institution, this has been clearly stated.
- Where I have consulted the published work of others, this is always clearly attributed.
- Where I have quoted from the work of others, the source is always given. With the exception of such quotations, this thesis is entirely my own work.
- I have acknowledged all main sources of help.
- Where the thesis is based on work done by myself jointly with others, I have made clear exactly what was done by others and what I have contributed myself.

Signed: _____

Date: _____

Part of this work has been published in Journals:

- **Cuan-Urquizo, E.**, and Bhaskar, A. "Flexural Response of Lattice Beams Having Woodpile Architecture" (manuscript submitted to Mechanics of Materials)
- **Cuan-Urquizo, E.**, and Bhaskar, A. "Elastic properties of additively manufactured lattice materials: measurements and models" (manuscript under preparation to be submitted to Materials and Design).
- **Cuan-Urquizo, E.**, and Bhaskar, A. "Apparent Young's modulus of the woodpile lattice material along the stacking direction: aligned vs staggered arrangements" (manuscript under preparation to be submitted to International Journal of Mechanical Sciences)

And also in conferences:

- Bhaskar, A. and **Cuan-Urquizo E.**, "Long waves in lattice waveguides", ICCMS, IIT Bombay, Mumbai, India, June 27-July 1, 2016
- Bhaskar, A., A. Bonfanti and **E. Cuan-Urquizo**. "Bioresorbable Systems: The Role of Modelling and Simulation in Performance Assessment of Bio-Structures and Implants". 27th European Conference on Biomaterials - Krakow, Poland - 30 August - 3 September 2015.
- **Cuan-Urquizo, E.**, and Bhaskar, A. "Flexural properties of the additively manufactured porous material having woodpile architecture" - Topology Optimization for Additive Manufacturing I, ESMC, Madrid, July 2015.
- **Cuan-Urquizo, E.**, and Bhaskar, A. "Structure-property relationship of additively manufactured lattice materials: micromechanics and measurements" - 18th International Conference on Composite Structures, Lisbon Portugal June 2015
- **Cuan-Urquizo, E.**, Yang, S. and Bhaskar, A. "Mechanical characterisation of additively manufactured material having lattice microstructure" IOP Conference Series: Materials Science and Engineering (Volume 74, Issue 1, 012004).

"Science is not about building a body of known 'facts'. It is a method for asking awkward questions and subjecting them to a reality–check, thus avoiding the human tendency to believe whatever makes us feel good."

Terry Pratchett

Acknowledgements

Firstly, I wish to express my sincere gratitude to my supervisor and mentor Prof. Atul Bhaskar, for all the support, and knowledge shared. I honestly do not know someone else with such energy and passion for science, my most honest acknowledgements and admiration to him. I would also like to thank Prof. Shoufeng Yang for his useful comments to improve my work. I am very grateful to Dr Mariam Ghandchi Tehrani and Dr Jiye Chen for their very helpful review and comments. I would like to thank the members of the CED group. I would like to extend my gratitude to Dr Ernesto Rodriguez, Dr Armando Roman and Dr Raquel Cuevas for leading me to the scientific research field. The assistance provided by Dr Andy Robinson, Dr Mamadou Bah and Dr Alex Dickinson for my laboratory and computational work, is greatly appreciated. I wish to thank the contributors of my daily smiles at work Alba, Sharon and Inma.

I would like to thank my colleagues Andrii, Susan, Paby, Lana, Natalia, Giorgos, Jie, Ilya, Hayk, Chris, Kiki, and Ale for sharing with me uncountable concepts and suggestions. I owe my deepest gratitude to SUTKD, for making my UK adventure a true everlasting memory. For all those trainings, and friendship a special mention to David, Kate, Sarmi, Saf, Booker, Cliff, Lorene, Lorraine, James, Maria, Sylwia, Javiera, Natalie, Ben, Benoit, Hussain, Jay, Declan, Sophie, Sara, Owen, and the team. Thanks to the MexSoc, Miguel, Angeles, Daniel, Julio, Itzy for bring a piece of Mexico to Southampton. Thanks a lot also to Terry Pratchett and Neil Gaiman for creating so many worlds in which I hid when this thesis seemed too scary. I also owe so much to the people of 250 Burgess road, my other family, for being there every day to make me laugh, so thanks to Lalo, Ana, Anais and Gregorio. My deepest gratitude to all the friends I've made during this journey, Nalleli for all the books and music shared, Stephanie for always being there, Pedro and Carlos for being my brothers, Anie, Claudia, Jon, Lizbeth, Marcela, Alma, Diana, MariSol, Thalia, Valeria for taking care of me. Thanks also to those who were there when the adventure started and stayed until the end of it, Carla, Gaby, Laura, Maribel, Alina, Ana, Monica, Aldo, Jorge, Olague, Marifer, Georgia, and Barbara.

I cannot find words to express my gratitude to my family (Elisa, Enrique, Bebis, Fito, La Chata, Marco, Don Neto, Tichi, Gaby) for supporting and encouraging me to pursue this degree, but more important for their unconditional love. This thesis would be incomplete without a mention of the support given me by my love, Viridiana Tejada, to whom this thesis is also dedicated. Without her lifting me up when this thesis seemed interminable, I doubt it should ever have been completed.

Finally, the financial support from the Mexican Council of Science and Technology (CONACyT) during my graduate study is acknowledged.

Abbreviations

AM	**A**dditive **M**anufacturing
RP	**R**apid **P**rotyping
SFF	**S**olid **F**ree **F**abrication
LM	**L**ayered **M**anufacturing
3DP	**T**hree-**D**imensional **P**rinting
FDM	**F**used **D**eposition **M**odeling
FFF	**F**used **F**ilament **F**abrication
SLS	**S**elective **L**aser **S**intering
SLA	**S**tereolithography
SLS	**S**elective **L**aser **M**elting
EBM	**E**lectron **B**eam **M**elting
RC	**R**obocasting
ABS	**A**crylonitrile **B**utadiene **S**tyrene
PLA	**P**olylactic acid
TE	**T**issue **E**ngineering
SEM	**S**canning **E**lectron **M**icroscope
CAD	**C**omputer-**a**ided **d**esign
FEA	**F**inite **E**lement **A**nalysis
EB	**E**uler **B**ernoulli
NA	**N**eutral **A**xis
OL	**O**ver**l**ap

Symbols

ρ	density of the parent material
$\bar{\rho}$	relative density
V_s	volume of the solid
V_c	volume of the unit cell
λ_x	separation of the filaments along the X axis
λ_y	separation of the filaments along the Y axis
N_x	number of the filaments along the X axis
N_y	number of the filaments along the Y axis
N_z	number of layers
R	relative position of the filaments
r	radius of a filament
a	area of a filament and parameter to locate the force application point in a beam
A	total area
F	unit force
σ	stress
ε	strain
τ	shear stress
γ	shear strain
ν	Poisson's ratio
E	Young's modulus

$\langle E \rangle$	apparent Young's modulus
$\langle E \rangle_{\parallel}$	apparent Young's modulus along the filaments
$\langle E \rangle_{s}$	apparent Young's modulus of the staggered configuration
$\langle E \rangle_{a}$	apparent Young's modulus of the aligned configuration
G	shear modulus
$\langle G \rangle$	apparent shear modulus
$\langle G \rangle_{EB}$	apparent shear modulus with EB theory
$\langle G \rangle_{T}$	apparent shear modulus with Timoshenko theory
I	second moment of area
B	bending stiffness equal to EI
$\langle B \rangle$	apparent bending stiffness
κ	shear correction factor and curvature in beam bending
S	shear stiffness equal to κGA
$\langle S \rangle$	apparent shear influence in transverse deflection
J	torsional constant
$\langle GJ \rangle$	apparent torsional rigidity
δ	transverse displacement
θ	twist angle in torsion
α	twist rate in torsion
w	displacement in the z-axis
L	length of a beam or bar
ζ	local coordinate axis of the left beam in the periodic beam analysis
ξ	local coordinate axis of the right beam in the periodic beam analysis
U	strain energy

To Elisa, Enrique, Bebis, Fito, Viri and specially Macaria

Chapter 1

Introduction

Demanding applications have triggered innovation in material design and manufacture. Engineered materials are an example of this, because they can be used to create components with tailored mechanical properties. This can be achieved by controlling the distribution of matter within the component. Materials with micro-structures minimise the unnecessary use of material, by placing matter in locations only where it is needed. Frequently, such materials with microstructure are porous. Applications demanding porous materials are found in the fields of structural engineering, biomedical applications, and acoustics metamaterials. There are several fabrication processes to produce parts with prescribed degree of porosity. Additive manufacturing (AM) techniques possess the capability of depositing material in a controlled manner, making them a promising alternative to produce parts with desired mechanical properties. The areas of porous materials manufactured using additive manufacturing have inspired the present work. The motivation and the objectives of the research are presented in this chapter.

1.1 Motivation of the study

Additive manufacturing frequently produces parts with a certain degree of porosity. This is particularly true with components manufactured using fused filament fabrication (FFF), commonly known as fused deposition modelling (FDM). This is because the

AM-parts are composed of a lattice arrangement of material, which in turn results with voids in the part. AM techniques allow the production of parts with tailored mechanical properties, by controlling the distribution of matter throughout the part. An understanding of the effect of the microstructure on the resulting mechanical properties is limited. Microstructured materials are taken as an alternative to minimise the use of natural materials. Their inherent porosity also makes structured materials suitable for a aerospace, structural and biomedical applications. A section of human mandible made up of lattice material fabricated using additive manufacturing is shown in figure 1.1.

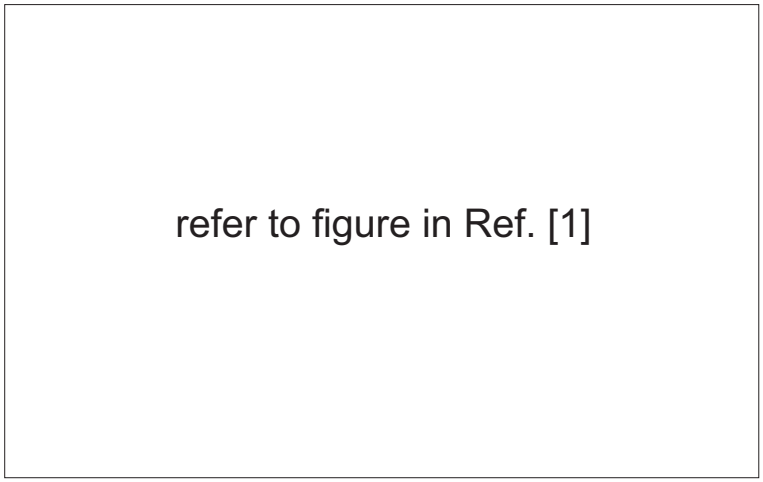

FIGURE 1.1: Additively manufactured section of human mandible composed of lattice material.. Figure from [1].

A motivation for the present work arises from the increasing interest in synthetic structural materials or engineered materials. The development of *engineered materials* is viewed a solution to the exhaustive use of natural resources and increase in demanding applications. Properties of such engineered materials with microstructure can be tailored easily. It is convenient to represent various material groups such as polymers, metals, honeycombs, foams, alloys or natural material belonging to the so called material kingdom on *material property maps*. Often known as Ashby maps–such as the one shown in figure 1.2. These maps contrast materials in a 2D plot with two properties (e.g. mechanical, thermal, etc.) in each axis [13]. In figure 1.2, each of the areas encircled represent the properties attainable by different material groups, on the Young's modulus-density plane.

One way to fabricate lighter materials with structural properties comparable to those of

metals or wood, is to introduce a certain degree of porosity. This will reduce the overall density. This appears to be an alternative to overcome the above mentioned issues. Porous materials possess an structured arrangement of matter. An intelligent use of these requires design, analysis and optimisation, of the resulting properties due to the porous structure. The use of these materials can be directly reflected in a reduction in the material used and in the consumption of resources. The gains are most significant when, as a designer, we require to fill a volume such as the core of a sandwich construction. Besides, voids are also beneficial in biomedical applications where cell proliferation and growth needs to be encouraged. The presence of voids results in properties that make them advantageous when compared to their homogeneous counterpart.

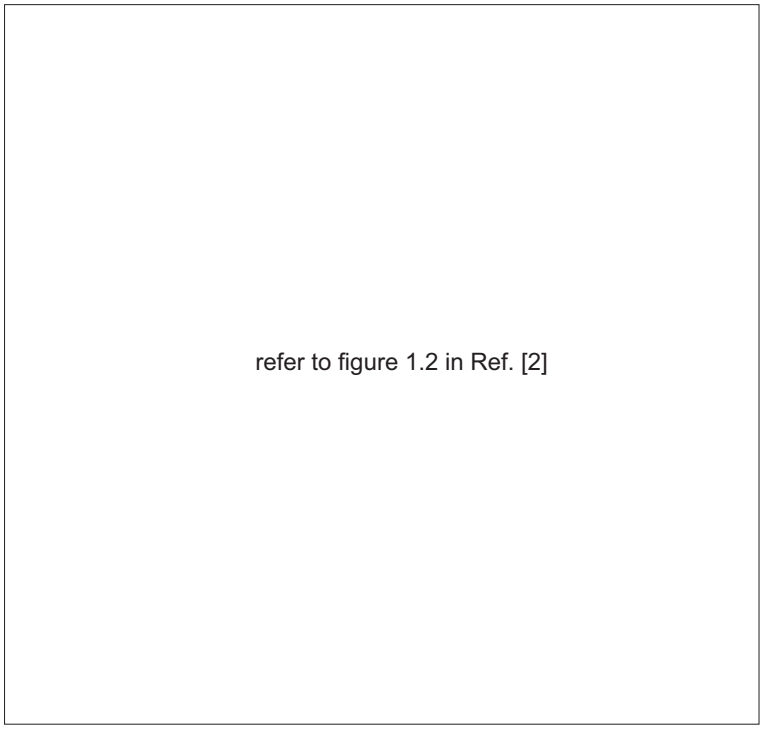

FIGURE 1.2: Material property chart of Young's modulus plotted vs the density. It shows the material attainable Young's modulus currently available. The blank spaces shows gaps where material with those properties is not available. Figure from [2].

The second motivation of the present work is the increasing use of AM as a fabrication technique. Some of the reasons behind this rapid change include an increase in manufacturing resolution, built volume, manufacturing speed, reduction in manufacturing cost, and advances in multiple material manufacturing [14]. While the idea has been around for over two decades, it is only now that many practical implementations have been feasible. Originally, these manufacturing technologies were known as *rapid prototyping*. A

reason for this is that they were traditionally used to produce parts in a mock-up or 3D shape models before the final and ready-to-use component, hence the name *prototype*. The current trend is to use components fabricated with these techniques for parts in service, rather than prototypes. This can only be feasible with a deep understanding of the resulting mechanical properties of the additively fabricated materials and components.

Parts fabricated with AM techniques, based on the extrusion of material, are often composed of an inner arrangement of extruded filaments. A section of an additively fabricated part is shown in figure 1.3. The arrangement of material significantly influences the mechanical properties of the fabricated part. This inner structure has voids, thus saving material used, reducing the weight of the printed component and also reducing the fabrication time. The porosity can be reduced by setting the parameters in order to fabricate a fully dense component. This brings the filaments closer to each other, but the stacking of these invariably results in voids. This makes components fabricated using AM to be composed of structured material arrangements, so that the effective properties will differ from those of the parent material. Such structured filler volumes inside printed parts are very commonly found in the printing strategies provided by many commercially available printers and the software that accompany them. This necessitates the study of the mechanical properties of parts fabricated with these processes. While there has been significant effort in improving the manufacturing procedures in order to achieve a variety of complex shapes of the manufactured parts, the understanding of the mechanical properties of materials and components thus manufactured remains limited. This arrangement of extruded material has huge impact on the resulting mechanical properties which is studied in this dissertation. In the next sections, an introduction to cellular and structured materials in a generic setting, followed by a review of the additive manufacturing of structured materials in Section 1.3, are presented.

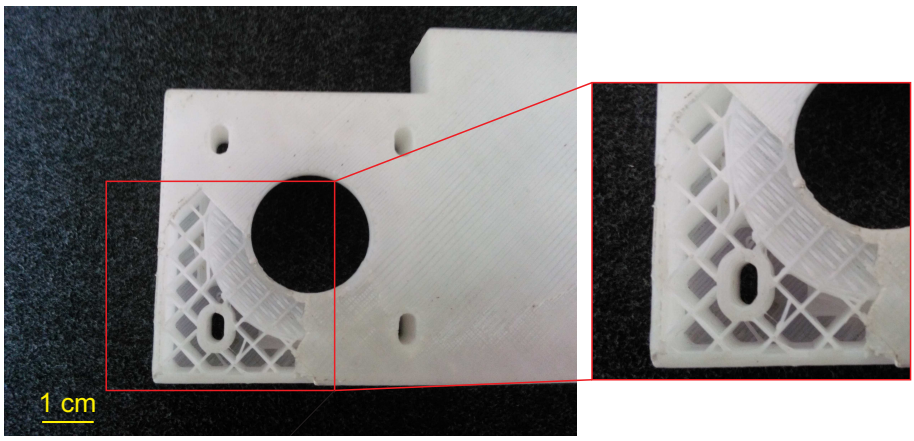

FIGURE 1.3: Part fabricated using Fused filament fabrication technique showing the internal porosity. What appears as solid also possess porosity at a smaller length scale. Courtesy of Prof. S. Yang [3].

1.2 Cellular and structured materials

Nature uses porous materials to build objects, such as wood in trees and bone in skeletons. This has inspired the engineers to produce their own synthetic structured materials. The term *cellular materials* describes solids made up of an interconnected web of solid struts, or surfaces which are the edges and faces of the cells [4]. It normally refers to *structured materials* found in nature. For their synthetic counterpart, several terms are found in the literature, such as *micro-architectured materials* or *lattice materials* for materials with periodic porosity and *synthetic foams*. Some examples are shown in figure 1.4. A section of balsa tree showing cellular structure is shown in figure 1.4(a), a synthetic foam made of cordierite in 1.4(b), and a lattice made of polylatic acid by means of additive manufacturing in figure 1.4(c).

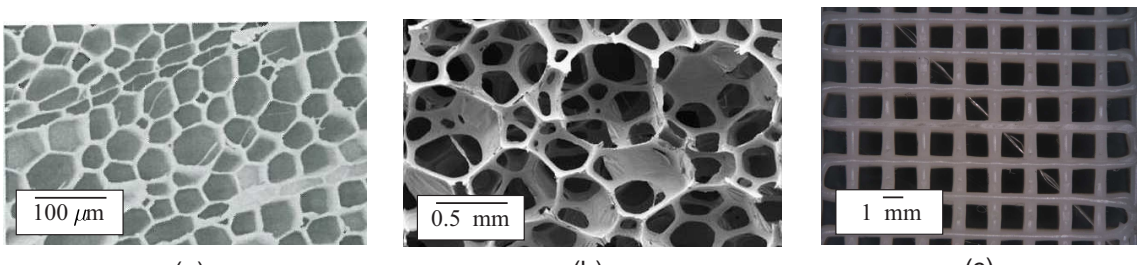

FIGURE 1.4: Examples of natural and synthetic porous materials: (a) Ochroma pyramidale (known as balsa tree) [4], (b) cordierite foam [5], and (c) polylactic acid lattice fabricated by means of additive manfacturing (present work).

According to their material structure, cellular materials can be divided in two main groups: *open-cell* structures and *closed-cell* structures. Open-cell structures are those where the the void space is interconnected with a network of slender struts, while the closed-cell are those where the network consists of interconnected surfaces that separate voids by cell walls or membranes. Examples of open-cell materials are shown in figure 1.5(a) and 1.5(c), where a polyurethane foam and a aluminium hexagonal honey comb are presented. An example of closed-cell is shown in figure 1.5(b), with a polyethylene foam.

Cellular materials offer many functional advantages over dense solids. A good comparison of how the properties of a conventional solid can be changed and sometimes improved by foaming is found in Gibson and Ashby's work [4]. Cellular media is known to have a high stiffness to weight ratio [15]. This is particularly true with stretch dominated structures. An ideal orientation of the struts in the cellular media can make them stiff and the presence of voids lighter. A well-known property is the low *strengths-large compressive strains* relationship. Cellular materials are capable of having large strains due to compression at an approximately constant stress. This characteristic make them ideal for *packaging* applications as they need material capable of absorbing energy without resulting in high stresses. Packaging material must have the following attributes: moulding (i.e. be able to adapt to the shape around objects to be packaged), energy and impact absorbing, and change in the transport speed. Foams posses all these attributes [4]. Another property to note is the *thermal insulation*. The low thermal conductivity of plastics and glass in conjuction with the low conductivity of air within the voids of the foams has been exploited in the construction of buildings, and transport systems. The lower thermal mass of these materials have made them suitable for both ultra-low-temperature and higher temperatures applications. Their use leads to greater thermal efficiency.

Natural or synthetic cellular materials, are frequently used in *structural* applications. Two important examples of cellular materials found in nature are wood and bone. Wood is commonly used for applications in construction [4]. Several studies have been carried out to relate the structure of such solids with their apparent properties [16]. Hofstetter

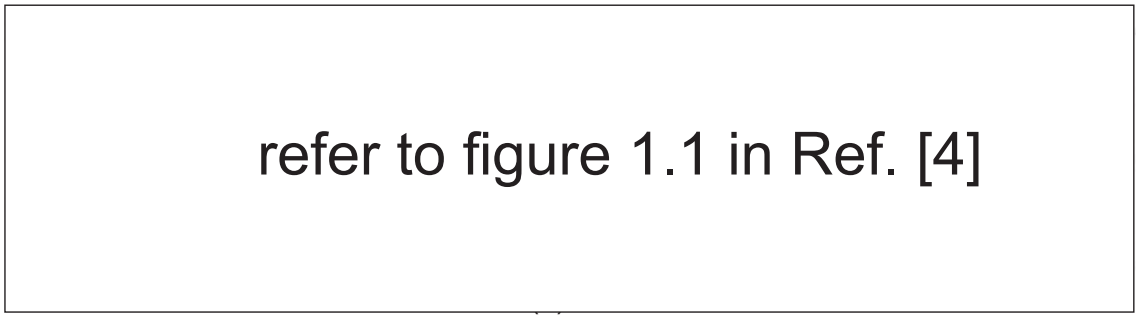

FIGURE 1.5: Examples of cellular solids: (a) polyurethane open-cell foam, (b) polyethylene closed-cell foam, and (c) aluminium honeycombs. Figure from [4].

et al. [16] developed a model based on four-levels of homogenisation to predict the elastic properties of various types of wood, such as balsa, pine, maple, oak, etc. The understanding of the properties of cancellous bone is important from the clinical point of view [17]. Lubarda et al. [17] studied the elastic modulus of bovine cancellous bone and compared this with a prediction based on the cellular solids approach [9, 18]. Other works on the mechanical properties of wood and bone can be found in [9, 18–20]. Another potential application for cellular materials that has gained interest in the recent years is in the field of biomedical engineering [21, 22]. In this field, particularly in tissue engineering (TE), structural matrices that give support to the ingrowing tissue are needed. Therefore, these scaffolds are required to have a certain degree of porosity and voids interconnectivity that proliferates the cell growth. Research on the mechanical properties of biomedical scaffolds are reviewed in the next chapter.

In the field of boat design, cellular materials are used as the core of a sandwich structures so the *rigidity* is provided by the material, in addition to *bouyancy*. Boats and floating structures make use of foamed polystyrene, polyethylene, polyvinyl chloride or silicones [4]. In aerospace engineering, sandwich structures are used in fuselage and wings where cellular materials such as honeycombs provide high shear stiffness with low weight penalty, and help in sound and noise propagation [23, 24]. Honeycombs as filters, foam sheets in chemistry, foams as water-repellent membranes, cellular solids as sound absorbers, electrical applications, among others, are just some other examples of applications of cellular materials.

Given the advantages of cellular media, the two main challenges that compete to cellular

solids are the study of their effective properties and their fabrication. Additive manufacturing techniques have shown to be a promising option to create synthetic porous materials with an specific distribution of matter. In the next section, an introduction to these fabrications techniques is given.

1.3 Additive manufacturing for the fabrication of structured materials

The structurally efficient designs found in nature (e.g. wood-trees, and bones-skeletons) use the least required resources of material for the loading condition that they face. As mentioned, this has inspired the engineering and research communities to create synthetic cellular materials, such as solid foams and lattices. Producing foams frequently results in materials with irregular cellular sizes and random topologies where control on the foam properties is difficult due to the inherent randomness of the process. To overcome this, *additive manufacturing* (AM) has been used to produce structured media with a controlled distribution of matter.

Additive manufacturing is also known as solid free form fabrication (SFF), layer manufacturing (LM). A most popular AM process is 3D printing (3DP). It consist of fabricating a 3D object by means of adding material, as opposed to conventional (subtracting) manufacturing techniques using lathe, drilling and milling machines for example where material is removed from a bulk until the final part is obtained. The AM fabrication process involves a controlled deposition of matter layer-by-layer. Controlling where the material is going to be placed, deposited or extruded, allows to put material at free will (considering the limitations of each manufacturing process discussed later in Chapter 3). This has afforded the possibility to handle and shape matter at will, producing complex structured materials.

There are different types of AM techniques, where their principal difference lies in the physical and chemical processes to fabricate the solid part. These differences produce unique physical features on the fabricated part. Each technique offers different advantages over its rivals, and the selection of the AM technology to use is given by the

intended application of the fabricated part. Selective laser sintering (SLS) and stereolithography (SLA) are AM techniques that are based on the reaction of laser beams on polymer and metal powders, and liquid photopolymers respectively [25, 26]. Electron beam melting (EBM) uses electron beam as a heat source to weld metal powder [27]. Porous structures, such as octet-truss lattice have been fabricated with EBM [6, 7]. Some of these lattices are shown in figure 1.6. Robocasting (RC) and fused filament fabrication (FFF), are techniques based on the extrusion of material through a nozzle. The material is deposited on a platform in the form of cylindrical filaments, the stack of these filaments results in the so-called woodpile architecture and it forms the 3D part. Woodpile lattices have been fabricated with RC for TE scaffolds [28–30] and as acoustic *metamaterials* [31, 32]. Fused filament fabrication has also been used to fabricate woodpile lattices [33, 34] and other lattice truss topologies [35].

In FFF-parts, the woodpile arrangement appears naturally and it offers manufacturing advantages, such as reduction in time and material employed. The mechanical properties are influenced by the structural parameters, and the study of this aspect of engineering is very much an open issue. The great potential of these material arrangements have motivated the present work in the area of structure-property relationship in FFF woodpile structures.

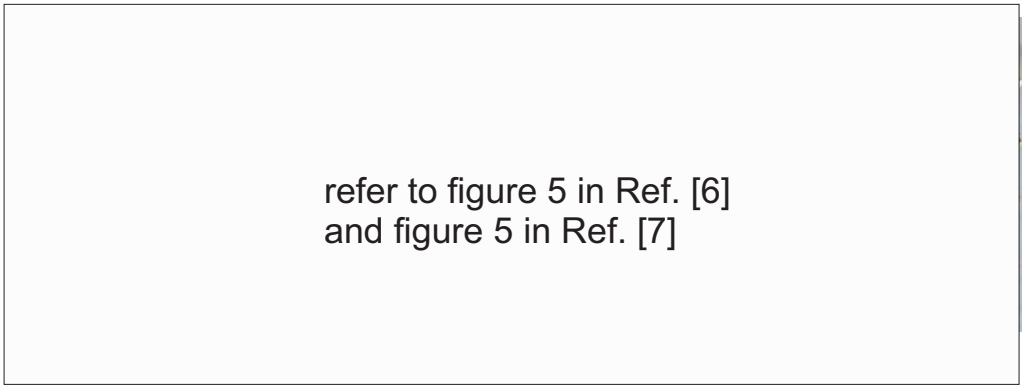

FIGURE 1.6: Examples of lattice structures fabricated with (a) EBM [6] and (b) SLM [7].

1.4 Aims and objectives

This dissertation is concerned with the elastic properties of the lattice material having woodpile architecture. Woodpile structures fabricated using FFF are considered. The results obtained here can potentially be applied to other manufacturing processes that produce the same lattice arrangement. The majority of the literature has been focused on the response of the woodpile arrangement under uniaxial tension or compression, while the study of the response under shear, bending and torsional loadings is scarce. Also, the study of the mechanical properties of components fabricated with FFF is limited to tensile and compressive experimental characterisation. With the aim of filling these gaps in the knowledge, the objective of the present work is to characterise the *elastic mechanical properties* of the *woodpile lattice material*. The main objectives of this dissertation are:

- Experimental characterisation of FFF manufactured single filaments by tensile microtesting and quantification of the Young's modulus variability within filaments;
- Theoretical, experimental and computational characterisation of the elastic response of the woodpile lattice arrangement when the load is parallel to one of the filaments axis;
- To study the flexural properties of the woodpile beams by means of analytical models, computational models and experimental three-point bending tests on FFF-samples;
- To study the torsional properties of the woodpile slender bars by means of analytical models, computational models and experimental tests on FFF-samples; and
- To characterise the elastic response of the woodpile in the stacking direction by computational models validated with analytically developed predictions.

In the next section the outline of the thesis is presented.

1.5 Thesis outline

This document is organised into eight chapters. A general introduction to all the areas involved in the research project is given in Chapter 1. In Chapter 2, a review of the literature in different areas including the mechanical properties of lattice materials and additively manufactured parts, is presented.

A comparative assessment between various additive manufacturing techniques is presented in Chapter 3. The description of the manufacturing process to fabricate the lattice testing samples is also presented in Chapter 3. The generation of the paths to be followed by the 3D printer is described too in this chapter.

In Chapter 4, we present the characterisation of parent material properties by the tensile testing of single filaments. The use of the parent material properties to predict the apparent Young's modulus of woodpile lattice samples is addressed in this chapter. A rule of mixtures approach to predict the apparent elastic property is also presented in Chapter 4.

The influence of shear deformation in the flexure of woodpile beams is studied in Chapter 5. Analytical models based on the flexure of the filaments when the lattice experiences shear loadings are derived in this chapter. Computational and laboratory experiments of FFF-samples in three-point bending are used to validated the models developed.

The theory to understand the effective torsional properties of the lattice material is presented in Chapter 6. A comparison of twist of free bundle of filaments with woodpile samples is presented also in this chapter. Computational and laboratory experiments of FFF-samples under torsion loadings are used to validated the models developed.

The elastic behaviour under compressive loadings in the stacking direction is addressed in Chapter 7. Staggered and aligned arrangements of filaments were studied. For the staggered configuration models based on slender structural elements in flexure were employed to predict the apparent Young's modulus. The aligned configuration was analysed using the elastic response of a disc diametrically loaded.

Finally, the conclusions and future work derived from the outcomes of the present work are summarised in Chapter 8.

Chapter 2

Review of literature on the mechanics and manufacturing of cellular and lattice materials

The literature review of highest relevance for this research project is presented in this chapter. First, a review of the techniques and processes to manufacture porous and structured media is given. Then, we review some of the most relevant research on the study of the mechanical properties of lattice materials. This review is divided into different specific sections: (i) introduction to the mechanical analysis of lattice materials, (ii) mechanical properties of additively manufactured lattices, and (iii) mechanical behaviour of the woodpile architecture. Finally, we review the works on the mechanical properties of parts fabricated using fused filament fabrication. The areas of opportunity on which this project is founded are given in the conclusions section of this chapter.

2.1 Manufacturing of porous and lattice materials

In Chapter 1, we have given the advantages that porous and structured media posses over their solid counterpart. These can be best exploited if the fabrication of materials with a prescribed inner structure becomes attainable. Many applications demand such

porous materials; these includes biomedical applications, elastic meta-material, sound absorption materials and lightweight lattice materials. It is a challenge to manufacture materials with a prescribed inner structure. Foam is a well-known example of an irregularly structured material.

Materials such as, metals, polymers, ceramics, glasses and composites can be foamed. In the case of polymers, the foam is obtained by means of introducing bubbles in the liquid state of the material. This can be done by introducing inert gases in the hot polymer at high pressure. By reducing the pressure, the material expands with bubbles nucleating and growing within it. Another approach to produce polymer foams is to use low melting point liquids mixed with the polymer and then heat to form vapour bubbles [4]. Metallic foams can be formed by different techniques. One method is to use powder metal that contains hydrogen which, when heated to melting point releases hydrogen as gas to form the foam. Another approach is to agitate liquid metals and infiltrate with granules of another metal which can lead to the formation of foams. Foams are also obtained by sintering, in which the powder metal is mixed with a spacing agent that decomposes or evaporates during the process. Yet other methods include the bonding of spheres or granules together, sintering hollow spheres, bonding of fibres, graphitizing in a controlled environment, among others.

Metallic lattices are frequently found as cores in sandwich structures. Wadley [10] reviewed the techniques used to fabricate metallic lattices including honeycombs and truss structures. One of them consists of the corrugation of metal sheets using a gear press. The corrugated sheets are stacked and welded together forming a honeycomb structure. In the final part of the process, the stack of sheets is sliced to a desired thickness. Another method to fabricate honeycombs, *strip slotting*, consists of producing strips of metal sheets with periodic slots. The assembly is carried out by fitting the slots of various metal sheets and bonding them by means of brazing. Strip slotting, as opposed to corrugated sheets, is ideal for honeycombs made of brittle materials as it does not involve any bending of the sheets.

The fabrication of truss topology lattices can be done by investment casting [10]. The

casts for the lattices can be fabricated using injection moulding or additive manufacturing. The negative of the cast is filled with liquid metal. No further assembly is required. However, it requires the use of equipment capable to deal with the high temperatures of molten metal. Truss topology lattices can also be fabricated by the bending of perforated metal sheets. Several options can be employed in the perforation stage, e.g. dies stamp, laser, or water cutting. Pyramidal and tetrahedral lattices are obtained by folding sheets perforated with diamond and hexagonal patterns respectively. The perforation stage produces a considerable waste of material, due to all the small sections cut.

Another method for making sandwich structures with metal lattice cores has been proposed by Queheillalt et al. [36]. The lattice is formed from the stack of layers of metallic filaments. The filaments in each layer are kept separated using an external tool (see figure 2.1). The tool consists on vertical cylinders to set the filaments with a pre-defined separation between them. The orientation of the filaments is alternated in each layer, producing lattices with the so-called woodpile architecture. The filaments are bonded by brazing and the solid face sheets are then attached to the lattice using a second brazing treatment, thus forming the sandwich structure.

It was mentioned previously that an alternative method to fabricate components made of structured materials is that of additive manufacturing. Additive manufacturing is capable of controlling the porosity of the part made, by controlling the deposition of matter very precisely. This feature makes them an ideal option for the fabrication of micro-architectured materials. In the field of tissue engineering (TE), extrusion-based techniques (FFF and RC) have been used in the past to produce porous structures made of ceramics and polymers. Some examples can be found in [28–30, 37–40], each work will be reviewed in turn in the following sections. Fused filament fabrication and RC techniques consist of extruding filaments and deposit them on a platform. As a result, the stack of these filaments produces 3D scaffolds in the woodpile arrangement. Further details on the manufacture of these are given in relevant section within Chapter 3. The main advantages of using AM to build porous scaffolds for TE include: (i) macro-shape

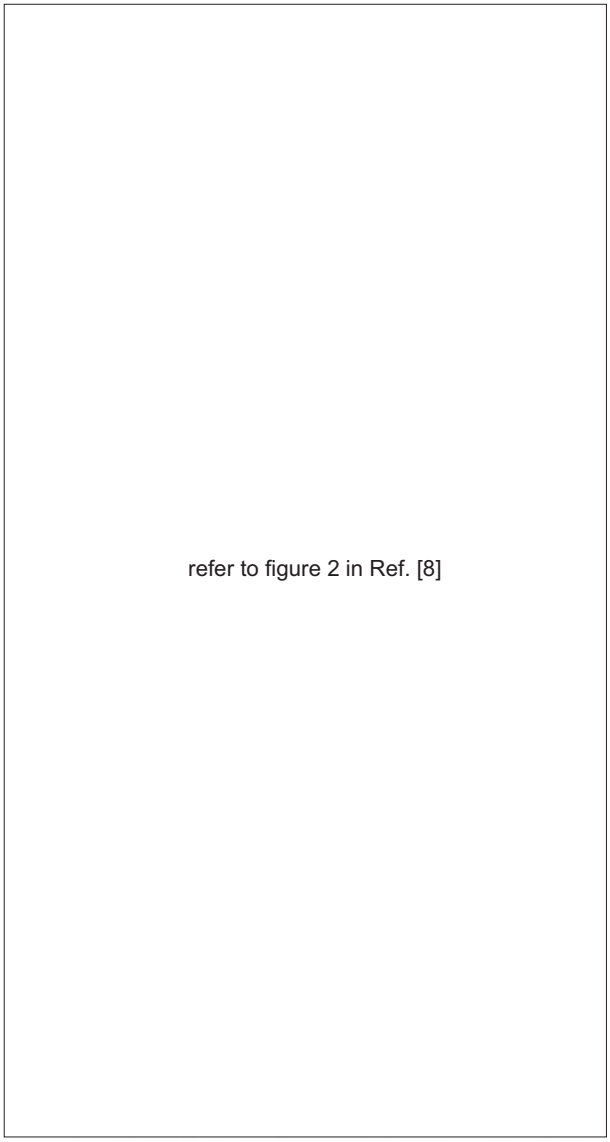

FIGURE 2.1: Schematic of the procedure developed by Moongkhamklang et al. to fabricate woodpile lattices. Figure from [8].

control (scaffolds with complex macro geometries), (ii) micro-structural control, (iii) high surface to volume ratio, (iv) independent control of porosity and pore size.

Powder based AM-technologies, such as SLS and EBM, have been used to produce truss lattice materials. An example of this is found in Suard et al. [41], where octet truss lattices were fabricated with EBM. Truss lattice materials have also been fabricated using FFF by Ravari et al. [42]. Truss lattices fabricated with AM techniques are composed of trusses with struts built layer-by-layer. This produces struts with non-uniformities across the length and cross-sections. The mechanical properties of the lattices studied in [41, 42] are reviewed in Section 2.3.1, where the variability in the structural parameters

mentioned is taken into account. Various general concepts in the study of the mechanical properties of lattices are introduced next.

2.2 General concepts of the mechanical properties of structured materials

The mechanical properties of cellular and lattice materials show dependence on the following: (i) the mechanical properties of the parent material, (ii) its topology and cell geometry, and (iii) the relative density. The relative density, $\bar{\rho}$, is the ratio between the density of the cellular material and that of the material that is composed of [4]. The relative density is equal to the volume fraction, $\bar{\rho} = V_s/V_c$; where V_s is the volume of the solid material and V_c is the volume of the lattice material considering the external dimensions, i.e. porosity-filled space of the lattice material. When the characteristic lattice dimensions are significantly smaller than the overall dimensions of a piece of solid, one can represent the properties of such structural solids by means of *apparent properties*– as if the material were homogeneous having equivalent continuum properties. An apparent property, $\langle P \rangle$, of a structured material can often be expressed as,

$$\langle P \rangle = CP\bar{\rho}^n \tag{2.1}$$

where P is the property of the parent material (e.g. Young's modulus), and C and n are constants related to the deformation mechanism of the lattice elements and topology. The exponent n, which depends on the micro-architecture response, defines the scaling relation of the apparent property with the relative density. In general, due to deformation response, lattice materials are classified into two main groups: bending-dominated and stretch-dominated structures. In the following two sections more details on these two types of deformation mechanisms are given.

2.2.1 Bending-dominated structured materials

When a structured material responds to a remote stress σ_∞ by the deformation of their constituent cell wall structural elements in bending, the material is said to be *bending-dominated*. In lattices with such mechanism of response, the constituent elements are found with a certain inclination with respect to the loading direction and joint with a topology that is kinematically rigid [43]. Take the frame shown in figure 2.2(a), assuming the struts are connected with joints that allow rotation, the struts respond under the action of force F by rotating with respect to each other, behaving as a *mechanism*. If joints are now restricted avoiding the rotation, the struts bend under the action of the force F. Similarly, the hexagonal honeycomb is an example of bending-dominated lattices (see figure 2.3(a)), where the response to an in-plane remote stress σ_∞ is given by the bending of the inclined members. It is worth mentioning that although the word *strut* has been used in the past for structural elements that is under axial loads, in the field of structured materials it has been used as a general lattice element, that is not necessarily under axial loading only.

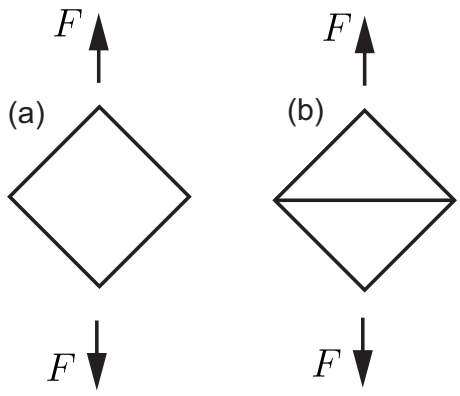

FIGURE 2.2: Schematic of a (a) bending-dominated and (b) stretch-dominated structures.

The stress-strain curve of this type of materials starts with a linear elastic part given by elastic deflection of the lattice elements. Then, the lattice elements can suffer plastic deformations or failures. This part is characterised by plastic yield, buckle or fracture of the lattice elements. This happens at nearly constant stress making this type of material ideal for energy absorption applications. In the stress-strain curve it is observe as a horizontal line, known as *plateau*. The collapse continues until the elements in

the structure become in contact with each other. This stage, known as *densification*, is characterised by stiffening of the material. In a stress-strain curve it is observed as an increment in the stress after the plateau.

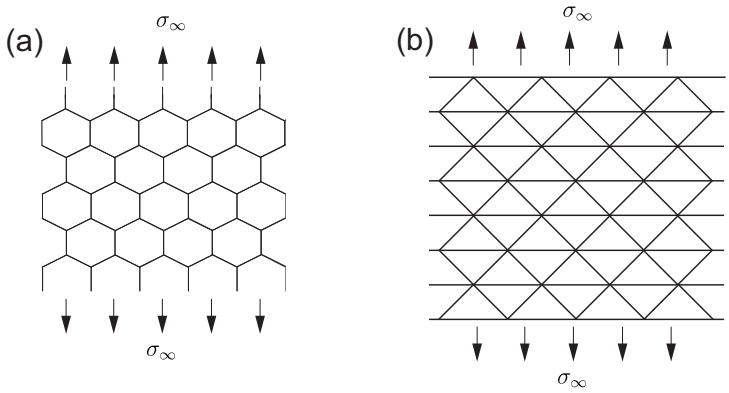

FIGURE 2.3: Schematic of an hexagonal and triangulated lattices, which are known to be bending- and stretch-dominated structures.

2.2.2 Stretch-dominated structured materials

Lattices that respond to a remote stress σ_∞ by the stretch or compression of the constituent elements are known as *stretch-dominated*. Consider the triangulated frame in figure 2.2(b), having welded-joints, under the action of force F the dominance of the response is given by the axial elongation and compression of the struts. Similarly, take the lattice shown in 2.3(b) which is formed with a periodic distribution of frames from figure in 2.2(b). Under the action of a remote stress σ_∞ in direction indicated, the response is dominated by the extension and compression of the struts. These lattices appear to be stiffer and stronger, compared to the bending-dominated lattices for the same volume fraction and parent material. This makes stretch-dominated structures suitable for load bearing applications but less ideal for energy absorption than the bending-dominated configurations where plastic deformation of cell walls is key.

The stress-strain curve for a compressive loading of a stretch-dominated structure is characterised by an initial linear response given by the elastic compression or stretching of the lattice elements. This initial linear response gives the apparent Young's modulus $\langle E \rangle$. The limit of the elastic response can be given by three mechanisms: yield, buckling, or fracture. Normally, lattices with low relative densities will present failure because

in buckling if the struts are in compression. Lattices with low relative densities have slender elements making them more prone to failure by buckling. Lattices made of brittle materials will collapse by the fracture of their elements when in tension.

2.2.3 Deformation-mechanism maps

The stages in deformation of structured materials are summarised visually in a *deformation-mechanism map*. The deformation-mechanism maps for structured media are one of the main contributions found in Ashby's work [9]. An example for elastomeric foams under remote compressive stress is shown in figure 2.4. The stages described earlier are clearly indicated: linear elasticity, elastic buckling, and densification. The regions in which each deformation-mechanism dominates are shown and separated with heavy solid lines.

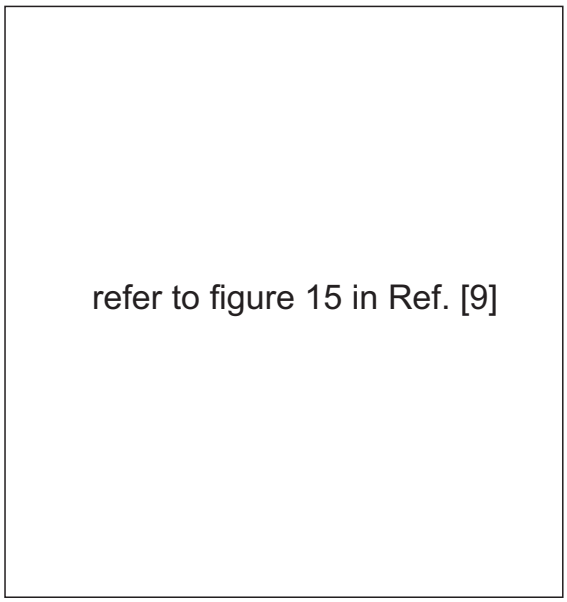

FIGURE 2.4: A deformation map for elastomeric foams. Figure from [9].

A qualitatively representation of a deformation map for woodpile materials under compressive loading is shown in figure 2.5(a), for three assumed relative densities. Due to the filament distribution, the elastic response of this lattice material is dominated by the bending of the filaments, i.e. bending dominated. Note that for this particular arrangement of matter, filaments in flexure will get in contact with filaments in adjacent layers, before reaching plastic deformation (see figure 2.5(b)). This particular behaviour will be reflected in a response with no plateau. The contact between bent filaments will

result in an increase of stiffness, i.e. densification. Further details of the linear elasticity of this material arrangement are given in Chapter 7. Having defined the relative density $\bar{\rho}$, and its influence on the apparent properties we now proceed to review the works done on the analysis of the apparent mechanical properties of lattice materials.

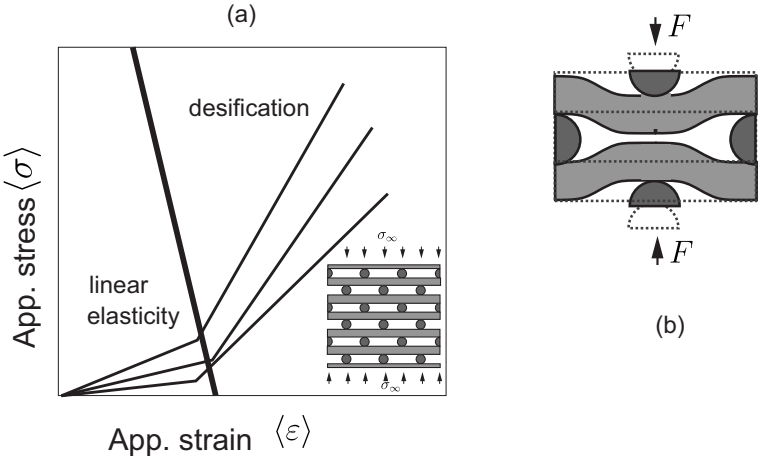

FIGURE 2.5: (a) A qualitatively representation of a deformation map for woodpile lattice material with staggered arrangement of filaments, under compressive loading. (b) Unit cell of the woodpile staggered arrangement, showing the flexure prompt to contact under the loading.

2.3 Mechanical properties of lattice materials

Prior to the use of lattice materials in any application, the understanding of the mechanical properties is required. The understanding of the mechanical properties becomes relevant, as difference in the arrangements of matter result in differences in the properties for lattices made of the same parent material and volume fraction. The study of the structure-property relation of these materials is of great current interest for the engineering community.

The work of Gibson and Ashby [44, 45] was one of the earliest relating structure to apparent properties by making use of the lattice geometry combined with the structural mechanics of elastic members constituting the lattice. From structural analysis on representative unit cells, of which the walls were modelled as beams, analytical models for the apparent Young's modulus of honeycombs were derived in [44] and for foams in [45]. The resulting apparent properties are a function of the intrinsic properties of the parent

material, its relative density $\bar{\rho}$ and structural parameters, the geometry of the lattice elements and the connectivity of the cell walls. For the hexagonal honeycomb, the apparent Young's modulus scales with relative density as $\langle E \rangle \sim \bar{\rho}^3$. This scaling relation has the basis that the relative density of the hexagonal honeycomb scales with the thickness t and the length l of a cell wall of the honeycomb as $\bar{\rho} \sim t/l$; whereas the bending behaviour, has a dependence with the length of l^3. Similarly, foams were modelled as a cubic array of structural elements, beams and plates for open- and closed-cell foams respectively. The resulting apparent properties scale with the relative density as $\bar{\rho}^2$ and $\bar{\rho}^3$, for open- and closed-cell foams, respectively. Gibson-Ashby work differs from the research presented in this document, by the dimensionality. While Gibson-Ashby focused primarily on 2D lattices, the woodpile arrangement is a case of a periodic 3D lattice, and therefore models proposed by them cannot be used. Throughout the document, the precise analytical models to predict the apparent elastic properties are developed and presented.

Lattice materials are frequently used as cores in sandwich structures. Deshpande and Fleck [46] studied tetrahedral lattice materials used in this context. A unit cell of the tetrahedral lattice is shown in figure 2.6(a). Analytical expressions for the apparent properties (e.g. Young's modulus, shear modulus and strength) were developed. All these apparent properties resulted with scaling relation with respect to the aspect ratio of the radius r and length l of the constituent struts as $(r/l)^2$. The expressions were derived under the assumption of the tetrahedral lattice struts being idealised as pin-jointed assemblies. In their study, they identified four collapse mechanisms: face-yield, face-wrinkling, indentation and core shear. Collapse mechanism maps were constructed to aid in the structural design of sandwich structures. The shear failure of the lattice core appeared to be by the plastic shearing of the pins where the core is attached to the solid sheets. The analytical expressions were compared with the experimental response in three-point bending of lattices fabricated from aluminium LM25 and silicon brass MB1.

Deshpande et al. [47] studied the apparent properties of octet-truss lattices. A unit cell of the octet-truss lattice is shown in figure 2.6(b). This lattice is stretch-dominated and

the apparent Young's modulus resulted with a linear scaling relation with the relative density as $\langle E \rangle = CE\bar{\rho}$; where the constant C is related to geometric and structural parameters. For the analytical model, the struts are assumed to be pin-joined, neglecting the contribution of the bending of the struts to the apparent property. In their study, they compared the analytical and FE predictions with experimentally obtained measurements on LM25 aluminium lattices under uniaxial compression.

Wallach and Gibson [48] conducted a numerical study on the apparent properties of an aluminium cast truss lattice with a unit cell, like the one shown in figure 2.6(c). In their work, the apparent Young's modulus and shear modulus were studied. They experimentally tested lattice materials in tension, compression and shear to obtain the said apparent properties. They used measured data to develop a numerical model for these apparent properties. The apparent properties have a linear scaling in relation to the relative density i.e. $\langle E \rangle = C_e E\bar{\rho}$ and $\langle G \rangle = C_g E\bar{\rho}$; where constants C_e and C_g were determined from experimentally obtained data. The struts of the truss unit cell were modelled as simple truss members having pinned joints. This assumption neglects the contribution of the bending moments. In comparison with the experimental results, the numerical models were in close agreement, having the greatest discrepancy for the shear modulus $\approx 27\%$.

The lattices studied by Deshpande et al. [46, 47] and Wallach and Gibson [48] were fabricated using an investment-casting procedure. The use of a cast prevents the production of struts with irregularities in their cross-section (as discussed earlier in Section 2.1); the material poured in the mould takes its shape, avoiding non-uniformity. A new mould is required for every structural modification of the lattice architecture. By contrast, AM techniques are capable of producing lattices with different structural parameters and geometries with no changes in the fabrication machine. This can directly impact in a reduction of the production cost and time, making AM techniques suitable for the fabrication of lattices. The next section presents a review of the works dealing with the mechanical properties of lattices fabricated with AM technologies.

2.3.1 Mechanical properties of additively manufactured lattice materials

Most studies on the mechanical properties of AM-lattices have been focused on those fabricated with powder and laser based technologies such as electron beam melting (EBM) and selective laser melting (SLM). Murr et al. [49], used EBM to fabricated open cell titanium foams and characterised their apparent Young's moduli using resonant frequency-damping analysis. The values for stiffness measured were in good agreement with the values predicted using Gibson and Ashby models [4]. Parthasarathy et al. [50] worked on the mechanical properties of EBM-lattices made of titanium. In [50], cubic samples with square voids were characterised via compression tests resulting in a decrease of the stiffness and strength when the degree of porosity is increased. Scanning Electron Microscopy (SEM) and an optical microscope were used to characterise the resulting porous materials showing struts to be uniformly formed but with rough surfaces [50]. EBM-lattices possess a high degree of imperfections on the struts elements, having struts with irregular cross-sections. This is because the struts are formed by the bonding of the powder particles, hence surfaces with poor smoothness are formed.

The use of FEA has been used to predict the mechanical properties of AM-lattices fabricated with powder-based techniques accounting for the imperfections mentioned [41, 51]. Campoli et al. [51] modelled the non-uniform cross-sectional area of the SLM-struts using beam finite elements having length sections of the beam elements with different cross-section diameters. Moreover, Suard et al. [41] proposed a methodology to predict the stiffness of EBM octet lattices (figure 2.6(b)) with trusses with rough surfaces. The methodology consisted of a multi-scale modelling to characterise the stiffness. First, a computational model made from X-ray tomographies of the struts was created. From this model, the stiffness is calculated and then the dimensions of strut, that will give equivalent elastic responses is obtained. The equivalent strut dimensions can be used to create FEA models of the whole truss structure to predict the apparent stiffness.

McKown et al. [52] studied stainless steel 316L SLM-fabricated lattices under compressive and blast loadings. They studied two truss structures with unit cells, as depicted in figures 2.6(d) and 2.6(e), by loading them in the z-direction. In [52], the two truss

structures resulted in different failure mechanisms under compression. For lattices having struts aligned to the compressive loading direction (figure 2.6(d)), the failure mechanism was observed to be buckling. This is expected as slender structural elements aligned to the compressive loading, lead to buckling. For the lattice with no struts aligned to the loading direction (figure 2.6(e)) the failure was identified to be by progressive collapse. The blast loading tests showed that the lattice with the struts aligned to the loading direction, failed due to a shear band propagation at an angle of $\sim 45°$ caused by the buckling. The lattices without the vertical struts presented the same crush behaviour in the blast loading tests as in the compression tests.

Lattices simillar to those studied by McKwon et al. [52] were fabricated of polylactic acid (PLA) using FFF by Karamooz Ravari et al. [42]. A schematic diagram of a unit cell of this lattice is shown in figure 2.6(f). Karamooz Ravari et al. employed FEA to predict the mechanical behaviour of the truss lattices using two different models. One of the models used 2D beam elements to model the struts, while in the other used solid elements. The struts in the truss were built layer-by-layer, producing lattices with clear discontinuities in the surface of the trusses. To represent the variability of the cross-section, the FEA models have beams with non-constant cross-sections. Both models showed good agreement with the experimental data for stiffness. Moreover, FFF produce parts with an inherent lattice that consists of the alternating stacks of filaments. In the next section, we review the works on this specific material arrangement.

2.4 Mechanical properties of woodpile lattice materials

The present work is focused on lattice materials that consist of orthogonal stacks of struts in a woodpile arrangement. Therefore, works done on understanding its mechanical properties are reviewed. The woodpile arrangement can be obtained from several fabrication processes. One of the processes to produce woodpile lattice was proposed by Queheillalt and Wadley [36] and it was reviewed in Section 2.1. In extrusion-based AM techniques such as fused filament fabrication [40, 53] and robocasting [28, 29] this arrangement appears naturally.

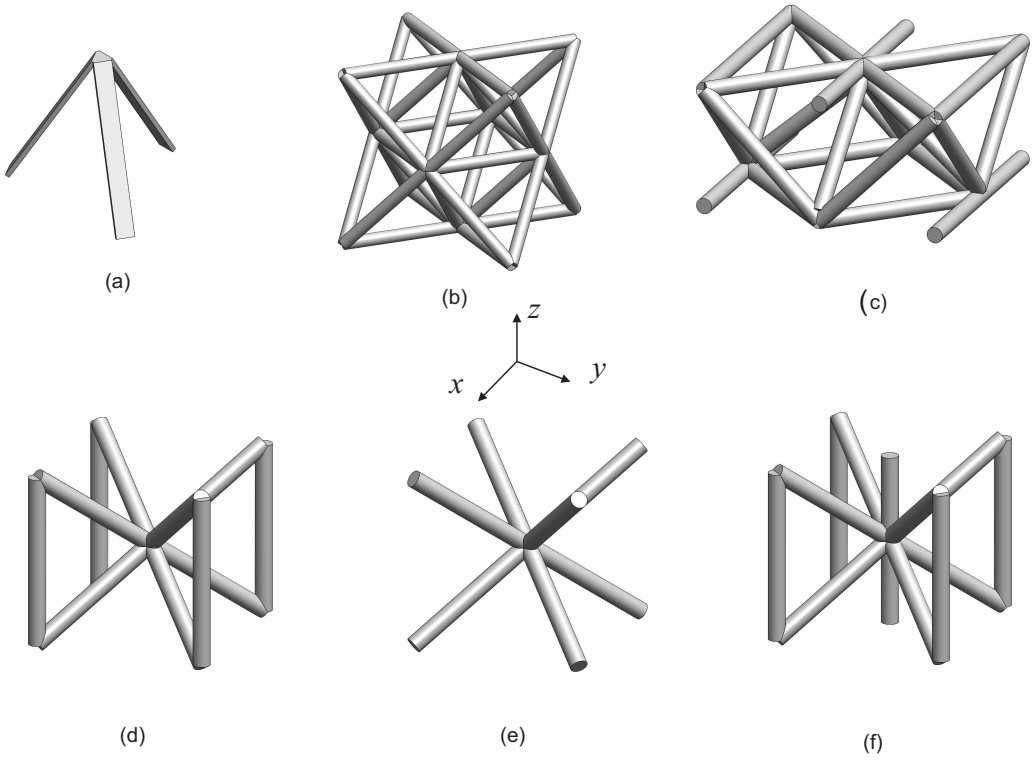

FIGURE 2.6: Unit cells of various lattices.

2.4.1 Woodpile lattice as core in sandwich structures

Queheillalt and Wadley [36] built stainless steel woodpile lattices with hollow filaments and studied their compressive response. The lattices were used as cores in sandwich structures having two different orientations: (i) one in which one of the axes of the filaments was aligned to the loading direction (see figure 2.7(a)), and (ii) another one where the filaments were oriented at 45° to the loading direction, referred as 'diamond' orientation (see figure 2.7(b)). The load direction studied is indicated in figure 2.7. The apparent elastic properties of the aligned configuration were predicted using a model that considers only the filaments aligned to the loading direction contributing to the stiffness. In the diamond configuration, only the filaments that are bonded to the top and bottom plates of the sandwich contribute to the apparent stiffness. In both arrangements, the stiffness is given by the elastic compression or tension of the participant filaments. The compressive strength was predicted using an analytical model based on the inelastic buckling stress of a hollow cylinder. The experimental data lies between the predicted

trends considering filaments bonded with built-in and pin-joined nodes. Later on, Queheillalt et al. [54] compared the mechanical behaviour of the orientations presented by Queheillalt et al. [36] with that of lattices with the woodpile woven arrangement. The woodpile woven arrangement consists of struts with waviness. Wires with a sinusoidal shape passing above and below of consecutive struts, similar to the shape formed by yarn in a fabric, are presented in such structures. An analytical expression for the woven configuration was derived using strain energy methods for curved beams. The analytical and FEA predictions were in good agreement with the experimental data on stainless steel lattices. The woven configuration resulted with apparent properties 20% lower than those of the lattices with straight struts for the same volume fraction.

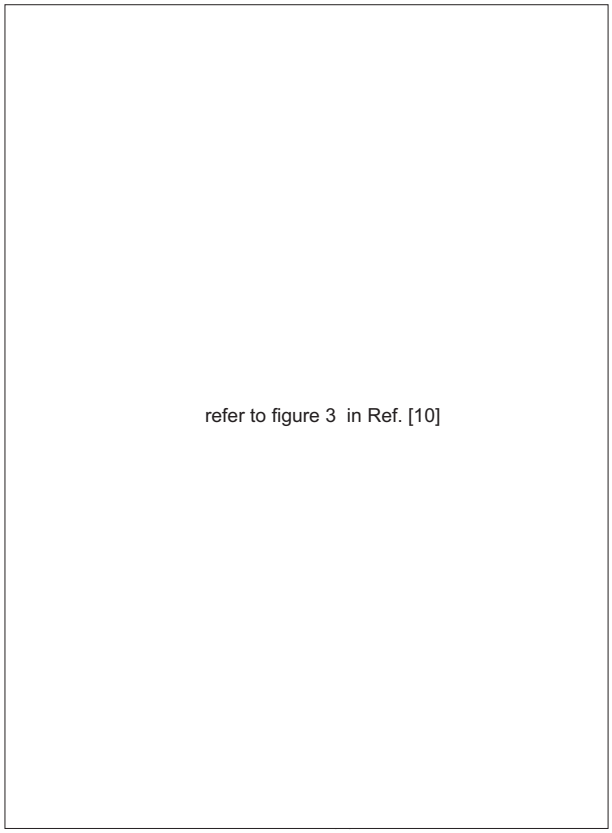

FIGURE 2.7: Schematics of the woodpile architecture used as core in sandwich structures at two different orientations (a) aligned and (b) diamond orientations. Figure from [10].

Mooongkhamklang et al. [8] studied the apparent Young's modulus and the shear modulus of the woodpile lattice composed of titanium-based composite filaments. Analytical models were developed and compared with experimental data obtained from compression

and pure shear tests of sandwich structures. The sandwich structures were also fabricated using the assembly and brazing process previously described [36, 54]. They studied the apparent Young's modulus of the aligned orientations under compressive loadings. The shear modulus studied corresponded to loading and response in the plane of the filaments (see figure 2.7). It was observed that when the lattice is under shear loadings the deformation is given by the bending of the struts between each junction. An analytical expression for apparent shear modulus which assumes the filaments are bonded with fixed-joints was provided. The model was obtained by analysing a unit cell, of which the filaments were modelled as beams. The model is suitable for lattices with low relative density where the separation between struts is such that Euler-Bernoulli assumptions are adequate to predict the flexural behaviour. The strength of the titanium-composite lattices under compression along the filaments direction was studied by Mooongkhamklang et al. [55]. The strength was observed to be dominated by the cooperative elastic buckling of the filaments lying parallel to the loading direction. In [55], the stiffness and strength of the titanium-composite lattice were compared against similar lattices like the ones studied in [36, 54], showing superior properties.

2.4.2 Woodpile arrangement as scaffolds in tissue engineering

The works reviewed in the previous section concern the woodpile lattice made of metals and used as core for sandwich structures. This material arrangement is also frequently found in scaffolds in tissue engineering (TE). Scaffolds in TE are porous structures that serve as support for cells to proliferate. Scaffolds need to be structurally efficient to withstand loading due to the ingrowing tissue. This enhances the relevance of the understanding of the mechanical properties of lattices in woodpile arrangement. In figure 2.8, an SEM image of the woodpile arrangement is shown, which is to be used as a scaffold, for the growing bovine articular chondrocytes. Note the growth of tissue in the attached to the filaments of the woodpile, and in the gaps between them.

Scaffolds are commonly fabricated using AM technologies such as RC [28–32] and FFF [53, 56, 57]. The structures fabricated using these techniques result in the stack of filaments. Due to the stacking arrangement of layers with alternating orientations, the

lattice material will result in filaments running in two orthogonal axes. The mechanical properties along the filament axes are very different from those along the stacking direction. The stacking axis is also referred to as the axis *perpendicular to the printing plane*. The works reviewed in the previous section did not concern the response of the lattice in this direction. The lattice in sandwich structures was oriented so that the influence of this response is neglected. Nevertheless, this orientation is frequently used in the scaffolds used in tissue engineering.

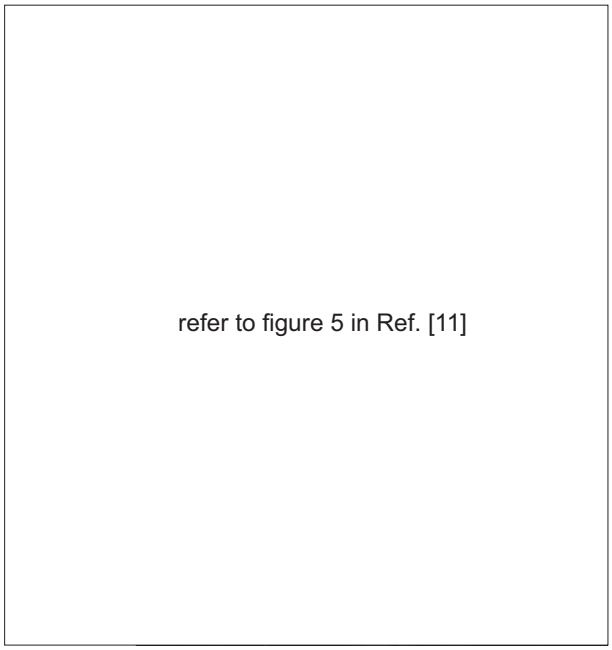

FIGURE 2.8: SEM of scaffolds showing seed and ploriferation of bovine articular chondrocytes. Figure from [11].

Woodpile structures have been recently studied under compressive loadings. Hutmacher et al. [56] reported the compressive properties in the stacking direction of scaffolds fabricated with polycaprolactone (PCL) using fused filament fabrication. Two arrangements were compared: one where the stacking sequence of layers had filaments oriented at $[0°/60°/120°]$ and other with $[0°/72°/144°/36°/108°]$. The later showed lower properties $\approx 50\%$ in stiffness. Zein et al. [57] characterised the stiffness and strength under compression tests of PCL-scaffolds with filaments oriented at various angles. The orientations tested were: $[0°/90°]$, and $[0°/60°/120°]$. The stacking lay-down patter of $[0°/90°]$ resulted 30% stiffer than the $[0°/60°/120°]$.

Miranda et al. [28, 29] studied the mechanical properties of calcium scaffolds for tissue

engineering applications using FEA and laboratory experiments. In [28], the scaffolds were subjected to compressive tests to study their strength. Two different ceramic materials were compared (β-tricalcium phosphate and hydroxyapatite). The failure of these scaffolds was attributed to the micro-cracks in the ceramic filaments. In [29], FEA models were used to predict the strength properties by analysing the stress fields. The FEA models consisted of a stack of struts modelled as cylinders with a fixed overlap fraction between them. The models were subjected to compressive, tensile and shear loading. The stress contours were studied for each loading, showing a directional dependence. The shear simulations showed high concentration of stress at the joints, indicating a failure by cracking at these locations. The scaffolds tested here were of high relative density, having the filaments at a distance slightly bigger than their diameter. This complicates the development of analytical models, so their analysis in [29] was restricted to FEA predictions.

Sobral et al. [58] studied different arrangements of poly(ε-caprolactone) filaments, including those where the porosity was functionally graded, under static and dynamic compressive loadings. A comparison was made between scaffolds with equally distributed filaments and gradient distribution. For the equally distributed fillaments, the separation between filaments tested were: 750 μm and 100 μm. The graded scaffolds had a porosity linearly varied from 100 μm to 750 μm, one set of samples had the denser part at midheight while the other had the denser part at the top and bottom. The samples had the same overall dimensions. The highest value for stiffness was observed in the samples with filaments closer to each other and equally distributed. The samples showed higher stiffness as they were made with larger number of filaments. But in terms of cell seeding, the scaffolds with graded porosity showed better results, as they posses filaments offsets with respect to the adjacent layers. The alternation of filaments prevents cells to fall to the bottom of the scaffolds as observed for the scaffolds with equal distribution of filaments.

Norato and Wagoner-Johnson [30] studied woodpile material arrangement using the unit cell approach and presented analytical models for the apparent Young's modulus along the axis perpendicular to the printing plane. The model consists of the interpolation

between the plane stress and the plane strain responses of a disc and a cylinder under diametrically opposed loads. The constants for the interpolation based model were obtained from simulations using a geometry projection numerical model. The model presented in [30] showed a dependence on the fraction of volume share between adjacent filaments. This fraction is known as *overlap*. Such dependence was also observed experimentally by Naghieh et al. [53] on scaffolds fabricated with the FFF technique. Naghieh et al. [53] fabricated the scaffolds using polylactic acid (PLA) and showed that the apparent Young's modulus is strongly dependent to this parameter; stiffness increases as the overlap increases. The studies in [30, 53] are restricted to lattices where filaments are bonded by having overlap, and aligned in the stacking direction. The case of woodpiles where the filaments are distributed in an staggered arrangement is addressed in Chapter 7. The staggered arrangement is believed to have better results for cell growth purposes [58], and the understanding of the mechanical properties is addressed for the first time under shear and compressive loadings, in Chapter 5 and Chapter 7, respectively.

Attempts to understand the flexural response of beams made of such lattice material are extremely limited with exception of a few recent works [59–62]. Yeo et al. [59] studied that changing the position of the filaments produces different pore sizes that resulted more suitable for bone tissue regeneration. They used FEA computations to study the response of woodpile cantilever beams with various arrangements of filaments, where the axial filaments were kept constant for all the cases tested. Negligible differences were observed among all the arrangement tested. The authors in [59] did not provide an explanation of this behaviour. The role of the filaments that run across the axial direction is studied for the first time in Chapter 5. Its influence in the transverse deflection of woodpile beams is tracked to the apparent shear modulus, which in turn is dominated by the filament flexure. Martinez-Velazquez et al. [60] studied the flexural properties experimentaly in four-point bending of β-tricalcium phosphate based samples. The objective in [60] was to study the influence of the impregnation of the samples with polymers such as polylactic acid and poly(ε-caprolactone). Liu et al. [61], characterised bioactive glass scaffolds by mechanical testing under compression, flexure and fatigue. The effect of incorporation of polylactic acid and poly(ε-caprolactone) in mechanical properties of bioactive glass scaffolds was studied by Eqtesadi et al. [62]. The flexural properties

studied in [60–62] were characterised by means of four-point bending. However, no attempt to predict the flexural response seems to exist in the published literature. In this research work, novel analytical models to predict the transverse deflection of woodpile beams are developed and presented in Chapter 5.

Biomedical scaffolds have been fabricated by several researchers in the past using AM techniques. Components for other applications can also be fabricated using similar techniques. A review on the works on the lines of the mechanical characterisation of parts fabricated with fused filament fabrication is presented next.

2.5 Mechanical properties of parts fabricated using fused filament fabrication

The current trend is to use AM, not only to fabricate prototypes, but also to produce ready-to-use components. In order for these components to be functional, the understanding of their behaviour under different loadings is important. The study of the mechanical properties of FFF-components has been restricted primarily to experimental characterisation in the past. It has been observed that structural parameters, e.g. filament separation, filament orientation, have a greater influence on the mechanical properties of FFF-components than manufacturing parameters, e.g. extruder temperature, filament colour, nozzle traverse speed. This highlights the importance of understanding the structure-property relation in parts fabricated using AM-tehnology.

The adjustment of structural and manufacturing parameters results in variations in the properties. Rodriguez et al. [63] characterised the stiffness and strength in terms of the microstructural parameters. Unidirectional filament samples made of acrylonitrile butadiene styrene (ABS) were studied. The optimal filament gap was found to be -25.4 μm, when the structure was optimised for compressive strength. A negative gap is associated with the distance between extruded filaments being less than the diameter, (see figure 2.9). The authors in [63] concluded that the extrusion rate and envelope temperature affect the filaments cross-section and the filament-to-filament bonding strength. A finite element heat transfer analysis to understand the solidifying temperature process is also

reported in [63]. The authors presented temperature-time curves where it can be seen that the centre cools rapidly (within 0.55 sec). Variations in the filament thickness are due to the non-uniform temperature distribution shown in the temperature profile. This corroborated with SEM images of the resulting structure.

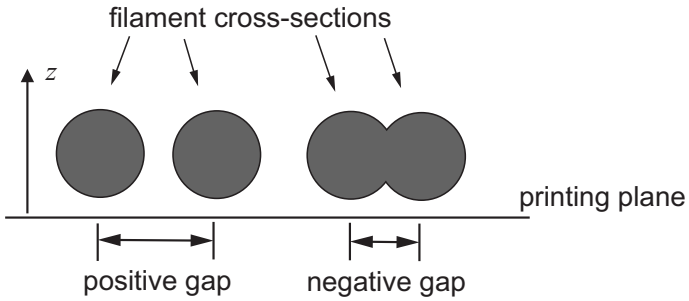

FIGURE 2.9: A schematic representation of filament cross-sectional areas, showing the difference between positive and negative gaps.

Rodriguez et al. [64] studied three different arrangements of filaments in the FFF-parts made of ABS. The arrangements tested by them included: one in which the filaments in each layer are aligned with the filaments of the adjacent layers, and negative gaps between them; and two skewed, one with negative gap and one with positive. Rodriguez et al. used experiments on raw monofilament to measure the stiffness and strength of the parent material in order to compare them with the resulting form FFF-ABS printed samples. From all the arrangements tested the aligned with negative gap resulted with the highest stiffness and strength values. The mechanical properties of the FFF parts were found to be inferior to those of the parent material. Reductions of 11% to 37% in the stiffness and 22% to 37% in the strength were observed and reported in [64]. The largest differences correspond to parts fabricated with positive gaps between filaments. The reduction is attributed to the presence of voids, as shown also in this chapter. The reduction in mechanical characteristics can be seen as a drawback, nevertheless, parts fabricated with voids are lighter and produced faster than fully dense parts.

Montero et al. [65] used the design of experiments approach, considering the deposition orientation, gap between filaments, filaments colour and extrusion temperature, to observe their influence on the strength of FFF-specimens. A reduction between 67%-72% was observed, attributed to the presence of voids, and the filaments orientation. Design

of experiments has also being used to study the mechanical properties of FFF parts by Ahn et al. [66], Sood et al. [67], Onwubolu and Rayegani [68].

Ahn et al. [66] characterised the properties of samples manufactured with ABS. They studied the influence of manufacturing parameters on the tensile and compressive properties. They considered parameters such as filament orientation, filaments width, filament separation, colour, and model temperature. In their work, the influence of filament separation and orientation on tensile strength was observed to be most significant. The mechanical properties of the FFF-ABS were compared with those of fully dense samples fabricated by injection moulding. No arrangement with positive gaps between filaments was analysed in this work. In [66], the strength of the parts loaded along the axis perpendicular to the printing plane was tested under compression, resulting in 15% lower compressive strengths than the axially loaded samples. Ahn et al. [66] considered filament orientation aligned to the loading direction (*axial*), 45° (criss-cross) and perpendicular (*transverse*). The structure is 10 times stronger axially than transversaly. This suggests the anisotropy of parts fabricated with FFF, as parts fabricated are directionally sensitive. The parts fabricated with a negative separation between filaments possess a lower porosity and therefore, results in higher strength (≈2 times for transverse orientation). Both Sood et al. [67] and Onwubolu and Rayegani [68] built empirical models to predict the strength of FFF-samples based on central composite design of experiments, and using group method for data handling respectively.

Bellini and Geri [69] presented a methodology for the mechanical characterisation of ABS products manufactured with FFF. They presented a comparison between the mechanical properties (i.e. tensile strength, maximum strain, and elastic modulus) of ABS single pre-manufactured filaments and single FFF-ABS filaments. Almost no extrusion effect on the strength and stiffness was observed. However, a reduction of one third on the maximum strain was noted. The last observation was explained by the authors using the viscoelastic behaviour of ABS. As material passes through the extruder its molecular chains are submitted to such orientations that reduce its elongation properties. They tested samples of different orientations with no gaps between filaments and [0°/90°/+45°/-45°] layers. Experimentally determined elastic moduli were used to

form the stiffness matrix. The authors [69] used domain decomposition on the raster to evaluate the effect of the nozzle-path. The samples lying on the printing plane are more sensitive to nozzle-path modifications. Samples that are built perpendicular to the printing plane have their response predominantly dependent to the bonding between layers.

RepRap are a class of printers that work on the principle of extruding semi-molten filaments. The RepRap is an open source model that can be built for less than $1000 [70]. Further details on the RepRaps are given in Chapter 3. Tymrak et al. [71] characterised the mechanical properties from the tensile testing of samples fabricated using RepRap printers. The objective of [71] was to compare the mechanical properties (strength and stiffness) of parts fabricated using RepRap machines with that of parts fabricated with commercial FFF printers. Parts showed comparable properties, which gives low cost printers a clear advantage when compared to commercial FFF printers. Again, in [71] only "fully" dense parts were studied.

Classic laminate theory (CLT) has been combined with experimental tests to study the mechanical properties of FFF-components. Kulkarni and Tutta [72], Li et al. [73], and recently in Casavola et al. [74] and Ziemian et al. [75], used similar approaches obtaining the elastic constants of the stiffness matrix through laboratory experiments. Kulkarni and Dutta [72] were perhaps the earliest to use CLT to predict the mechanical properties of parts fabricated with FFF. The stiffness matrix was fed using experimentally measured elastic properties. The properties were obtained from tensile test on unidirectional samples. Different orientations were used, longitudinal, transverse and 45°. Li et al. [73] followed a similar procedure. Li et al. also presented SEM images of the cross-section of samples fabricated with various values of separation between filaments. These micrographs were used to calculate the void density of the printed samples based on an empirical model. Casavola et al. [74], obtained the elastic moduli from tensile tests of unidireccional fully filled samples. They obtained the longitudinal Young's modulus from samples were the filaments are aligned to the loading direction. They also measured the Poisson's ratio. They obtained the transverse Young's modulus of filaments running parallel and bonded together by testing them in a direction perpendicular to

that of the filaments. They measured the shear modulus from tests on parallel filaments oriented at 45° from the loading direction. The laminate model was used to predict the Young's modulus of a sample fabricated with the following stacking sequence [30°/-30°/0°/-30°/30°]. The model showed a good agreement within 6.6%. Similarly, Ziemian et al. [75] used CLT fabricated from unidirectional samples to predict the effective stiffness. Additionally, the tensile fatigue life of FFF-samples was studied in [75]. For the fatigue tests bi-directional samples showed fatigue behaviour similar as that of reinforced composites. The main fatigue damage observed were filament cracking, delamination, and void geometry changes.

Classic laminate approaches are restricted to parts fabricated with negative or zero separation between filaments. Kulkarni and Tutta [72] and Li et al. [73], both accounted for the effect of the inevitable voids on the stiffness of the printed parts by calculating stochastic factors in their formulations. The approach of Casavola et al. [74] and Zeiman et al. [75] was limited to parts fabricated with 100% infill, no separation between the extruded filaments was specified. To obtain the complete stiffness matrix, the Young's moduli of a single layer in the longitudinal and transverse directions of the filaments are needed. The stiffness in the transverse direction is only obtained when the filaments within the layer interact, i.e when they are bonded in the plane. The prediction of the mechanical properties using CLT fails when filaments are extruded with a gap between each other as the stiffness in the transverse direction vanished [76]. Other analytial models that rely on filaments that are bonded within the layers can be found in [77, 78]. Croccolo et al. [77] proposed an analytical model to characterise parts fabricated with zero separation between filaments extruded at 45° with respect to the loading direction. The model was based modelling the inclined filaments as inclined truss members. Huang and Singamneni [78] studied the sensitivity of the effective stiffness and strength on unidireccional samples fabricated with filaments at various angles. Huang and Singamneni proposed an analytical model based on the plane stress response of layers of filaments bonded in a plane. Because that filaments are bonded within the layer, Huang et al. considered the filaments cross-sections to be square with elliptical fillets in their analysis. On the other hand, Wang et al. [79] aimed to reduce the voids in the FFF-part by adding thermally expandable microshperes and adding thermal treatment to the FFF procedure.

An increment of 25.4% and 52.2% was observed for the tensile and compressive strengths respectively. Another attempt to improve the mechanical strength of FFF-components was made by Weng et al. [80]. They prepared parent material filaments made of a combination of ABS and montmorillonite. The inclusion of montmorillonite increased the tensile strength by 43%.

Domingo-Espin et al. [81] took a different approach. They carried out experimental characterisation of the orthotropic elastic constants of FFF-printed samples. Domingo-Espin et al. [81] implemented these constants in computational models to predict the mechanical response of structural elements. These procedures [72–75, 81] are functional, and applicable to parts fabricated with complex nozzle trajectories, stacking sequences, or parts with 100% of infill and/or no control of the nozzle trajectories. However, they lack the understanding of the role of lattice architecture on the mechanical properties of the frabicated part. Any change in the structural parameters requires experimental characterisation of the elastic constants in order to be able to feed the CLT and FEA models. The research work carried out here accounts for these, since the analytical models of apparent properties are developed as function of the structural parameters.

Different deposition trajectories will produce parts with varying mechanical properties, even if the macro shapes and dimensions are the same. The influence of the micro-architecture present in FFF-parts motivates the present research. In the next chapter the procedure to manufacture FFF-lattices is described.

2.6 Conclusions

In this chapter, the relevant background on the manufacture, and mechanical properties of lattice materials was reviewed. Several methods to produce structured media were described including that of additive manufacturing. While several laser based AM techniques have been employed to produce lattices with complex architectures, the use of extrusion based AM techniques will inevitably produce parts composed of the woodpile architecture. A thorough understanding of the apparent mechanical properties of the woodpile arrangement is still an open issue. The woodpile architecture has been studied

in the past primarily via experimental and numerical methods, mostly using compressive loadings. While works on the study of the shear modulus, and flexural properties are scarce, the torsional properties are studied here for the first time.

Chapter 3

Controlled manufacture of lattice materials using fused filament fabrication

Additive manufacturing (AM) or rapid prototyping (RP) is a solid free-form fabrication process that is used to create three-dimensional objects by adding material layer-by-layer. Originally, the application of parts fabricated using these techniques was mainly in assemblies for interference and dimensional checking. Recently, the fabricated parts have been used not only as prototypes but also as final and ready-to-use components. The capability to control the material deposition can lead to the fabrication of parts with tailored mechanical properties. This feature makes AM techniques promising for the fabrication of lattice materials. Among the rapid prototyping techniques, *fused filament fabrication* (FFF) is employed in the current research. Parts fabricated with this technique are likely to have porosity due to the manner in which the material is deposited. Changing the deposition strategy directly affects the porosity which, in turn, influences the apparent mechanical properties. This chapter describes the controlled deposition of matter in the FFF process in order to achieve the fabrication of lattice materials with pre-specified structural parameters. A bespoke strategy for controlling the internal architecture has been developed in this work and discussed later.

3.1 A comparative assessment of various additive manufacturing techniques

Several AM techniques were discussed in the previous chapters. Here we compare and contrast their relative advantages, limitations and also applicability depending on the industrial context. The nature of the manufacturing process has a significant impact on the properties of AM manufactured materials and structures. Aspects of manufacturing are speed, accuracy, processing temperature, properties, cost, materials, among others. The selection of an AM process depends on the intended application, and available resources.

A technique known as *three-dimensional printing* (3DP) consists of a powder bed and an inkjet print head. The inkjet head prints droplets of a binder fluid on to the powder bed. The powder contains a plaster that is activated with the binder. The location at which the head prints the droplets is controlled. Once, one of layers is completed, the machine adds another layer of powder and the process is repeated. The printed part is then built by stacks of layers formed over each other [82].

Selective laser sintering (SLS) also uses a powder bed. In this case, instead of a binder, a laser is used to sinter the powder material. The possibility to produce metallic parts makes SLS popular among the AM techniques. The 3D part is fabricated by a controlled aiming of the laser. This technique is similar to that of *selective laser melting* (SLM), the difference is that in the latter, the material is fully melted instead of sintered. *Electron beam melting* (EBM) is another technique that utilises melting of material, where metal is welded or bound together by the use of an electron beam as heat source. The key is the controlled trajectory of the electron beam [27]. The use of laser is also found in *stereolithography* (SLA). The production of parts using this technique is based on photopolymerisation [83]. A controlled projection of an ultraviolet laser is performed on liquid photopolymers. The laser initiates the solidification of the photopolymer forming a single layer of the component. The repetition of the process forms the 3D component from the pile of layers.

Another alternative, beside powder and laser techniques, is to use an extruder through which the material could be pushed out. The location of the deposited material is controlled. The 3D part is built by stacking the layers of extruded material. *Robocasting* (RC) is an extruder based technique that works with ceramic cast or slurry. The slurry is pushed out through the nozzle in liquid state, but the extruded shape is maintained due to the shear thinning. Shear thinning is the phenomena in which the viscosity of a liquid decreases due to the influence of stresses. Another extrusion based technique is *fused filament fabrication* (FFF). In this, the material is extruded in semi-molten state and then it solidifies while bonding to the adjacent filaments.

Fused filament fabrication machines are significantly cheaper when compared to other AM machines. An example of this is the *RepRap* Project [84], where it is possible to build a functional 3D printer from about £400 [85]. Reprap machines are built with parts that were fabricated with other printers, or with itself, making them very cheap [86]. On the contrary, 3DP, SLS or SLA can cost 500% more than a FFF machine [87]. The complexity of the fabrication process and the materials employed make the other options more expensive. Currently, many brands of FFF machines are so easy to use and to transport that they can be used now from home [88, 89], while other alternatives require large space only found in research laboratories or industry.

Stereolithography is limited to the processing of photopolymeric materials, whereas a range of polymers, metals [90] and even edible materials such as chocolate [91] have been printed using FFF machines. Stereolithography offers the best results for the surface quality of the printed part and resolution–being capable of printing features of $\approx$ 20 μm [92]. While in FFF some of the smallest attainable features are within the range of 50 μm-200 μm, and depend on the hardware e.g. nozzle dimensions, material, and manufacturing parameters, such as nozzle traverse speed, building temperature, and layer increment.

Selective laser sintering, as opposed to SLA, FFF, and RC, does not use support structures to fabricate components with overhangs. The reason is that during the fabrication process, the component is enclosed by unsintered material [93]. The main fabrication disadvantage of SLS, is that it cannont produce hollow and fully enclosed components.

The powder chamber is always filled with material, leaving unsitered material that is not possible to remove from the inside of the intended component.

Robocasting and FFF can produce parts composed of the same material arrangement. This arrangement consists of the stack of extruded filaments. In contrast with FFF, RC has the advantage that it can manufacture porous structures without the use of high processing temperatures. Robocasting is restricted to ceramic slurries as parent materials, while FFF can employed a range of materials already mentioned. Robocasting enables manufacturing with smallest filaments having rod diameter in the range: 200 μm-400 μm. On the other hand, FFF can employ nozzles with extrusion diameters in the range of 250 μm-800 μm [94]. RC-parts are commonly exposed to post-processings, such as drying, and debinding, increasing the fabrication time. A comparison of various AM techniques is summarised in Table 3.1.

3.2 The fused filament fabrication process

Fused deposition machines comprise a heater block, an extruder (nozzle) and a platform. The parent material is drawn into the heater block and partially melted. The material is extruded through the nozzle in the form of a cylindrical filament which is deposited on the platform. Servo-motors control the location of the nozzle to form the first 2D profile according to the instructions provided by the *G-code*. G-codes consist of lines of instruction containing the coordinates to be followed by the nozzle. Once a layer is extruded, the nozzle is shifted from the platform for the next layer of material to be extruded. The procedure is repeated until the 3D part is completed. A schematic representation of the FFF process is presented in figure 3.1, note the filaments are depicted as cylinders.

A conventional process to manufacture a part with FFF machines consists of the following steps. First, a CAD model of the part to be printed is created and exported as a *.stl* file, as required by most of the 3D printers software. The software then slices the model, into 2D profiles of the part and generates the nozzle trajectories accordingly these trajectories are expound in the G-code. The 3D part is created by means of the

TABLE 3.1: Comparison of the main additive manufacturing techniques.

Technique	**Process description**	**Advantages**	**Drawbacks**
Three-dimensional printing (3DP) [94–96]	Powder is bound by means of binder fluid droplets building the solid part.	• No support structure required. • Wide range of materials.	• Powder trapped inside the printed part. • Limited to small pore sizes. • Use of toxic solvents.
Selective laser sintering (SLS) [94–96]	Laser beam is used to melt a layer of powder material.	• Good mechanical properties (compressive strength). • No support structure required.	• Powder trapped inside the printed part. • Uses high processing temperatures.
Stereolithography (SLA) [94–96]	Laser beam used to initiate solidification in a thin layer of liquid photopolymer.	• High accuracy. • High speed. • Smooth surface finish.	• Support structure needed. • Limited to photopolymer.
Robocasting (RC) [94–96]	Robot controlled nozzle deposits a cast or slurry layer by layer.	• Combination of materials. • No support needed.	• Poor build time. • Material limited.
Fused filament fabrication (FFF) [33, 63, 64, 66, 69, 97–99]	Thermoplastic material is heated and extruded via a nozzle layer by layer.	• Economic affordability. • Wide range of materials.	• High processing temperatures. • Anisotropic parts.

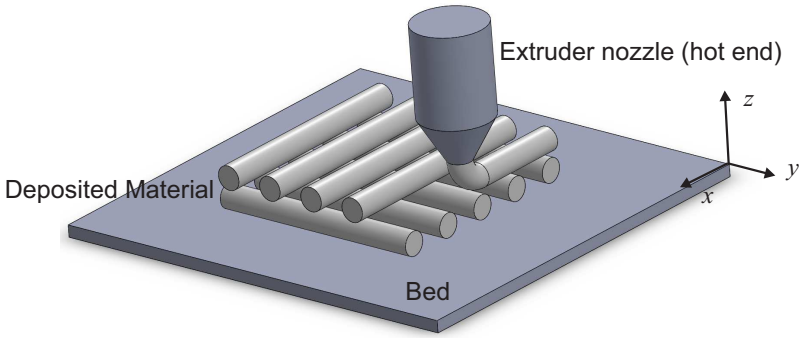

FIGURE 3.1: Schematic representation of the fused filament fabrication process.

stack of these layers of 2D profiles. A typical line of G-code is shown in figure 3.2. The numbers next to each label axis X, Y and Z indicate the corresponding coordinate, while 'G1' is the command for linear movement. Other parameters can be found in lines of G-codes such as F nozzle traverse speed, and E extrusion constant.

G1 X12.3 Y32.1 Z0.12

FIGURE 3.2: A typical line of G-code, G1 indicates linear movement, then the numbers next to X Y Z indicate the coordinate position at each axis respectively.

Each slice of the intended part to fabricate consists of the distribution of the extruded filaments. This arrangement of filaments is normally controlled with the software interface by adjusting the density of the part. The arrangement of filaments forms the 'skeleton' of the printed part and it is known as *infill*. FFF-manufactured parts rarely have 100% infill, as this offers several advantages, such as reduction in fabrication time, and material used. The fabricated parts will result with a lattice arrangement of filaments forming the infill of the part. An example of this infill was shown in Chapter 1 in figure 1.3.

Different patterns can be used as infill, two examples are shown in figure 3.3. The infill on the left consists of a square honeycomb, while the one on the right is a hexagonal honeycomb. The infill is automatically generated by the 3D printing software, and the decision of what pattern to use is usually specified by the user. Some softwares allow the user to decide the type of pattern, but others simply allow you to control the density. The two infills shown in figure 3.3 can be seen as the square and hexagonal lattices described in Section 2.2, where clear differences in their mechanical response were brought out.

This enhances the importance of characterising the mechanical properties of the infill, the two examples shown will have significant different apparent properties for parts printed with the same density. The infill on the left is stretch-dominated when the load is applied along one of the filaments axis, while the infill on right is bending-dominated. In order to best exploit the feature of the FFF process to fabricate parts with controlled mechanical properties, this internal structure needs to be controlled.

FIGURE 3.3: Two examples of conventional infills patterns that can be found in FFF-parts [12].

Since the main objective of this thesis is to study the property-structure relation, a script was developed to fabricate the samples with controlled nozzle trajectories, having full control on the structural parameters. This method will allow us to have full control on the resulting infill structure and it is described next.

3.3 Generation of G-codes

G-codes contain not only the coordinates at which the nozzle extrudes the filaments, but also some of the initialising manufacturing parameters, i.e. temperature of the nozzle, bed temperature, speed of the nozzle, fan controls, extrusion speed, among others. All of these are generated by the 3D printer software, which does not allow a control on the structural parameters of the infill. In order to study the property-structure relation of the FFF-parts a full control of the filaments extrusion location is required. Hence,

to achieve control on the G-code, a script was developed in MATLAB. The output of the script developed produces an ASCII file containing the G-code instructions. The MATLAB script uses the following set of desired structural variables as input:

- Number of filaments parallel to the x-axis, N_x.
- Distance between the filaments parallel to the x-axis, λ_x.
- Number of filaments parallel to the y-axis, N_y.
- Distance between the filaments parallel to the y-axis, λ_y.
- Number of layers, N_z.
- Distance between each layer in the z-axis, λ_z.

Each of these structural parameters can be seen in figure 3.4 where a schematic diagram of extruded pattern of filaments is presented.

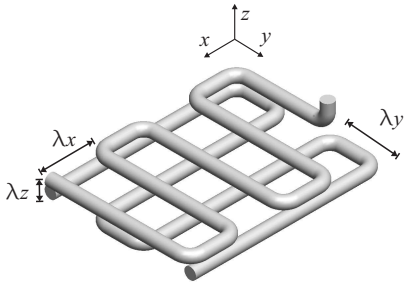

FIGURE 3.4: A representation of some extruded filaments product of the nozzle displacement, showing the variables that are controlled in the program that generates the G-code.

The G-code is obtained as an output of a bespoke MATLAB code developed as part of this work. The G-code generated is then used to computationally simulate the tool path to ensure that correct trajectories are generated. The simulation of nozzle toolpaths can be done with available software, such as Axon 2® or Repetier®. Stages of the complete manufacturing process are summarised in figure 3.5. A section of the G-code generator (MATLAB code) is shown in Frame (a) of figure 3.5. The generated G-code is shown in Frame (b). The G-code checked in the printer simulator Axon 2®, and the resulting 3D printed physical part are presented in Frames (c) and (d) respectively. The G-code

generator along with an example of G-code obtained can be found in Appendixes A and B. The effectiveness of the procedure just described is brought out in the next section with examples of some of the lattices fabricated and actual testing samples.

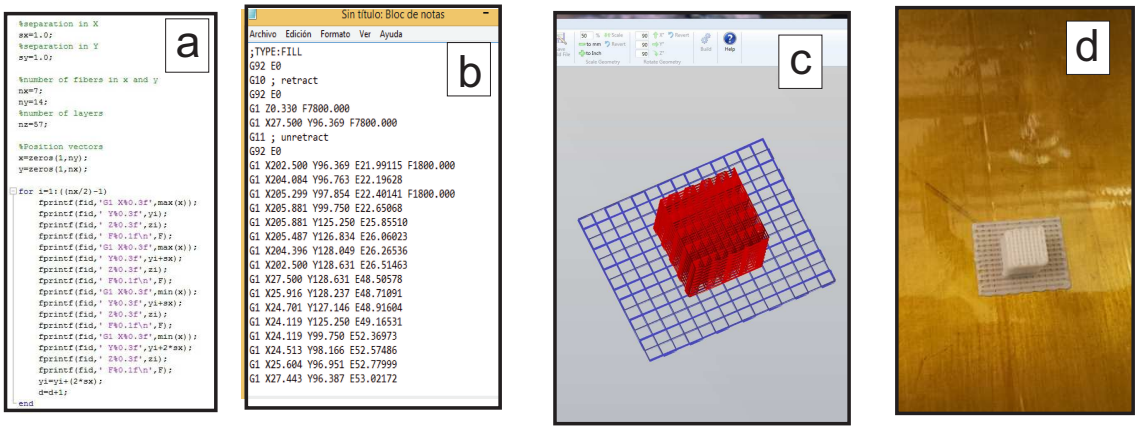

FIGURE 3.5: Manufacturing process employed. (a) G-code generator in MATLAB. (b) G-code generated. (c) Simulation of the G-code desired part on the computer. (d) Physically printed part.

3.4 Lattices and samples obtained

Lattices and testing samples were fabricated using the bespoke G-code generator introduced in the previous section. In this section, we present examples of such structures manufactured. First, we provided a brief introduction of the parent material employed for the fabrication.

3.4.1 Polylactic acid

A material commonly used with FFF manufacturing techniques is the *polylactic acid* or *polylactide* (PLA). Polylactic acid is a biodegradable polymer approved by the Food and Drug Administration [100]. This polymer has high mechanical strength, and low biotoxicity [101]. A comparison against other polymers such as: polyethylene terephthalate (PET) and polystyrene (PS) can be found in [101]. For tensile modulus and flexural modulus, have a higher value for PLA than for PS. It has, however, lower melting point than PET and PS. The last characteristic makes it suitable for heat-sealing and thermal applications.

Due to its superior recycling and degradation characteristics, some applications of PLA include packaging, transportation, building, houseware, together with biomedical applications [101]. In case of the last, it can be used for implants in different forms, such as screws, rods, and/or scaffolds [102]. The Food and Drugs Administration's approval makes PLA a promising material for packaging and therefore suitable for transporting food [101]. A good mechanical understanding of the PLA-based structures will improve existing products and will point towards new applications. In this work, white PLA filament from the manufacturer *KDI* Polymer Specialists Ltd®, is the material used to fabricate the lattices and samples studied.

3.4.2 Machine description

BFB 3D Touch® 3D printer was used for the fabrication of the samples used later in the mechanical tests. The machine is shown in the photograph of figure 3.6. As described earlier, each layer deposition trajectory is controlled with the location of the nozzle in the XY plane. The location is guided with the use of a set of stepper motors (M42STH47-158445C), and toothed belts, one for each axis. Additionally, the adjustment of the printing platform position permits changes in the z position resulting in parts formed by the stack of layers. The z position is controlled with another stepper motor (M57STH51-3008DC) and a ball screw that position the platform at different heights. The material extrusion is controlled with the same type of stepper motor used for the position in the xy plane. The filament is fed through a plastic tube and fit directly to a moving head. This moving head contains the nozzle and a screw to drag and push the filament into the nozzle. The main components of the BFB 3D printer are labelled in figure 3.6 with yellow arrows, while the axes are indicated with white arrows.

3.4.3 Micro-architecture formed

The cross-sectional area of the filaments and the micro-architecture formed in FFF can be observed in the SEM micrographs of figure 3.7(a) and 3.7(b) respectively. To observe the stacking of filaments and adhesion at the interface of alternating layers, the sample was fractured by dipping it in liquid nitrogen and impacting. Figure 3.7(b)

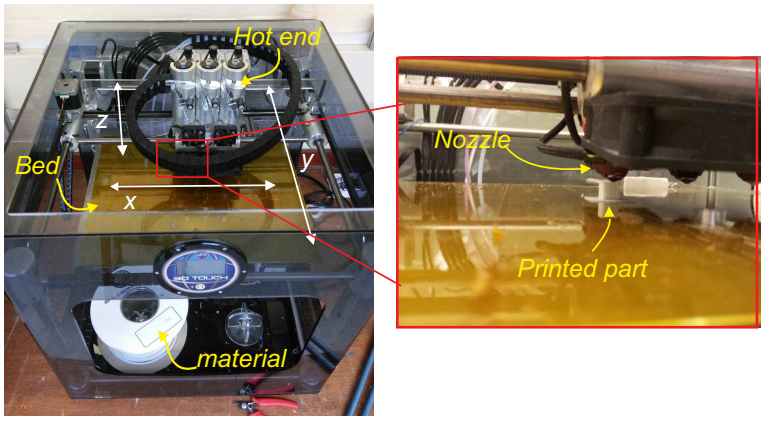

FIGURE 3.6: A photograph of the FFF machine employed in within this work, showing the principal parts and the axes direction.

indicates that the stacking sequence of filaments results in a structure formed in the so-called woodpile arrangement. Due to the change in temperature from the extruder to the printing environment, the filaments expand forming an ellipsoidal cross-sectional area. When a filament is deposited, the temperature at the interface in contact with the filament previously deposited is above the material glass transition temperature. This condition favours the rapid development of adhesive bonds [103]. These bonds of "welded material" can be observed in micrographs presented in figures 3.7(c) and 3.7(d). The formation and resulting properties of the adhesive interface are research areas that are beyond the scope of the present work [73, 103–105]. Some of the important findings in studying the interface between adjacent filaments is that it results with properties different from those of the parent material [73, 105]. In order to understand the apparent mechanical properties of FFF-components, we assume that the parts have perfect bonds (same mechanical properties as the constituent filament material). In the computational models the bonding between filaments is represented as an overlap between their volumes.

The FFF-parts can be considered to be made up of a lattice material formed by the stack of filaments. This lattice material is shown in figure 3.8 having the filaments represented with cylinders. The relative density is calculated from the repetitive unit cell shown in figure 3.8. Recall that the relative density is equal to the volume fraction, $\bar{\rho} = V_s/V_c$. For the geometry under consideration, $V_s = \pi r^2(\lambda_x + \lambda_y)$ and $V_c = 4r\lambda_x\lambda_y$, therefore the relative density is obtained as,

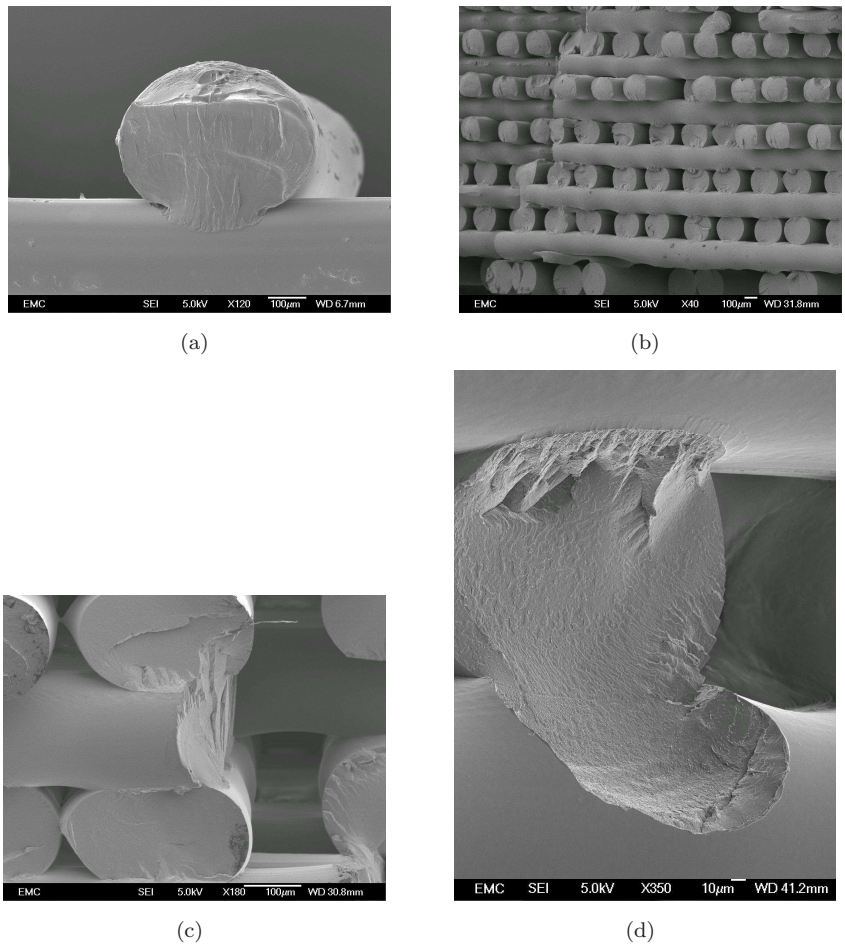

(a) (b)

(c) (d)

FIGURE 3.7: SEM images of (a) cross-sectional area of a filament, (b) the resulting microstructure consisting of the stack of filament in the woodpile architecture, and (c)-(d) closer look at the bonding between adjacent filaments, the full diffusion can be observed.

$$\bar{\rho} = \frac{\pi}{4} \frac{r}{\lambda_x \lambda_y} (\lambda_x + \lambda_y) \tag{3.1}$$

for the square lattice i.e. $\lambda_x = \lambda_y = \lambda$ the expression for the relative density simplifies to $\bar{\rho} = \pi r / 2\lambda$. The reduction in the volume due to the overlap is not considered in the calculation of the volume fraction. The filaments are assumed to be bonded at a point in the expression in equation (3.1).

3.4.4 Lattices fabricated with controlled structural parameters

Several G-codes were generated by changing some of the structural parameters. Three resulting porosities are shown as examples in figure 3.9. The lattice in figure 3.9(a),

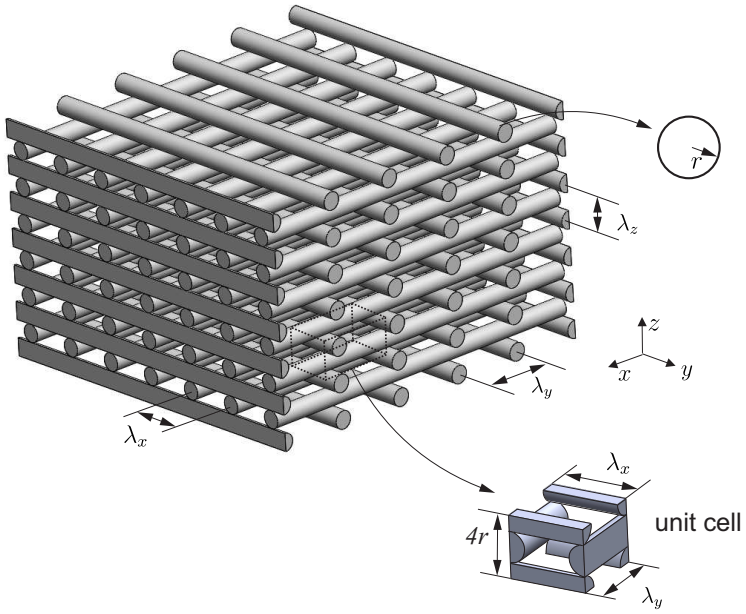

FIGURE 3.8: Schematic of the lattice material formed with the FFF process, and the unit cell used to calculate the relative density. The figure shows the parameters nomenclature to be used trough the rest of the document.

was fabricated with an overhang between filaments specified as $\lambda_x = \lambda_y = 1$ mm. The parameters specified for the lattice in figure 3.9(b) and 3.9(c) were: $\lambda_x = 1$ mm, $\lambda_y = 2$ mm, and $\lambda_x = \lambda_y = 2$ mm, respectively. The rest of the fabrication parameters were kept constant for the three examples presented. Only lattices with the filament axes parallel to the x- and y-axes of the machine were fabricated in this case, but the method presented here can be easily adapted to fabricate many other configurations, e.g. filaments oriented at 45°. Current research is focused on several orientations of the filaments, where the samples were fabricated using the G-code generator developed here. The customised G-codes can be used to produce tailored infills for FFF parts. The approach presented here is an important contribution to develop parts with controlled porosity and, therefore, tailored mechanical properties.

3.4.5 Samples fabricated for mechanical testing

We have shown the correct functioning of the G-code generator in the previous section. The next step towards the study of the structural-property relation of the FFF-lattices is to fabricate samples for mechanical testing. These samples are composed of filaments

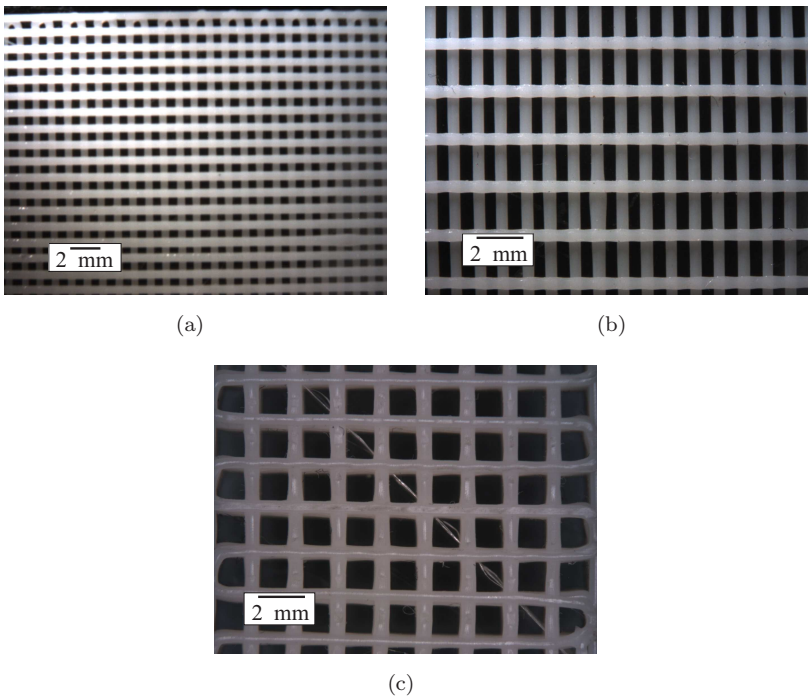

(a) (b)

(c)

FIGURE 3.9: Macroscope images of different porosities obtained by controlling the G-code (a) 1×1 mm corresponding to a $\bar{\rho} = 0.39$, (b) 1×2 mm corresponding to $\bar{\rho} = 0.29$, and (c) 2×2 mm corresponding to $\bar{\rho} = 0.19$.

in the woodpile arrangement. The specific orientation of the filaments is described in turn.

When the dimensions of the parts to be fabricated are considerably long, the adhesion to the printing platform becomes critical. While printing, long parts are likely to be detached from the platform before the printing is completed. To avoid this, the samples were fabricated with a *raft* base. This raft ensures the adhesion of the part to the platform and gives it structural support while printing. It consists of two extra layers added to the actual part, as shown in figure 3.10. These two layers are printed first. Once the printing is completed the raft is manually removed from the samples.

The dogbone shape for the samples used in the tensile testing can be observed in figure 3.11(a), the plane of the paper corresponds to the xy-plane of the printer. The dimensions for the samples were followed according to the ASTM-D638 standard and are presented in figure 3.11(b). The samples were printed so that they lie on the xy-plane, which makes the thickness of the samples to be given by the stack of filaments. The orientation used was such that filaments were aligned to the x- and y-axes of the machine.

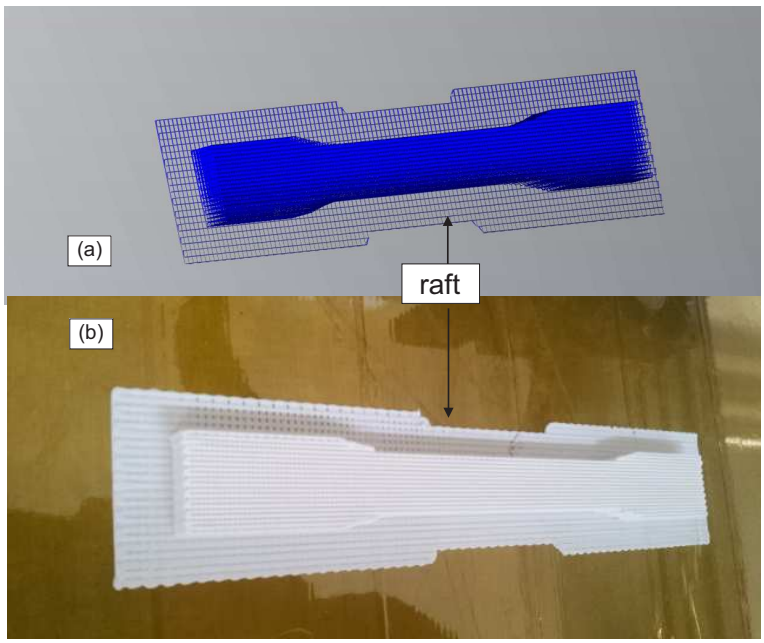

FIGURE 3.10: Screen-shot of the (a) tensile sample manufacturing simulation to ensure the correct trajectory of the nozzle generated, and a photograph of the (b) physical tensile sample obtained right after the printing process finished. Note the raft layers indicated, these layers are printed to ensure the adhesion to the bed as well as to bring support for the actual printed part.

The x-axis of the machine is parallel to the length of the samples. The orientation of the filament within the samples is depicted in figure 3.11(c). The cross-section of the samples is shown in the schematic of figure 3.11(d), showing the stack of filaments.

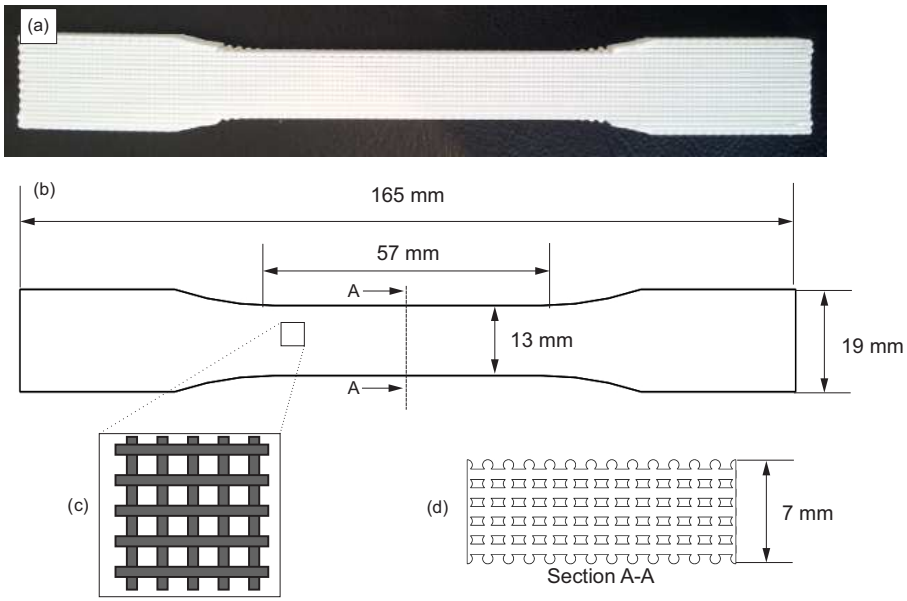

FIGURE 3.11: (a) Photograph and (b) schematic with the dimensions of the samples fabricated for the tensile testing under the ASTM-D638. (c) The orientation of the filaments within the sample and (d) the cross-section of the samples.

The samples used to study the flexural properties of the lattice material were fabricated following the ASTM D790 standard (standard for flexural properties of polymers). A photograph of the sample is presented in figure 3.12(a), the plane of the paper corresponds to the xy plane of the printer. Some modifications were applied to the width dimensions proposed in the ASTM D790 standard. The width was deliberately increased to 25.5 mm instead of the recommended value of 12.7 mm in order to ensure that the width is significantly greater than the characteristic lattice dimensions. Otherwise, the lattice material could not be treated as apparently homogeneous and significant end effect will be present in the measurements. The dimensions are presented in figure 3.12(b). The orientation of the filaments is shown in figure 3.12(c) and the cross-sectional in figure 3.12(d).

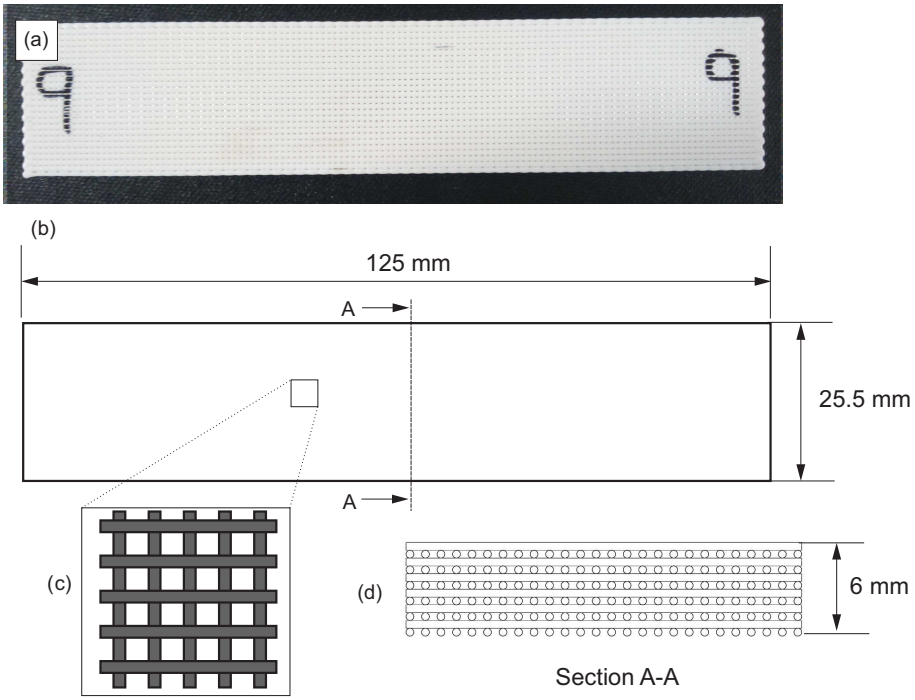

FIGURE 3.12: (a) Photograph and (b) schematic with the dimensions of the samples fabricated for the three-point bending. (c) The orientation of the filaments within the sample and (d) the cross-section of the samples.

A dog-bone shape was used for the samples used in torsional tests (figure 3.13(a)). The dimensions are presented in figure 3.13(b). The orientation of filaments and cross-section of the samples are shown in figures 3.13(c) and 3.13(d) respectively. For all the samples tested, the separation between the filaments was set the same in both axes as $\lambda_x = \lambda_y = \lambda = 1$ mm. The rest of the manufacturing parameters, such as, nozzle speed,

extrusion speed, and extrusion temperature, were kept the same for all the samples used in this work. These parameters were used from the default suggestions for conventional printing. These parameters are summarised in Table 3.2.

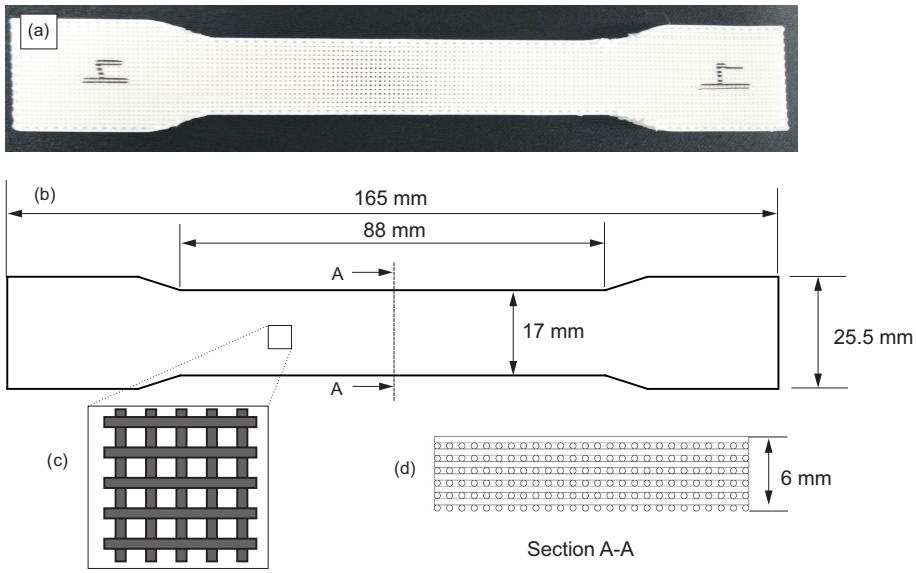

FIGURE 3.13: (a) Photograph and (b) schematic with the dimensions of the samples fabricated for the torsion tests. (c) The orientation of the filaments within the sample and (d) the cross-section of the samples.

TABLE 3.2: Samples and manufacture parameters.

Sample	**Nozzle Speed (mm/s)**	**Extrusion speed (rpm)**	**Raft Temperature (°C)**	**Extrusion Temperature (°C)**	**Total time (min)**	**Material used (g)**
ASTM D638	860	45	195	190	54	17.5
Flexural sample	860	45	195	190	58	18.5
Torsional sample	860	45	195	190	104	15.31

3.5 Conclusions

In this chapter the FFF technique was compared with other AM processes, highlighting some of the advantages of FFF and also its limitations. Then the benefits of controlling the porosity in FFF-parts was address. In this research, this was achieved by a customised generation of G-codes. One of the main advantages of controlling the nozzle trajectories is that the lattice infill is fabricated with desire structural parameters. This is a crucial step towards the the fabrication of parts with tailored mechanical properties. The micro-structural parameters affect the mechanical properties. The infill resulted to be in the so-called woodpile arrangement, and in this dissertation, we studied how the structural parameters affect the apparent mechanical properties of the fabricated part.

Samples for various mechanical tests were fabricated in a controlled manner using customised G-codes. The bespoke generation of G-codes enables the fabrication of parts where the number of filaments, their spacing, the number of layers in the stack, can be fully controlled. Other manufacturing parameters such as temperature, nozzle speed can be specified within the G-code. Following the G-code generation procedure presented in this chapter, there is no dependence on any CAD software to manufacture samples with simple geometry, such as the samples for testing. A 3D printer simulation software however was used to ensure that the correct trajectories were generated before commencing the printing process in order to avoid any possible machine damage.

In the literature review, several works that considered the directional dependence of the woodpile lattice material were mentioned. This dissertation is focused on the orientation where the filaments of adjacent layers are orthogonally oriented and aligned to the length and width of the samples. The loading conditions considered her, however are complex and relevant to many practical slender engineering structures. The flexural and torsional properties of the 3D printed lattice structures were studied on samples having their thickness in the z-axis. The number of layers is much less than that of the filaments parallel to the x- and y-axes. In the following chapter, the analysis of the apparent Young's modulus when the load is aligned to one of the filaments axis is addressed.

Chapter 4

Tension of the woodpile lattice material: the apparent Young's modulus

The stiffness of the structure having woodpile arrangement when it is loaded along one of filament axis is studied here. The elastic properties of the parent material (PLA) are characterised first. The characterisation of PLA is done through tensile tests on single FFF-filaments. An analytical prediction based on the rule of mixtures is developed and compared with both computational and laboratory experiments.

4.1 Properties of the parent material: single filament characterisation

In this work, a hierarchical model of the lattice architecture is proposed. The first step in this direction is to characterise a single filament that compose the lattice material. The experimental characterisation is done using laboratory testing so that the data could be imported into computational and analytical models subsequently. Single filaments were fabricated under the same manufacturing conditions as those for the fabrication of the lattice samples. These process conditions were listed in Table 3.2. A set of 10 samples

were subjected to tensile loading using the Deben MICROTEST® module. The description of the testing module used and the measured data for stiffness characterisation of these filaments are presented next.

4.1.1 MICROTEST Module Description

The Deben MICROTEST® module was originally designed for testing and live monitoring of samples while taking SEM micrographs. The device fits inside the SEM chamber; this evidences the handling dimensions capabilities of the module. The complete set-up of the module is shown in figure 4.1. It consists of the controller unit, a PC, and the testing module. The testing module is connected to the control unit and also to the PC. The tensile test stage is shown in detail in figure 4.2, where the two simple screwed-fixing clamps are indicated by the yellow arrows. The minimum distance between the clamps is 10 mm and the maximum distance after travel is 20 mm giving a maximum total travel distance of 10 mm. The device has a loadcell of rating 300N, giving it superior sensitiveness in measurements than INSTRON machines used later for the complete lattice testing; these are within the range of 2kN and 50kN.

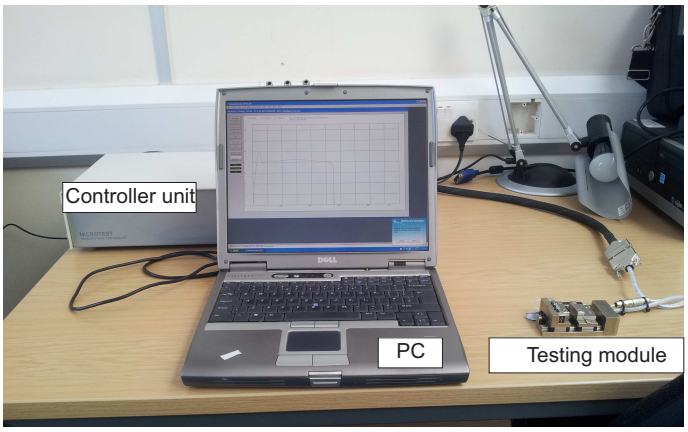

FIGURE 4.1: A photograph of the set-up for the single filament testing. Showing the control unit, the computer, and the micro-testing device.

The software allows live monitoring of the extensional response. The force-elongation curve can be observed while the samples is being loaded. Within the software interface, several settings exist to adjust the resolution in the results, such as the sampling time, motor speed, vertical axis scale, etc. Once the sample has been properly clamped, the motor moves the clamps in the direction indicated in figure 4.2. The data for force and

elongation can be exported in an ASCII file for further processing to get the *stress-strain curve*. From this, properties such as the Young's modulus, the strength, etc. can be found. In order to achieve this, the cross-section area of the filaments cross-section needs to be known. In the next section, a description of the measurements of the cross-sectional area of the filaments is presented.

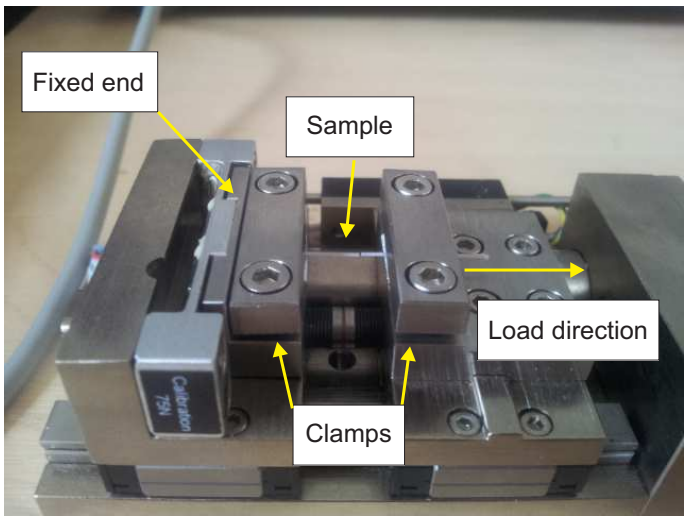

FIGURE 4.2: A photograph of The Deben MICROTEST® module. Showing the fixed end, the clamps, and the load direction. A sample of a single filament after failure is shown.

4.1.2 Characterisation of the cross-sectional area of filaments

In order to obtain the stress and the corresponding strain, the force needs to be divided by the cross-sectional area of the filaments and the elongation is divided by the original sample length. The area was characterised using images from the *MakroSkope M420*. The cross-sectional area of each of the 10 single filaments fabricated was measured prior to the tensile testing. The shape of the cross-section was then treated as an ellipse (see figure 3.7(a)). The area of an ellipse is given by

$$a = \pi \left(\frac{h}{2}\right)\left(\frac{b}{2}\right) \tag{4.1}$$

where h and b are the major and minor axes of the ellipse. The major and the minor axes of the cross-sectional area of 10 different samples were measured. Then using equation (4.1), the area was calculated and summarised in the second column of table 4.1. The

resulting mean area was calculated as $a = 0.302 \pm 0.017$ mm^2. This area was then used to obtain the stress-strain curves presented in the next section.

4.1.3 Tensile test results of the single filaments

A set of 10 filaments, like the ones shown in figure 4.3, was subjected to tensile loadings. The filaments were between 25 and 30 mm long and were glued to aluminium plates at the ends. The purpose of the plates is to ensure a better gripping of the sample to the clamps. The stress-strain curves were calculated after using the cross-sectional area information and the gauge length of the samples in conjunction with the force-elongation data. The stress-strain curves for all the samples tested are presented in figure 4.4. The values for elastic modulus obtained from the stress-strain data measured for individual filaments are summarised in table 4.1.

FIGURE 4.3: A photograph of single filaments glued to the clamping aluminium plates.

The elastic region in the linear part of the stress-strain curve shows some consistency among all the samples tested. The average Young's modulus was measured $E = 2.29 \pm .315$ GPa. The tensile strength and fracture stress, however, are scattered. Variations in the cross-sectional area can be present due to manufacturing inaccuracy. These defects cause variations in tensile strength and strain at failure. Some of these defects can be bubbles due to the moisture accumulated in the nozzle. When the nozzle is heated, the moisture is released as bubbles and cavities are formed within the filament. Another type of defect is the imperfection of filaments attached to the bed. When detached from the bed, the roughness of the bed will be mirrored on the surface of the filaments.

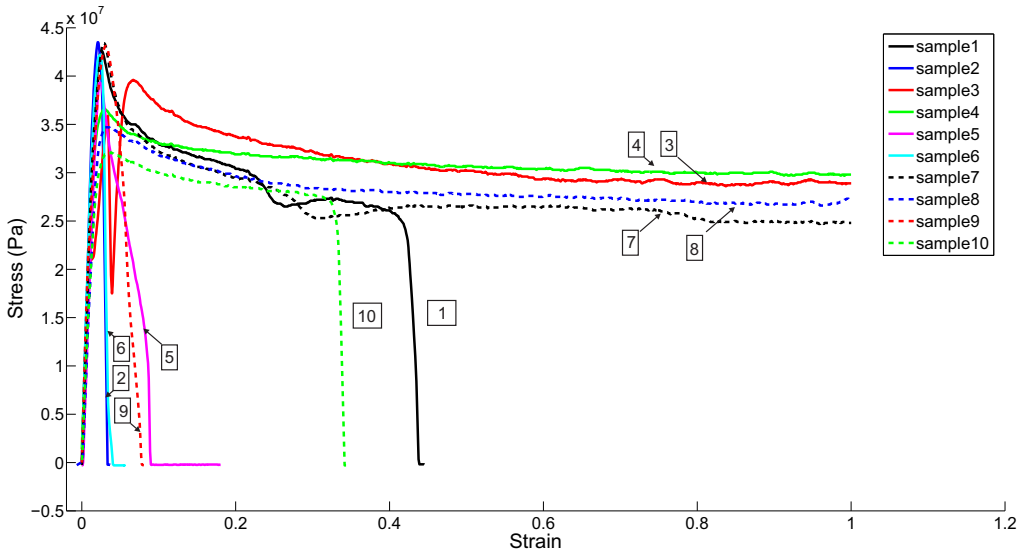

FIGURE 4.4: Stress-strain curves of the FFF manufactured single filaments. For convenience, numerical label with each curve indicate the sample number.

TABLE 4.1: Measured cross-sectional areas and experimental results for the elastic modulus of the single filaments (E).

Sample	**Cross-sectional area** (mm^2)	E (GPa)
1	0.328	2.65
2	0.321	2.65
3	0.306	1.95
4	0.304	2.12
5	0.288	2.24
6	0.272	2.64
7	0.318	2.54
8	0.299	1.92
9	0.303	2.41
10	0.276	1.79
Mean	0.302	2.29
St. dv.	0.017	0.315

An SEM micrograph of a single filament showing the defects just described is shown in figure 4.5. Improper clamping could led to the slipping of the sample, introducing error in the measurement of the elongation. Care was taken to prevent this. Conducting an experimental error analysis, the formula for the stress calculation $\sigma = F/\pi r^2$, assuming a perfect circular cross-section of radius r resulted in an expression for the percentage error: $|\mathrm{d}\sigma/\sigma| = |\mathrm{d}F/F| + 2|\mathrm{d}r/r|$. Note the factor of 2 that appears with the radius term resulting in *twice* the overall percentage error in the stress calculation. If the cross-section is treated as an ellipse instead, the formula for stress changes to $\sigma = F/\pi hb$, where h and

b are the major and minor radii of the ellipse, we obtain $|\mathrm{d}\sigma/\sigma| = |\mathrm{d}F/F| + |\mathrm{d}h/h| + |\mathrm{d}b/b|$ where the errors in the measurements of the minor and major axis of the ellipse will add up affecting the final percentage error [33]. The average elastic modulus of PLA, is used later to predict the apparent properties of the lattice material in the analytical and computational models. In the next section, we study the apparent elastic modulus $\langle E \rangle_{\parallel}$ when the load is applied along one of the filament direction.

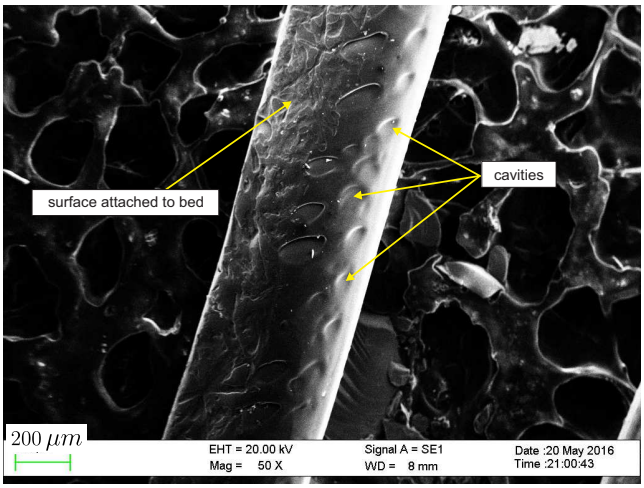

FIGURE 4.5: SEM micrograph of a single filament, showing the irregularities in the surface due the manufacturing process. The porosity observed in the background of the micrograph is the surface to which the filament is attached.

4.2 Tension of woodpile structures: apparent Youngs modulus along the filaments

Consider a woodpile lattice, such as the one shown in figure 4.6, when viewed in the direction of the stacking. A remote stress σ_∞ is applied along one of the two principal filament directions. The applied load is carried by the filaments parallel to the loading direction and the filaments across the loading are strain-free. This suggests that the apparent Young's modulus $\langle E \rangle_{\parallel}$ is a function of the fraction of the filaments carrying load over all the piece of lattice material. If the filaments across the loading direction do not participate in elastic deformation, the apparent Young's modulus must follow the rule of mixtures,

$$\langle E \rangle_{\parallel} = E\phi \tag{4.2}$$

where E is the Young's modulus of the parent material and ϕ is the fractional cross-sectional area exposed to tensile loading. In other words, the fractional area is the ratio between the actual total area of the cross-section of the filaments parallel to the loading direction, and the porosity filled area. The subscript $\parallel$ indicates that the property is that when the load is applied parallel to one of the filament axes. Expression (4.2) can also be expressed in terms of the relative density of porous material [8, 55]

$$\langle E \rangle_{\parallel} = \frac{1}{2} E\bar{\rho} \tag{4.3}$$

where the relative density $\bar{\rho}$ is equal to the volume fraction $\bar{\rho} = V_s/V_c$ calculated in Chapter 3 as $\bar{\rho} = V_s/V_c = \pi r/2\lambda$, so that $\langle E \rangle_{\parallel} = (\pi r/4\lambda)E$.

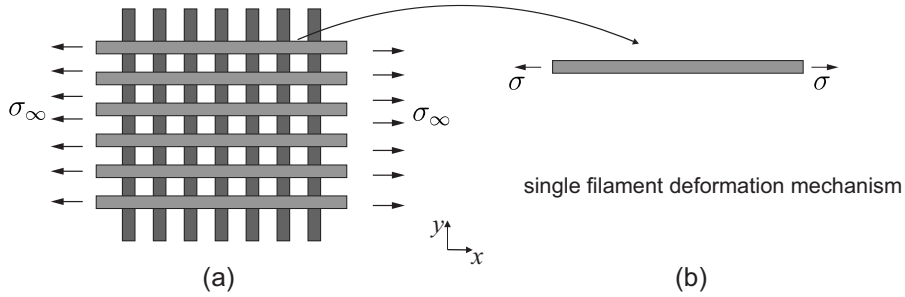

FIGURE 4.6: Schematic representation of (a) the lattice material subjected to remote uniaxial stress σ_∞, and (b) a single filament showing deformation mechanism under this load.

Note the factor of (1/2) in the expression for $\langle E \rangle_{\parallel}$ in equation (4.3) which, in the limit of $\bar{\rho} \to 1$, becomes $\langle E \rangle_{\parallel} \approx (1/2)E$. This seems to be inconsistent with the expectation that $\langle E \rangle_{\parallel} \to E$ in the limit. The apparent discrepancy is resolved when we realise that half of the material within fibres running orthogonally to the loading direction are unstressed for a square lattice. When the volume is imagined to be filled completely in the limit $\bar{\rho} \to 1$, this would not be the case. Thus the validity of expression (4.3) is limited to $\bar{\rho} < 1$ and when filaments are non-contacting. Equation (4.3) shows a linear dependence of the apparent Young's modulus on the relative density i.e. $\langle E \rangle_{\parallel} \sim \bar{\rho}$. This is expected because micromechanics involving stretch of filaments leads to stiffness that scales linearly with characteristic cross-sectional area, which in turn is proportional to

the volume fraction. Equation (4.3) is applicable only in the limit of the lattice being infinite, while equation (4.2) accounts for the finite number of filaments.

The apparent Poisson's ratio $\langle\nu\rangle$ results in 0 for this lattice material. This phenomena is due to the fact that the filaments perpendicular to the loading direction (y-axis in figure 4.6) remain stress-free. But at the same time keeping the separation between the filaments parallel to the load constant, results in no displacement in the perpendicular direction of the load, i.e. $\langle\nu\rangle \approx 0$. We proceed to compare expressions (4.2) and (4.3) with computational and laboratory experiments next.

4.2.1 Computational modelling and validation

Commercial finite element code Abaqus/CAE/Standard 6.13® (Simulia, Dassault Systmes, Providence, RI, USA) was used to calculate the response of a lattice under tensile loading numerically. A typical FE mesh is shown in figure 4.7. The filaments of the lattice were modelled as cylinders of diameter $d = 0.5$ mm and meshed using linear tetrahedral elements C3D10. PLA material properties were used. The values chosen here are $E = 2290$ MPa (measured from the single filament tensile tests), $\nu = 0.36$ [101]. Bonding between layers was represented by an overlap between the volumes of contacting cylinders that belong to adjacent layers. The overlap OL is defined here as the fraction of the centre-to-centre distance λ_z between adjacent cylinders and the cylinder diameter, given by $OL = (2r - \lambda_z/2)/2r$ (see figure 4.8). This fraction of OL is expressed here as the percentage of the described fraction. We used $OL = 8\%$ in the simulations presented in this chapter.

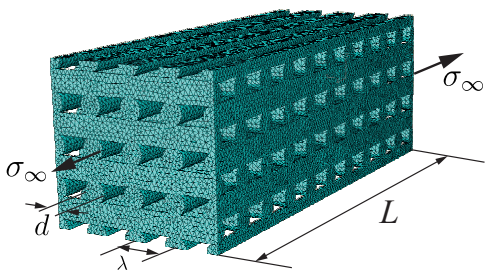

FIGURE 4.7: FEA model showing the loading direction and the mesh.

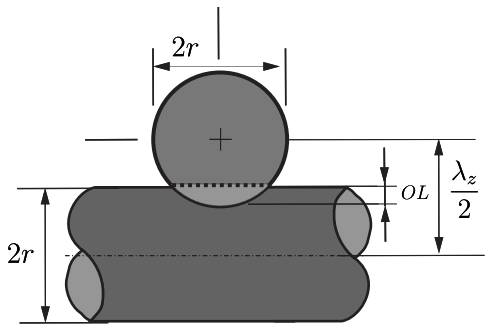

FIGURE 4.8: Schematic showing the definition of overlap.

A series of simulations with different relative densities were performed and the apparent Young's modulus $\langle E \rangle_{\parallel}$ was calculated. A unit distributed load was applied on all the nodes at one end of rectangular cuboid sample of the lattice material. The FEA samples shown in figure 4.7, consists of 16 axial and 24 transverse filaments. The relative density $\bar{\rho}$ was varied across the simulations by keeping the diameter of the filaments fixed and changing the separation between them λ. Each FE model contained about 800K nodes and 500K elements after ensuring convergence. The load applied was divided by the total effective area to obtain the apparent stress σ_∞. The displacement components at the end were averaged and divided by the total length of the bars L to obtain the apparent strain ε. The effective Young's modulus was then calculated using $\langle E \rangle_{\parallel} = (\sigma_\infty / \varepsilon)$. The process was repeated for several samples of varying relative density. The modulus of elasticity as a function of the volume fraction $\bar{\rho}$ is plotted in figure 4.9. There is an excellent agreement with theoretically predicted values of the modulus of elasticity using equation (4.3). The linear trend is consistent with the expectation for stretch dominated filament deformation. A single point of data coming from the laboratory experiments is also shown in figure 4.9, note a clear difference. The difference is attributed to the fact that equation (4.3) assumes the lattice to be infinite, for experimental data equation (4.2) shows better results, as it account for a finite number of filaments as shown in the following section.

4.2.2 Experimental testing of lattice rods in tension

The elastic response of rods having the woodpile lattice was measured experimentally. Works that deal with the elastic response of FFF-components were reviewed in Chapter

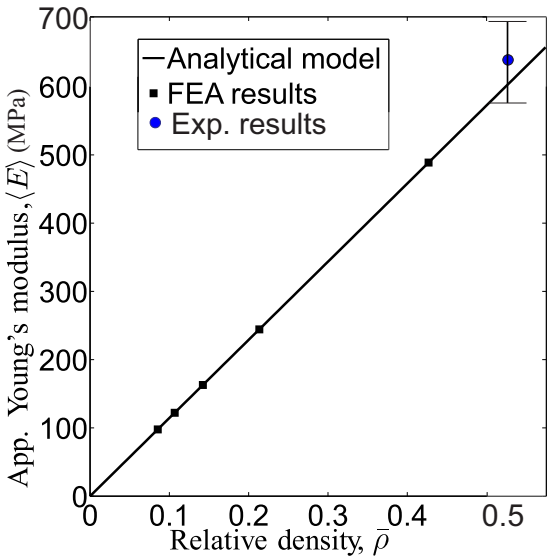

FIGURE 4.9: A comparison between the analytically predicted apparent Young's modulus $\langle E \rangle_{\parallel}$ (solid line) and the results obtained via computational experiments (squares), showing linear scaling relationship with the relative density $\bar{\rho}$. A single point obtained from the mean of the experimental measurements is also plotted along with the error bars at one standard deviation.

2. A majority of them are focused on fully dense parts, with the exception of very few that deal with porous components. The elastic response of the woodpile lattice along the filaments direction was previously studied for metal lattices in compression [36, 54, 55]. Here we present the experimental characterisation under tensile loadings of the apparent Young's modulus for lattices fabricated with FFF.

Machine description

The tensile tests on the complete lattice were carried out using an INSTRON 5569 machine. It consists of a base, two columns, a crosshead, and a top plate. This structure forms a rigid closed frame with high stiffness to reduce the deflection of the load frame during testing. Each column comprises a guide column and a ball screw. The crosshead is mounted on both the guide column and the ball screw. Rotation of the ball screw drives the crosshead up or down while the guide column provides stability. The machine performance parameters are listed in Table 4.2 [106].

TABLE 4.2: INSTRON 5569 performance parameters.

Load Capacity (kN)	50
Maximum speed (mm/min)	500
Minimum speed (mm/min)	0.005
Max. force at full speed (kN)	25
Max. speed at full force (mm/min)	250

Test results along the direction of the filaments

A set of 11 samples were tested. The dimensions of the samples tested were described in Chapter 3. All the samples for this case were fabricated lying on the printing platform, and having the filaments with axes aligned with the x- and y-axes of the 3D printer. The geometry and dimensions of the samples were given in figure 3.11. A photograph of a sample mounted on the INSTRON machine is shown in figure 4.10. Note the alignment of the filaments to the loading direction indicated with red arrows. The jaws are seen at the top and bottom of the photograph. INSTRON 5569 was operated in displacement control mode, the top grip moved upward at a strain rate of 5 mm/min applying a load in the vertical axis.

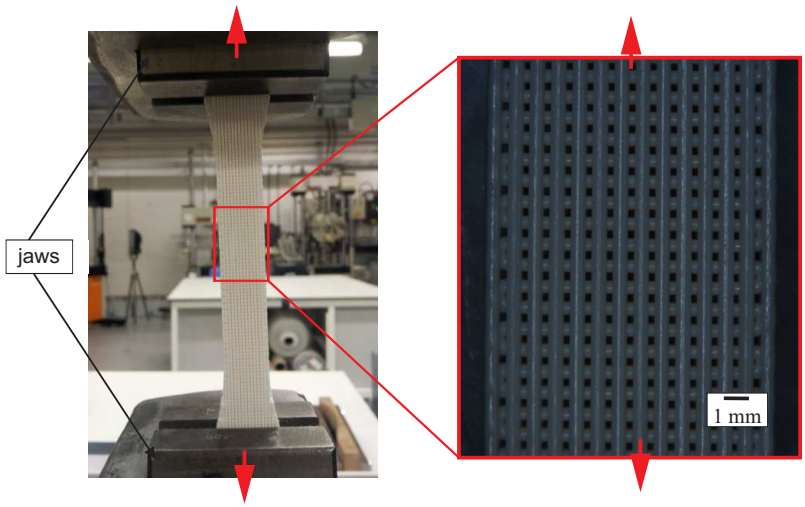

FIGURE 4.10: One of the samples during the tension test and the macrograph of the porosity showing the filaments aligned to the loading direction. The loading direction is indicated with the red arrows.

The force-elongation curves obtained were processed to stress-strain curves and are shown in figure 4.11. The apparent stress was calculated by dividing the force by the apparent cross-sectional area of the samples (assuming the sample to be homogeneous) $A = 98$ mm^2. The strain was obtained by dividing the elongation by the original length

TABLE 4.3: Experimental results for the apparent elastic modulus along the filaments direction $\langle E \rangle_{\parallel}$.

Sample	$\langle E \rangle_{\parallel}$ (MPa)	Yield Strength (MPa)	Elongation to break (%)
AL1	634.2	11.38	7.863
AL2	549.1	11.35	7.285
AL3	634.7	11.43	7.638
AL4	605.2	11.78	7.939
AL5	690.0	11.58	7.134
AL6	681.1	11.42	7.855
AL7	679.3	11.46	7.160
AL8	645.8	11.37	6.356
AL9	609.3	11.31	7.683
AL10	646.5	11.16	7.533
AL11	672.4	11.59	8.080
Mean	640.6	11.47	7.466
St. dv.	39.7	0.1568	0.479
Calculated $\langle E \rangle_{\parallel}$	692.0	-	-

between the grips $L = 100$ mm. The measured apparent Young's modulus was obtained from the slope of the linear part of the stress-strain curves as $\langle E \rangle_{\parallel}^{Measured} = 640.6 \pm 39.7$ MPa. The results are summarised in Table 4.3.

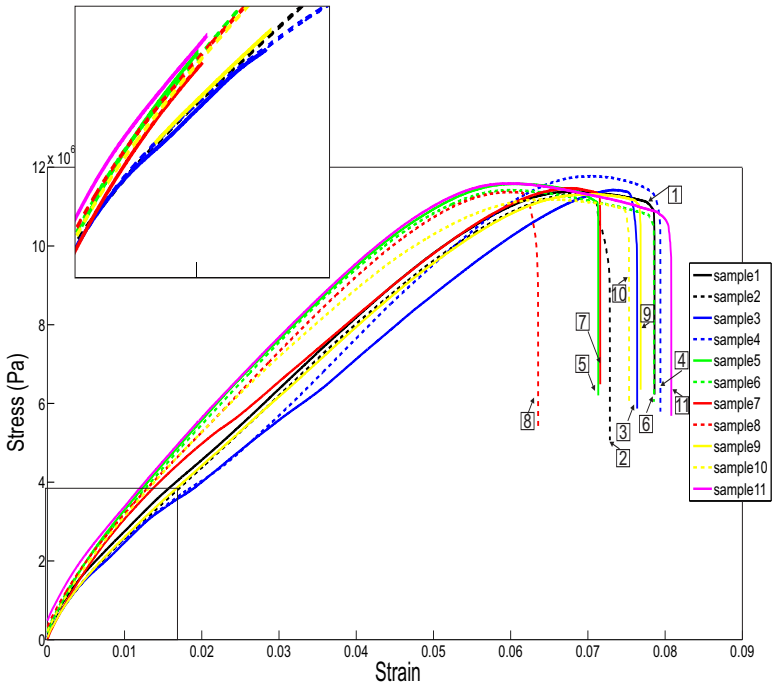

FIGURE 4.11: The stress-strain curves of the whole set of samples for the tensile test along the direction of the filaments. Inset shows a zoomed view of the initial response of the lattice material.

The value for the apparent Young's modulus was calculated using equation (4.2). The

fractional area was calculated as $\phi = Na/A$, where N is the total number of filaments parallel to the loading direction. Since we have full control on the G-code and, therefore, on the geometry of the produced lattice, we know the number of filaments are parallel to the loading direction, which is given by $N = 98$; 7 layers of 14 filaments each. The area of a single filament is taken as $a = 0.302$ mm^2 and the Young's modulus of the PLA obtained from the single filament characterisation $E = 2290$ MPa as determined in Section 4.1.3. The apparent Young's modulus was then calculated as $\langle E \rangle_{\parallel}^{Calculated} = 692$ MPa; this value is based on equation (4.2) in conuction with the single filament properties measured. A comparison of the predicted trend with experimental data is shown in figure 4.12. The predicted trend is shown in solid black line while the mean of the experimental data is presented with dots showing the distribution of one standard deviation.

Note a systematic difference between the calculated trend of 10%, which is always above the directly measured trend for complete lattices. Figure 4.12 indicates a slightly softer lattice than predicted using single filament properties. There are two possible reasons for this. Firstly the complete lattice shows sag of filaments overhung between orthogonally placed supporting filaments underneath. This slight curvature, also observed microscopically, as well as variability in the manufacturing conditions between those for a single filament and those for complete lattices.

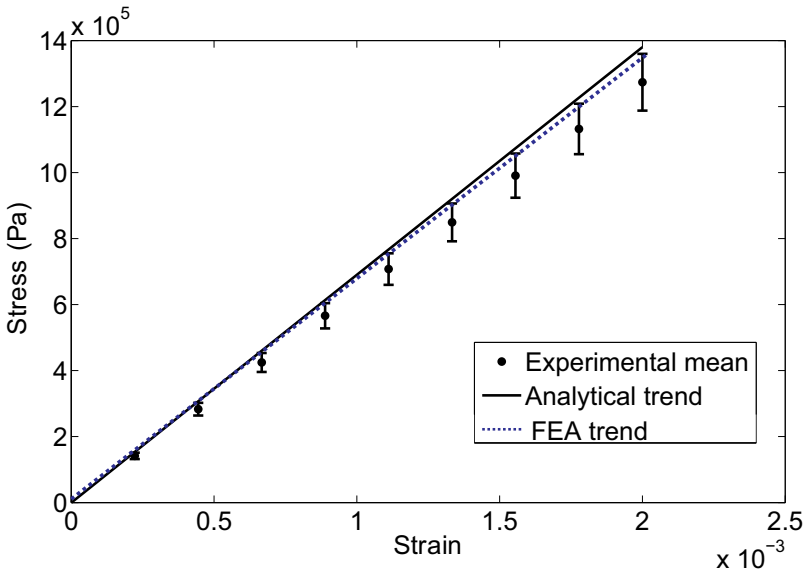

FIGURE 4.12: Stress-strain curves of the elastic part from the tensile tests and the predicted value using the rule of mixtures. The predicted trend is shown in solid black line. The mean of the experimental data is shown with dots. The error bars are shown at 1 standard deviation from the experimental mean.

4.3 Conclusions

The apparent Young's modulus of the woodpile lattice material along filament direction $\langle E \rangle_{\parallel}$ was measured and compared with a model that neglects deformation in filaments across the loading direction. The model utilises experimentally measured single filament properties. The comparison between the model and the FEA data showed excellent agreement for models with various relative densities. The experimental data and the calculated value showed minor differences attributed to manufacturing inconsistencies. The laboratory experiments were done on a set of FFF-manufactured samples.

The apparent Young's modulus $\langle E \rangle_{\parallel}$ was shown to be dominated by the filaments stiffness in tension or compression. The apparent Young's modulus was predicted by means of the rule of mixtures, as function of the cross-sectional area exposed to loading. The apparent property resulted to be stretch-dominated showing a linear dependence to the volume fraction $\langle E \rangle_{\parallel} \sim \bar{\rho}$. The woodpile lattice is a material arrangement that is directional dependent. The models and analysis presented in this chapter are restricted to the loading direction exposed. The mechanical response when loaded at any other direction will be significantly different. Currently, research is on these lines is underway.

Chapter 5

Flexural properties of 3D printed woodpile beams

Materials are most frequently used as beams or plates to resit external forces. Both structural forms have fundamentally similar mechanics–the main difference being the dimensionality. Beams are one-dimensional whereas plates are their two-dimensional generalisation. With increasing shift towards the use of 3D printed parts as functioning in service rather than as solid models, the behaviour of such additively manufactured parts is of great current scientific interest. This, combined with their use to resist bending is the main motivation of this chapter. In this chapter, the elastic response under transverse loading of woodpile beams is studied. Analytical expressions for the apparent bending stiffness and apparent shear of woodpile beams, as shown in figure 5.1, are developed here. A numerical characterisation of the role of shear in the transverse deflection of lattice beams is presented and compared with analytical models. Two different arrangements for the woodpile architecture are considered: the first with filaments aligned in the stacking direction, and that where they are staggered.

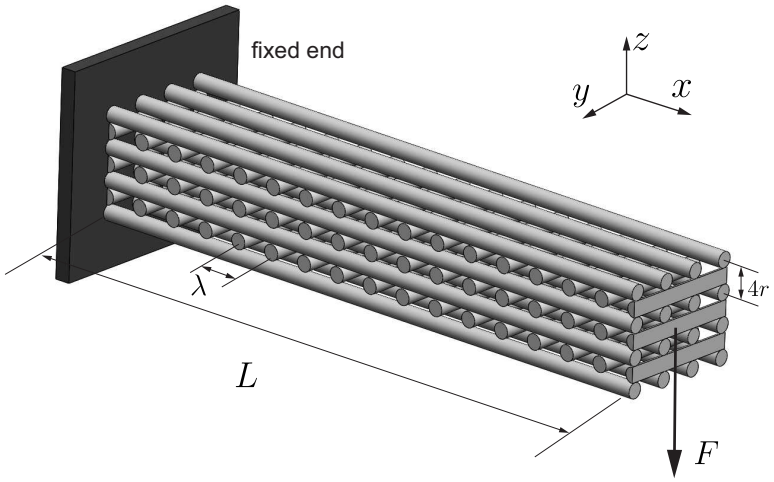

FIGURE 5.1: A cantilever beam made of the lattice material of one of the orientations studied. The thickness is given by the stack of layers.

5.1 Flexure of woodpile beams: apparent bending stiffness

Consider the flexure of a lattice beam subjected to a remote bending moment (M_∞) as shown in figure 5.2. Each filament induces a moment about the neutral axis (NA) of the lattice beam according to its distance from the NA. Therefore, the apparent bending stiffness $\langle B \rangle$ of the lattice beam can be expressed as $E\langle I \rangle$, where $\langle I \rangle$ is the effective second moment of area of the filaments distributed over the beam cross-section. This must be equal to the contribution to the second moment of area about the centroid of the cross-section of the structure according to the parallel axis theorem.

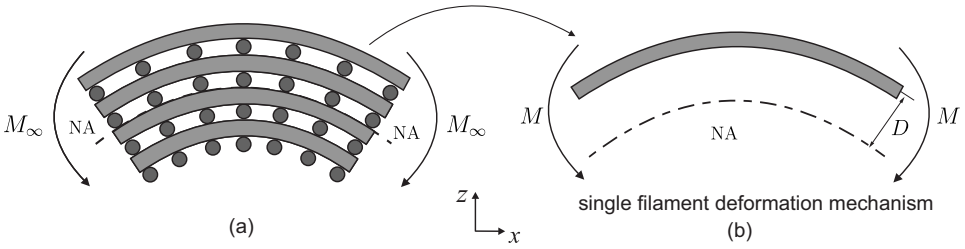

FIGURE 5.2: Schematic representation of (a) the lattice material subjected to remote bending moment M_∞, and (b) a single strut showing the deformation mechanism resulting from the bending moment, at a distance D with respect to the neutral axis (NA) of the lattice.

When lattice beams are bent in a plane as shown in figure 5.2, the displacement field in every stack of bent filaments, separated in the direction perpendicular to the plane of the paper, would appear to be identical. Also the filaments running perpendicular to the plane of the paper in figure 5.2, where they appear circular in their end views, would

participate in the elastic deformation minimally. This allows us to simplify consideration of the lattice geometry significantly. Modelling just one such group of curved filaments together with those providing spacing between them would be reasonable. Two views of such an abstraction are shown in figure 5.3, for odd number of stacks of filaments that participate in bending.

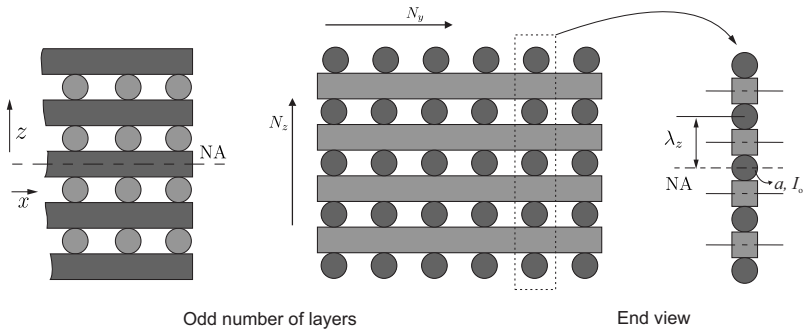

FIGURE 5.3: Schematic of the cross-sections of a lattice beam with odd number of layers.

Treating each filament as a beam, the apparent second moment of area, for an odd number of layers, is obtained by summing contributions from each, while accounting for the distance away from the neutral axis of the stack of filaments. Using the parallel axis theorem, we obtain an expression for the apparent second moment of the cross-sectional area as

$$\langle I \rangle = 2N_y \left[\sum_{i=1}^{(N_z-1)/2} \left(I_o + 16i^2 a r^2 \right) + \frac{I_o}{2} \right]. \tag{5.1}$$

Here N_z is the number of layers in the stacking direction, N_y is the number of such groups of filament in the y-direction (figure 5.3), $4r$ is the separation between layers because r is the filaments radius, I_o is the second moment of area of each filament about its own centroid. Note the upper limit of summation $(N_z - 1)/2$ which accounts for contribution on one side of the neutral axis; the factor 2 ensure the sum is carried out over the complete cross-section. The last term within the brackets is the contribution of the filament at the centre of the stack. An expression for even number of vertically stacked layers is obtained similarly as

$$\langle I \rangle = 2N_y \left[\sum_{i=0}^{(N_z-2)/2} \left(I_o + a \left(\frac{4r}{2} + 4ir \right)^2 \right) \right]. \tag{5.2}$$

Expressions in (5.1) and (5.2) both have the leading order terms that scale as $\sim \sum i^2$, The latter in (5.2) has a term that scales as $\sim \sum i$. The first of these can be summed up analytically using the square pyramidal number formula. The term $\sim \sum i$ in (5.2) is an arithmetic series that can also be summed up. Further, using the filament cross-sectional area $a \sim r^2$ in the expansion of these and reorganising terms, we obtain a single expression valid for both cases considered above as

$$\langle I \rangle = 8\pi r^4 N_y \left(\frac{1}{6} N_z^3 - \frac{13}{96} N_z \right). \tag{5.3}$$

Therefore $\langle I \rangle \sim r^4$ which is expected as this reflects stiffness due to flexure of the filaments. Further $\langle I \rangle \sim N_z^3$ holds when $N_z \gg 1$ so that the first term within the parenthesis dominates and we have an asymptotic formula for large N_z as $\langle I \rangle \approx (4/3)\pi r^4 N_y N_z^3$.

An expression for the apparent bending stiffness can now be derived in terms of the volume fraction in the form

$$\langle B \rangle = C \bar{B} \bar{\rho}^n \tag{5.4}$$

where $\bar{B}$ is a reference bending stiffness taken as

$$\bar{B} = \frac{E}{12} (N_y - 1) (N_z - 1)^3 \lambda (4r)^3 \tag{5.5}$$

which uses the second moment of the porosity-filled cross-sectional area, making $\bar{B}$ as the bending stiffness of a porosity filled dense beam. Using equation (5.3) and recognising that $\langle B \rangle = E \langle I \rangle$, we obtain

$$C = \frac{N_y \left(N_z^3/2 - 13 N_z/32 \right)}{(N_y - 1)(N_z - 1)^3} \quad \text{and} \quad n = 1. \tag{5.6}$$

The linear scaling with the volume fraction is in agreement with the linear scaling relation obtained in Chapter 4 for the apparent Young's modulus. The reason is because the axially running filaments are in tension and compression. The woodpile beam exhibits a stress distribution as shown qualitatively in figure 5.4, note the direction of the arrows point to the right for tensile stress on the top filaments and to the left for compressive stress for the bottom ones.

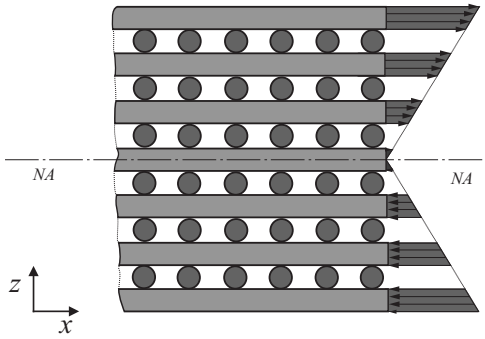

FIGURE 5.4: Stress distribution in the woodpile beam in flexure, showing the filaments above the NA in tension and the ones below the NA in compression.

5.2 The role of shear in transverse deflection of woodpile beams

When a slender solid beam is subjected to transverse loading, the transverse deflection scales according to $\delta \sim (L^3/EI)$, where L is the length of the beam and EI its bending stiffness. For relatively shorter beams, shear deformation needs to be accounted for [107, 108]. The relative importance of bending and shear in transverse deflection of solid beams depends on the ratio of the Young's modulus E and the shear modulus G, the shape of the cross-section and the slenderness. For solid material, $E/G = 2(1+\nu)$ is a fairly insensitive function of the Poisson's ratio ν because of the narrow range of the values for commonly found materials. Therefore, for dense beams the relative importance of bending over shear is primarily determined by the slenderness ratio. By contrast, for lattice beams, the ratio of bending and shear properties is extremely sensitive to the architecture of the lattice and the level of porosity.

The lattice considered here has three planes of symmetry which results in orthotropy of the material properties. However, here we restrict ourselves with lattice beams such that the bending axis aligns itself with one of the axes of orthotropy, hence such general considerations to fibre orientations are obviated.

Consider now a lattice under remote shear stress τ_∞, as sketched in figure 5.5(a). The bonding between struts is assumed to be at a point and it is assumed that the struts parallel to the y-axis do not contribute to the shear stiffness. The shear stiffness is a consequence of the bending of the struts parallel to the x-axis alone. Shear within the

cylindrical filaments, that appear circular on the xz-plane, is ignored; i.e. the circular shape is assumed to to be distorted during shear of the lattice. As opposed to this, shear in the filaments running parallel to the x-axis may be significant when the separation between the supporting filaments is short. Bonding between orthogonally oriented layers is assumed to be perfect. Therefore the shear of the woodpile is dominated by filament bending displacement w in the z-direction as shown in figure figure 5.5(b) for a repetitive unit and for a single filament between two consecutive points of bonding in figure 5.5(c). The dotted contour in figure 5.5(b) represents the underformed shape of the unit cell.

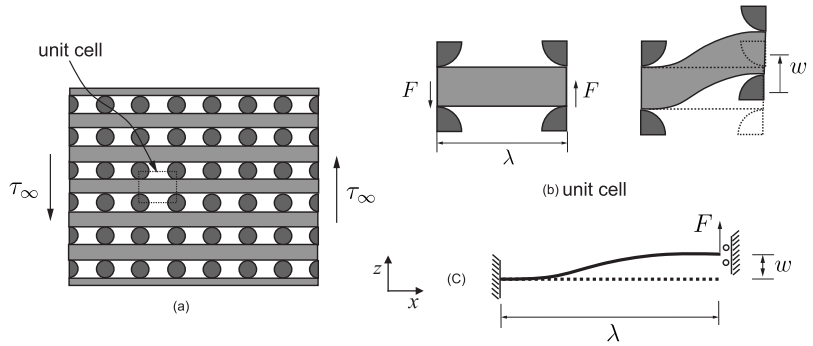

FIGURE 5.5: Schematics showing (a) the lattice subjected to shear stress τ_{xy}, (b) a unit cell deformation due to the shear stress, and (c) the representative strut used for the analysis.

The diameter to overhang ratio ($2r : \lambda$) is frequently found to be about 1:2 in additively manufactured lattices [33], and over 1:10 when using other manufacturing techniques [8, 55]. Therefore, thin beam theory may not be adequate to represent flexure of the filaments. Here we include shear within the filaments in addition to bending deformation, in order to develop a reasonably accurate, yet simple model of woodpile lattice shear. Such a model would cover a much wider range of relative densities, including situations where shear deformation is significant. Applying shear correction in the spirit of Timoshenko, an expression for the tip displacement w of a beam can be readily derived. The boundary conditions for beam mechanics used are: (i) at $x = 0$, deflection$= 0$, $\varphi = 0$ and (ii) at $x = \lambda$, deflection$= w$, $\varphi = 0$, where φ is the shear angle. The tip displacement as function of the applied force F is obtained as

$$w = F\left(\frac{\lambda^3}{12B} + \frac{\lambda}{2S}\right), \tag{5.7}$$

where $B = EI_o$ is the bending stiffness of the filament, and $S = \kappa Ga$ is the shear stiffness. Here, κ is the shear coefficient for circular cross-sections describing shear *within* a filament. The tip displacement w and the shear force F can be related to the apparent shear stress τ_{xz} and apparent shear strain γ_{xz} via

$$\tau_{xz} = \frac{F}{A} \qquad \text{and} \qquad \gamma_{xz} = \frac{w}{\lambda} \tag{5.8}$$

where $A = 4r\lambda$ is the porosity filled total area of the unit cell on which the shear force acts. Combining (5.7) and (5.8) and making use of the identity $\langle G \rangle_T = \tau_{xz}/\gamma_{xz}$, we obtain

$$\langle G \rangle_T = \frac{3BS}{6Br\lambda + Sr\lambda^3}. \tag{5.9}$$

The subscript T indicates the inclusion of Timoshenko shear correction in fibre bending. Recall B and S are the bending and shear stiffness of the filament material. Equation (5.9) is implicitly an expression for the apparent shear modulus as a function of the parent material properties (E and G), structural and geometrical parameters (λ, r). The dependence of the flexural displacement $w \sim (\lambda^3/r^4)$ makes the apparent shear modulus very sensitive to the parameter λ. Using $B = E(\pi r^4/4)$ and $S = \kappa G \pi r^2$, the expression for the apparent shear modulus is now obtained as,

$$\langle G \rangle_T = \frac{3\pi\kappa G E r^3}{6E\lambda r^2 + 4\kappa G \lambda^3}. \tag{5.10}$$

The apparent shear modulus can now be expressed in terms of the relative density of the porous material. After using the relationship $\bar{\rho} = \pi r/2\lambda$ (refer to Section 3.4.3), we have

$$\langle G \rangle_T = \frac{(6\kappa G E \bar{\rho}^3)}{(6E\bar{\rho}^2 + \kappa G \pi^2)}. \tag{5.11}$$

When Euler-Bernoulli model is used to describe the flexureal mechanics of filaments, we obtain an expression for the apparent shear modulus of the woodpile lattice as

$$\langle G \rangle_{EB} = \frac{6E}{\pi^2}\bar{\rho}^3, \tag{5.12}$$

after carrying out algebra on the lines of equation (5.7) through to (5.11) while ignoring

the second term in (5.7). The subscript EB denotes Euler-Bernoulli bending of filaments as the basis of the derivation of the apparent property. The connection between the two expressions in equations (5.11) and (5.12) becomes clear when we divide the numerator and the denominator in (5.11) by κG. In the limit of $\bar{\rho} \gg 1$, the two expressions coincide. This is expected as shear deformation theory represents the micromechanics better for relatively dense lattices, whereas it would provide negligible improvement over the apparent properties derived on the basis of Euler-Bernoulli micromechanics for material with thin filaments and large porosity. Rearranging terms, we obtain $\langle G \rangle_T = \langle G \rangle_{EB}/(1+\epsilon)$, where $\epsilon = 6E\bar{\rho}^2/(\kappa G \pi^2)$. Using $E/G = 2(1+\nu)$, we have $\epsilon = 12(1+\nu)\bar{\rho}^2/\kappa\pi^2$, where ν is the Poisson's ratio of the filament material. For example for the value of Poison's ratio $\nu = 0.36$ [101], and shear coefficient of $\kappa = 0.9$ for circular cross-sections [109], we obtain $\epsilon \approx 3.68\bar{\rho}^2$. Using Taylor series expansion the apparent shear modulus including shear correction can be expressed as,

$$\langle G \rangle_T \approx \langle G \rangle_{EB} (1 - 1.84\bar{\rho}^2) + \mathrm{O}(\bar{\rho}^4). \tag{5.13}$$

As an example, for $r/\lambda = 1/5$, $\bar{\rho} = \pi/10$, which gives $\langle G \rangle_T \approx 0.82\langle G \rangle_{EB}$, whereas for $r/\lambda = 1/10$, $\langle G \rangle_T \approx 0.95\langle G \rangle_{EB}$ highlighting the importance of inclusion of shear within fibres for dense lattices – the correction required is over 18% for relative density $\bar{\rho} < 0.3$. Also note the higher order term $\mathrm{O}(\bar{\rho}^4)$ which indicates a good approximation when we retain only the leading term $\mathrm{O}(\bar{\rho}^2)$ in the expansion – the next significant term being much smaller. Expressions (5.11) and (5.12) for the apparent shear modulus of woodpile structures are being reported for the first time.

5.2.1 Shear of lattices with staggered filaments

Consider the shear of a woodpile lattice with alternating layers in a staggered arrangement as shown in figure 5.6(a). For bending in the xz-plane, the stiffness is a manifestation of tension and compression in filaments running parallel to the x-axis. The expression for the apparent bending stiffness results the same as that derived in Section 5.1 when the alternating layers in the stacking direction possess an either 'eclipsed' or 'aligned' arrangement – the relevant expressions being given by equations (5.3) through

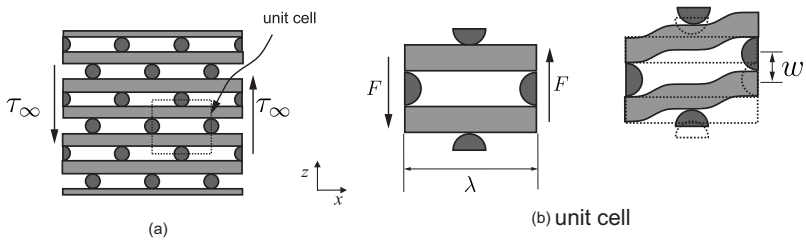

FIGURE 5.6: Schematics showing (a) the lattice subjected to shear stress τ_{xz}, and (b) a unit cell deformation due to the shear stress. The dotted contour indicates the undeformed unit cell.

(5.6). We can now carry out analysis for the staggered arrangement of struts on the lines of that from equations (5.7) through to (5.13). Comparing the deflections profile of the filaments in figures (5.5) and (5.6), we note that the deflected shape of $(\lambda/2)$ length in figure (5.6) resembles that of length λ in figure (5.5). The total vertical displacement w of the unit cell is given $\frac{w}{2} = \frac{(F/2)(\lambda/2)^3}{12B} + \frac{(F/2)(\lambda/2)}{2S}$ which is similar to the expression (5.7) except that half of the of the force over half of the overhang causes half of the total vertical displacement. After some algebra, the apparent shear modulus for the lattice in staggered arrangement is obtained as function of the relative density as,

$$\langle G\rangle'_T = \frac{24\kappa G E\bar{\rho}^3}{24E\bar{\rho}^2 + \kappa G\pi^2} \tag{5.14}$$

which is analogous to (5.11). The quantities with the prime symbol $'$ denotes properties referred to the staggered arrangement. For short overhang length λ, fibre shear is significant. The modulus using EB assumptions ignoring fibre shear is $\langle G\rangle'_{EB} = (24/\pi^2)E\bar{\rho}^3$ and, therefore, the following expression relating apparent shear moduli with and without fibre shear is obtained as

$$\langle G\rangle'_T \approx \langle G\rangle'_{EB}\,(1 - 7.36\bar{\rho}^2) + \mathrm{O}(\bar{\rho}^4). \tag{5.15}$$

The expression is analogous to equation (5.13) but they are for two differen stacking arrangements. Because of the change of the effective length at which the filaments are in flexure, the apparent shear modulus of the staggered lattice material having the same relative density as the aligned arrangement results 4 times stiffer (correction factors $1.84\bar{\rho}^2$ vs $7.36\bar{\rho}^2$). These two models were developed under the assumption that the amount of overlap between the struts is such that the rolling between them is excluded.

In the next section, response for lattice beams modelled using FEA are compared against the analysis presented in Sections 5.2 and the present section.

5.2.2 Numerical validation of fibre shear corrected lattice shear modulus

Analytical expressions for the apparent shear modulus obtained in Sections 5.2 and 5.2.1 are compared with numerical simulations using the finite element analysis (FEA) now. The apparent shear modulus obtained from unit cells of different relative densities are compared on a logarithmic scale in figure 5.7. The finite element model allowed lattice shear given purely by the transverse deflection of the struts, while constraining rolling of adjacent filaments. The scaling relation $\langle G \rangle \sim (\bar{\rho})^3$ is confirmed on a log-log plot by a slope very close to 3. This is consistent with the bending dominance in the filaments assumed here. An excellent agreement between FEA numerical experiments and the analytical models developed in the previous subsections can be observed for lattices with low relative densities ($\bar{\rho} < 0.3$). For relatively denser lattices, Timoshenko's correction in the micromechanics of the filaments improves the agreement significantly whereas the Euler-Bernoulli (EB) model is inadequate. Despite significant improvements by the introduction of filament shear for dense scaffolds, some differences between analytical prediction and the FEA simulations remain. They are attributed to two main factors. First, for denser lattices ($\bar{\rho} > 0.3$), the filaments can no longer be modelled as thin beams, as they are now in a complex state of stress. The inset in figure 5.7 shows a comparison between the errors obtained from the analytical models using Euler-Bernoulli theories of the staggered and aligned configurations. Errors for filament separation equal to $\lambda/2$ for the aligned arrangement are approximately the same when the separation is λ for the staggered arrangement. This is expected from the lattice shear patterns shown in figures 5.5 and 5.6, also confirmed numerically by the straight line at 45° passing through the origin (see inset in figure 5.7). Secondly, there is always finite overlap between two orthogonally adhering cylinders, rather than at a single point, to ensure bonding of filaments in the finite element mesh. A simple flexural theory does not account for this. How the overlap influences the shear response will be further discussed in Section 5.3.2.

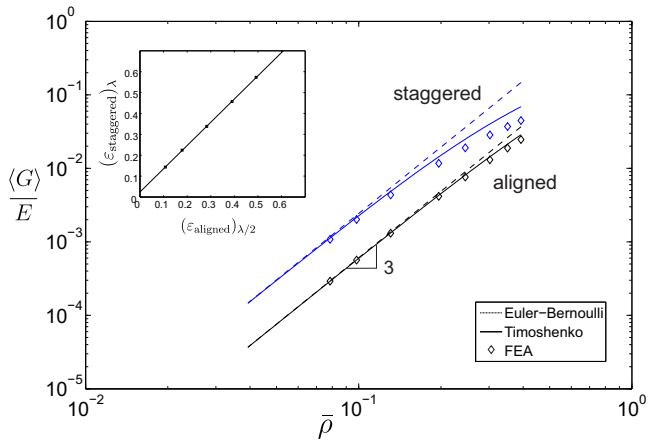

FIGURE 5.7: Apparent shear modulus $\langle G \rangle$ for both woodpile arrangements as function of the relative density $\bar{\rho}$ and a comparison with computational experiments using FEA. The dotted lines correspond to the prediction using EB assumptions, while the solid lines correspond to the filament shear inclusive model.

5.3 Bending and shear of woodpile beams

The effectiveness of the models developed on the basis of the micromechanics presented in the last section are now reconciled with numerically computed response of a woodpile lattice beam under transverse loading. A systematic parametric study by changing some key lattice parameters enables us to not only to corroborate the model, but also to provide a quantitative comparison of the relative importance of the different mechanism of lattice deformation. Additionally, factors unaccounted for in a simple analytical model are brought out. Relevant numerical calculations, results and discussions are organised in various subsections.

5.3.1 Transverse response of woodpile beams: mechanism of macroscopic and filament deformations

A lattice structure of simple macroscopic shape such as that of a beam of rectangular cross-section allows us to explore the mechanism of deformation by systematically changing selected macroscopic geometric parameters, since the behaviour of homogeneous continuum structures with respect to such changes is analytically known. For example, beams in flexure show a deflection–length dependence as $\delta \sim L^3$ whereas a shear beam shows $\delta \sim L$. This observation could be used effectively to determine the

relative importance of the two modes of deformation and their relationship with the microstucure of the woodpile. Further, any similarity or differences in the mechanical behaviour of a lattice beam with respect to that of a homogeneous continuum beam can be readily identified in this way.

A homogeneous cantilever beam of length L under tip loading F has tip deflection given by $\delta = FL^3/(3B)$. If a lattice beam were to behave as continuum, we could expect this relationship to be replaced by one making use of the apparent bending stiffness of the beam $\langle B \rangle$ in an analogous manner as $\delta = FL^3/(3\langle B \rangle)$ which shows $\delta \sim L^3$ scaling. Keeping all other lattice parameters the same, beam FEA models of different length were subjected to tip loading and the tip deflection was calculated. The structure in each case was discretised using tetrahedral elements as described earlier. The tip deflection plotted against the square of length of the lattice beam is presented in figure 5.8 for three different values of N_z, the number of layers in the stacking direction z. Each dot in this figure represents result for one structure. The straight line dependence validates $\delta \sim L^3$ relationship, with linear graphs of differing slopes–the difference being attributed to that differences in bending stiffness resulting from differing N_z.

As we have a model for the apparent bending stiffness $\langle B \rangle$ in Section 5.1, which makes use of the micromechanics of filaments when the lattice beam is bent, we use the theoretical value of $\langle B \rangle$ in the non-dimensional equation

$$\frac{\delta}{L} = \frac{FL^2}{3\langle B \rangle}. \tag{5.16}$$

Therefore, all the data presented in figure 5.8 must collapse to a line on the $\frac{\delta}{L}$ vs $\frac{FL^2}{3\langle B \rangle}$ plane. Data for a number of lattice beams, when the overall length, the number of layers and the spacing between filaments is changes, are presented on this plane in figures 5.9 and 5.10 where the values of $\langle B \rangle$ used are based on the formula developed in Section 5.1. These graphs shows that all the straight lines have a common slope of 1/3. However, the intercepts vary across these straight lines. The (1/3)-rd slope confirms beam bending behaviour, however the shift in the intercept for each of the beams indicates missing aspects of mechanics from equation (5.16). Moreover, this plot also hints that the missing mechanics must provide δ/L = constant dependence, i.e.

$\delta \sim L$ for the deflection unaccounted by equation (5.16). This is consistent with shear deformation. Thus the relationship that would collapse all data for any lattice geometry involving a range of filament diamters, material, filament spacing, number of layers, or overall length of the beam must be given by a beam deflection formula that accounts for the *apparent bending* and the *apparent shear* of the lattice beam. Note that the apparent bending of lattice beam is associated with filament *stretch* along the length of the beam, whereas the apparent shear of the lattice beam is associated with the filament *bending*. In solid beams, stretch and shear deformations are interdependent because they scale with the inverse of the Youngs's modulus and the shear modulus of the material respectively. For lattice beams, the apparent shear modulus depends on the Young's modulus and the architecture of the lattice in its leading order behaviour. The shear modulus of the filament material has only a secondary role via the shear correction of the the filament deflection.

The formula to calculate the tip deflection of a cantilevered beam loaded at the end accounting for shear is $\delta = F(L^3/3B + L/S)$. This expression can also be presented in the following non-dimensional form for a lattice beam with apparent properties $\langle B \rangle$ and $\langle S \rangle$ as

$$\frac{\delta}{L} = F\left(\frac{1}{3\langle B \rangle}L^2 + \frac{1}{\langle S \rangle}\right). \tag{5.17}$$

Comparing the above equation with equation (5.16), we note that an additional apparent property $\langle S \rangle = \kappa\langle G \rangle A$ is required. Results obtained for a large number of lattice beams having different number of layers, varied spacing and length all collapse to a single straight line when we make use of the value of the apparent shear modulus $\langle S \rangle$ incorporating expressions for $\langle G \rangle$, as developed in Section 5.2.

When cylinders are placed orthogonally with a single point of adhesion that connects them, the joint is free to rotate. This is unrealistic. Therefore, we reduced the distance between the axes along the direction of closest approach to less than the diameter, such that cylindrical surfaces dig into each other resulting in a patch of overlap (refer to figure 3.7(a)). The overlap used was $OL = 8\%$ in our simulations presented in this section.

Ignoring any apparent shear in the lattice, the overall bending of the woodpile beam

would obey the relationship in equation (5.16). This is clearly demonstrated by figure 5.9 when the length and the number of layers in the lattice beam are changed, keeping the porosity is fixed, i.e. the volume fraction $\bar{\rho} = 39\%$. The effect of changed number of layers on the transverse response is accounted for by the apparent bending stiffness $\langle B \rangle$. The dominant scaling behaviour for the apparent shear modulus is given by $\langle G \rangle \sim (r/\lambda)^3 \sim (\bar{\rho})^3$ because $(\bar{\rho}) \sim (r/\lambda)$ after retaining the leading order terms in equations (5.11) and (5.14) for the two woodpile configurations respectively. This has a dramatic effect on the transverse response upon changes the porosity $\bar{\rho}$, however. Figure 5.10 illustrates this–increasing the porosity (thus reducing the volume fraction as $\bar{\rho} = 23\%, 27\%, 39\%$) the tip defection increases rapidly. The tip deflection response shown in figure 5.10 differs by a huge factor of about 12 for short beams (left end of the plot) highlighting the significance of consideration to shear for porous lattices of the type being considered.

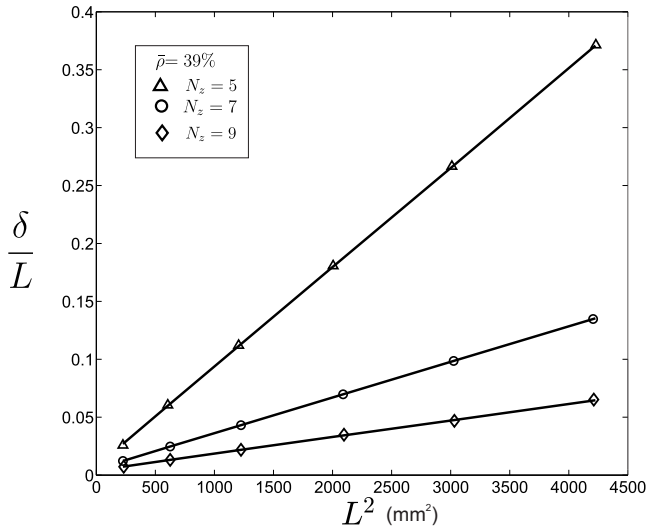

FIGURE 5.8: Plot (δ/L) vs L^2, the lines presented here correspond to different number of layers, $N_z = 5$, $N_z = 7$ and $N_z = 9$. These lines have different slopes and therefore different values of apparent bending stiffness $\langle B \rangle$.

The apparent shear flexibility is a consequence of flexure of the filament, as we noted in Section 5.2. The apparent shear stiffness is then given by $\langle S \rangle = \kappa \langle G \rangle A$, where $\kappa = 5/6$ for rectangular cross-sections [109] and where $\langle G \rangle$ is given by equations (5.11) and (5.14) for the two configurations of stacking. When we include shear flexibility due to filament flexure in the model, data from low porosity (as in figure 5.9 where shear is insignificant and an apparent-flexure-only model adequate) to relatively high porosity

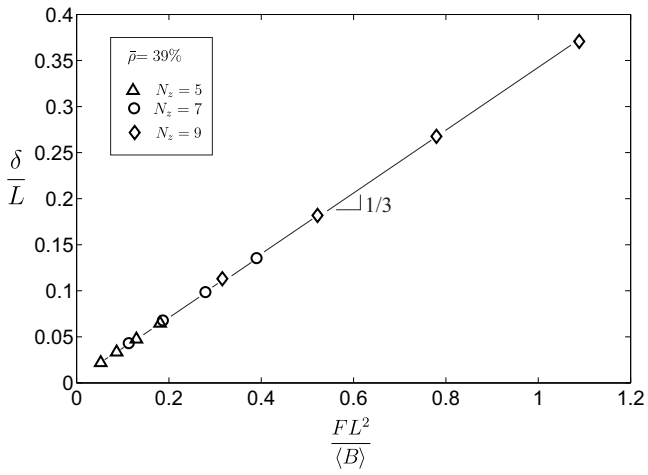

FIGURE 5.9: Plot (δ/L) vs $FL^2/\langle B \rangle$, for woodpile beams with the same porosity $\bar{\rho} = 39\%$. The lines presented here have the same slope of 1/3, showing negligible shear effect for low porosity woodpiles.

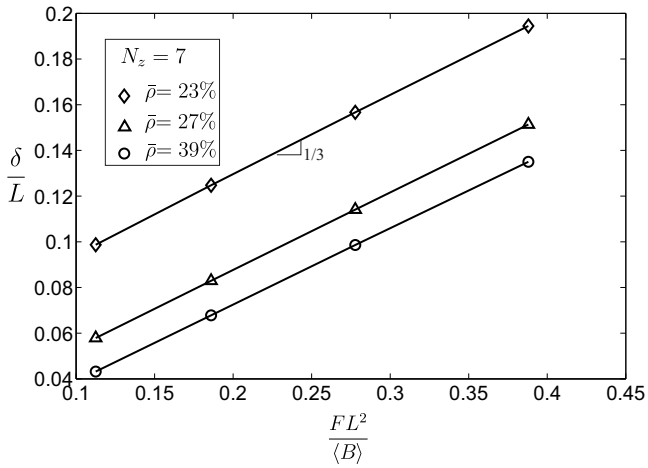

FIGURE 5.10: Plot of (δ/L) vs $FL^2/\langle B \rangle$, the lines presented here have the same slope of 1/3 and the difference of their intercepts is due to the shear influence in each case.

data from figure 5.10, collapse to a single line when the deflection associated with shear $\delta_{\text{shear}}/L = F/\langle S \rangle$ is subtracted. This line is shown in figure 5.11 where different markers in the figure correspond to tip response for different geometries when the aspect ratio of the overall beam and the porosity are changed. Note that the shear stiffness $\langle S \rangle$ used to plot these markers are obtained using the apparent shear modulus $\langle G \rangle$ from expressions (5.11).

We now compare the elastic response in the transverse deflection of the two woodpile beams in the plane shown in figure 5.12. The top beam is composed of the aligned arrangement while the bottom one is composed of the staggered structure. The deformed shapes of figure 5.12 were obtained from FEA simulations. These two examples are

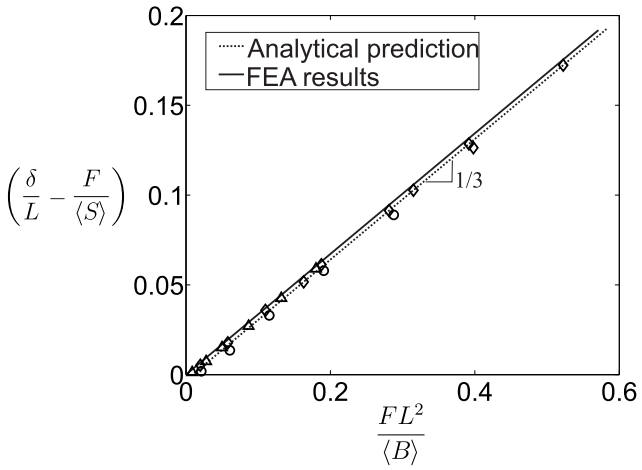

FIGURE 5.11: Plot of $(\delta/L - F/\langle S \rangle)$ vs $(FL^2/\langle B \rangle)$ showing the convergence of the data to a single line of slope 1/3. The data here was predicted using the analytical models presented in Section 5.1 and 5.2.

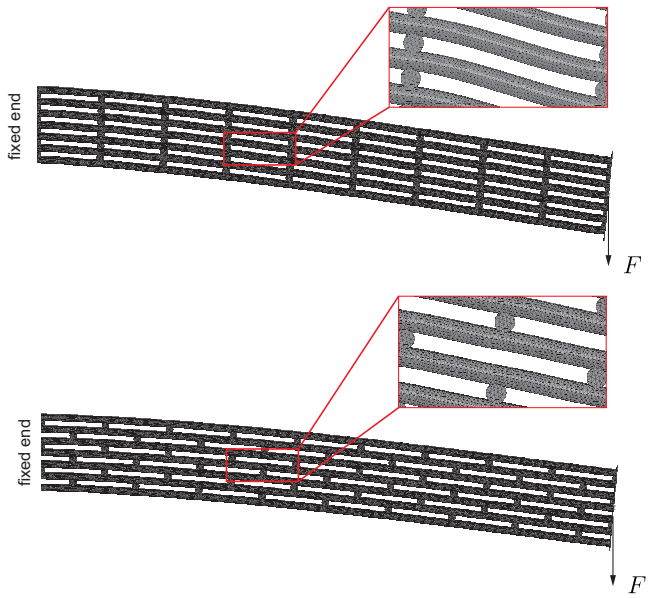

FIGURE 5.12: Deformed shapes from FEA simulations of cantilever beams composed of the two woodpile arrangements: woodpile aligned (top) and woodpile staggered (bottom). Both beams are composed of lattice materials with the same relative density and have the same number of axial filaments.

expected to have significant differences due to the role of shear in the transverse deflection in bending, as both beams have the same effective bending stiffness and relative density (the spacing between the struts λ is the same). The data for several beams with 7 layers, and various relative density ($\bar{\rho} = 23\%$, $\bar{\rho} = 27\%$ and $\bar{\rho} = 39\%$) are plotted in the $\frac{\delta}{L}$ vs $\frac{FL^2}{3\langle B \rangle}$ plane in figure 5.13. All lines appear parallel in figure 5.13. The role of shear is reflected in the different intercepts obtained, which are more obvious for beams with high porosity. For dense beams this effect is negligible. Note in figure 5.13 that for

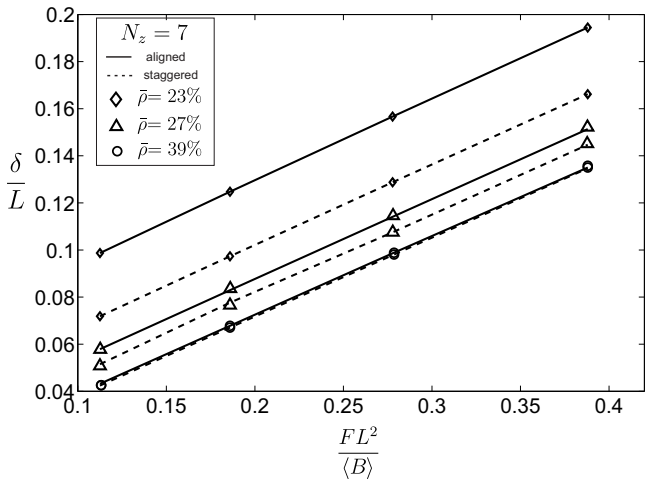

FIGURE 5.13: Comparison between the data obtain from FEA of beams with both aligned and staggered arrangements.

beams with the same relative density, the aligned configuration shows higher intercepts, which means that the apparent shear modulus is lower than the staggered configuration. The shear stiffness is found to be sensitive to the overlap of filaments at the region of adhesion. This is discussed next.

5.3.2 Sensitivity to overlap

Schematic diagrams in figures 5.5 and 5.6 highlight the kinematics of lattice deformation when a stack of filaments bonded at a single point are bent or sheared. In real manufacturing scenarios, this is not observed. A single point joint between two contacting cylindrical filaments offers no shear resistance even when the nodes belonging to different cylinders are tied up in translational degrees of freedom. This behaviour is very similar to a pile of elastic sheets (such as a stack of sheets of paper), which when bent slides over each other without much shear resistance. For woodpiles, adjacent layers "roll" over each other at "hinges" provided by tie points and the only elastic resistance is provided by deforming contacting surfaces, which requires careful implementation of this aspect of contact mechanics within commercial FE codes. Moreover, molten filaments in processes such as FFF inevitably show finite patch over which orthogonally placed filaments overlap.

The sensitivity of the overlap factor OL introduced here is sytematically studied computationally and is presented in figure 5.14. As the overlap increases, the apparent shear stiffness $\langle S \rangle$ increases and saturates to the theoretical value of $\kappa \langle G \rangle A$ where $\langle G \rangle$ is given by the formula developed in Section 5.2. The value of $\langle S \rangle$ is interpreted from the intercepts of lines in figure 5.10. The trend can be explained as the theoretical values are based on shear deformation that constrains rotation of the filaments rolling over each other. Thus theoretical values of $\kappa \langle G \rangle A$ provide upper limit to the shear stiffness, when the overlap factor is increased.

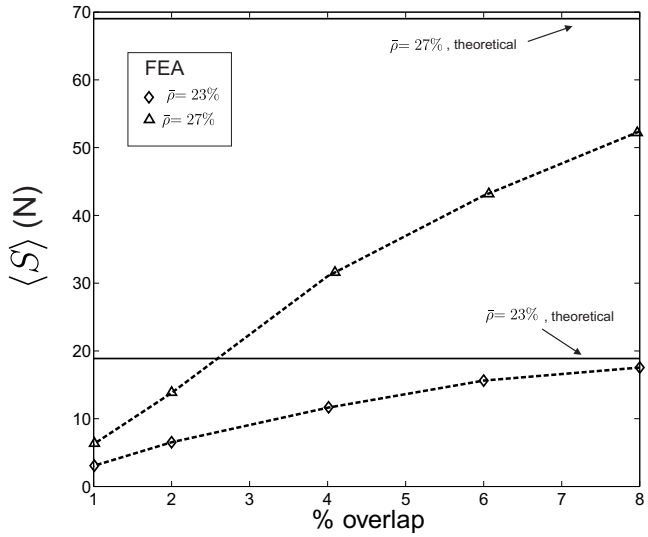

FIGURE 5.14: Convergence of the value for the $\langle S \rangle$ as the OL% is incremented.

5.4 Bending in the plane of filament adhesion

Consider now the orientation of the woodpile beams as shown in figure 5.15(a). Bending is considered in the plane of the paper; the z-axis points out of the paper (5.15(b)). The difference is further highlighted by the side view of the beam in figure 5.15. Note that bending in this plane is associated with flexure of *all* the filaments as opposed to the previous cases when alternate filaments were practically stress-free. The role of architecture is brought out numerically. Solid models of three cantilever beams are shown in figure 5.16. They are made of cylindrical filaments of radius $r = 0.25$ mm. The FEA models were meshed using linear tetrahedral elements C3D10. The external dimensions of the apparent cross-sectional area are the same for the three cases presented in figure

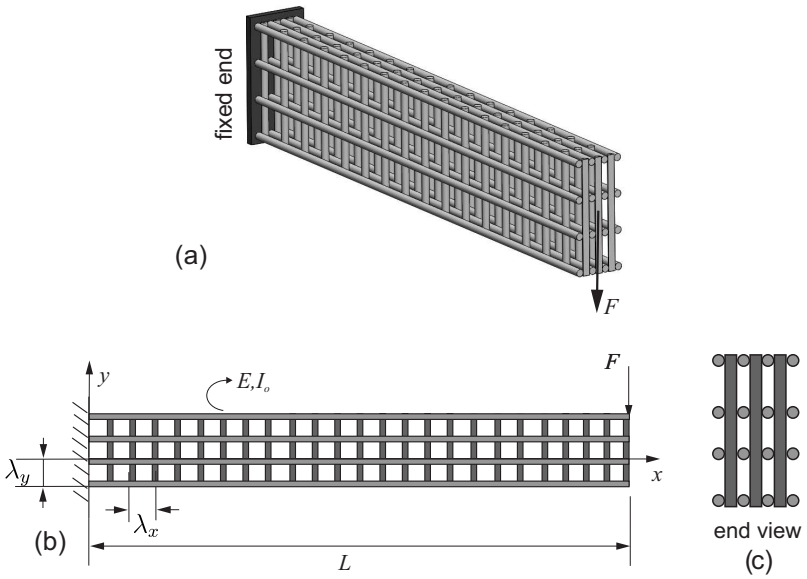

FIGURE 5.15: (a) A cantilever beam made of the woodpile lattice material, note the different orientation with respect to the case studied in Section 5.1. (b) The side view of the beam that bends in the plane of the paper. (c) The end view of the lattice beam.

5.16. From figure 5.16(a) the top beam is made of a square lattice having $\lambda_x = \lambda_y = 2.5$ mm. The middle beam of figure 5.16(b) has the following overhangs $\lambda_x = 1.25$ mm and $\lambda_y = 2.5$ mm, while the bottom one (figure 5.16(c)) has $\lambda_x = 2.5$ mm and $\lambda_y = 1.25$ mm. Note that the middle and bottom beams are composed of the same lattice, resulting in the same volume fraction $\bar{\rho}$, but rotated at 90°.

The first two beams (figures 5.16(a) and 5.16(b)) have the same number of filaments parallel to the x-axis, while the overhang has been reduced by a factor of 1/2, from 2.5 mm to 1.25 mm doubling the number of vertical filaments. Because these two have the same number of axial filaments, it is expected that they will result with the same apparent bending stiffness. While the apparent shear is expected to be significantly different, as the top beam has a greater overhang, making it softer in shear.

Now compare the middle and bottom beams (figures 5.16(b) and 5.16(c)). While the bottom beam has 7 number of axially running filaments, as opposed to 4 in the middle beam, the apparent bending stiffness of the latter is expected to be higher. Both configurations are expected to have the same shear influence in the transverse deflection.

As in Section 5.3.1, keeping all other lattice parameters the same, beams of different length were subjected to tip loading and the tip deflection was calculated by using FEA.

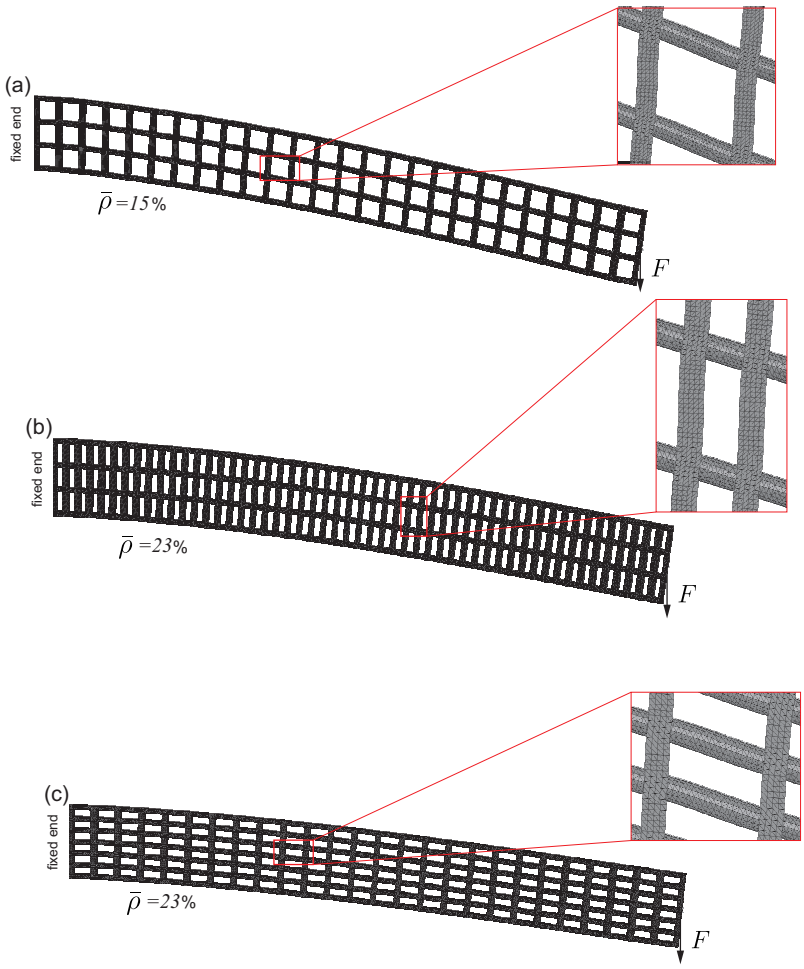

FIGURE 5.16: Deformed shapes from FEA simulations of cantilever beams composed of the three lattice arrangements. (a) $\lambda_x = \lambda_y = 2.5$ mm, (b) $\lambda_x = 1.25$ mm and $\lambda_y = 2.5$ mm and (c) $\lambda_x = 2.5$ mm and $\lambda_y = 1.25$ mm.

The tip deflection plotted against the square of the lattice beam length is presented in figure 5.17. As expected the top and middle beams (figures 5.16(a) and 5.16(b)) resulted with the same apparent bending stiffness, indicated by parallel lines in the δ/L-L^2 plane. Recall that the apparent bending stiffness is obtained from the slope of these lines. The different intercepts from the data of the top and middle configurations, confirm that the shear effects are different. Whereas, the data for the middle and bottom beams (figures 5.16(b) and 5.16(c)) result in lines with the same intercept, and therefore same shear stiffnesses.

The results presented here bring out the interesting possibility of the independent control on the apparent bending and shear influences in the transverse deflections of lattice beams. The reason is the apparent bending stiffness given by the axial filaments, while

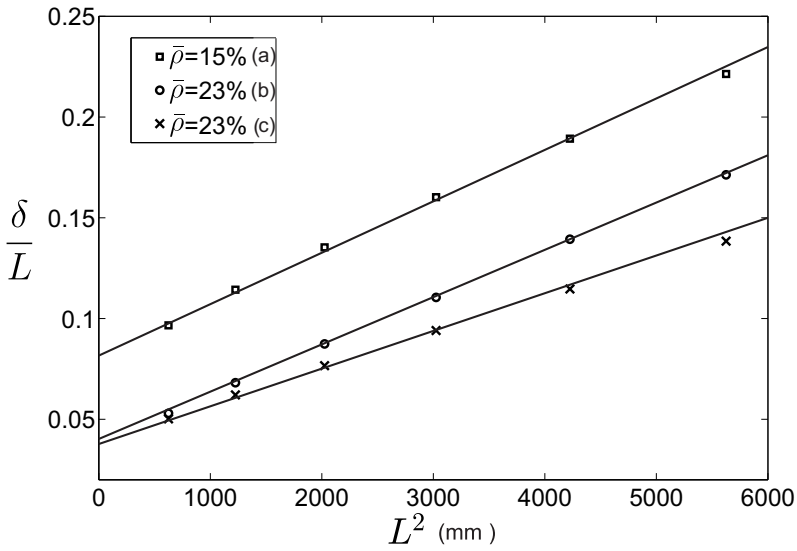

FIGURE 5.17: Plot L^2 vs δ/L for the three beams configurations described earlier. (a) (b) and (c) correspond to the figure 5.16. As expected (a) and (b) having with the same number of filaments parallel to the x-axis have the same slope, while the (b) and (c) with the same relative density ($\bar{\rho} = 23\%$) have the same intercept.

the shear influence is dependent on the overhang between filaments. Both behaviours can be customised by rearranging the filaments with the beam. This type of analysis are enhanced with the use of additive manufacturing, where a controlled placement of filaments is easily achieved. In the following section, we present experimental results on FFF-samples in three-point bending.

5.5 Experimental results and reconciliation with theory

Results obtained from the model presented in this chapter for the apparent bending stiffness were compared with experimental measurements from three-point bending tests. A schematic diagram of the test showing the orientation of the lattice analysed with respect to the loading direction is shown in figure 5.18. The description of the test procedure and the data measured are presented next.

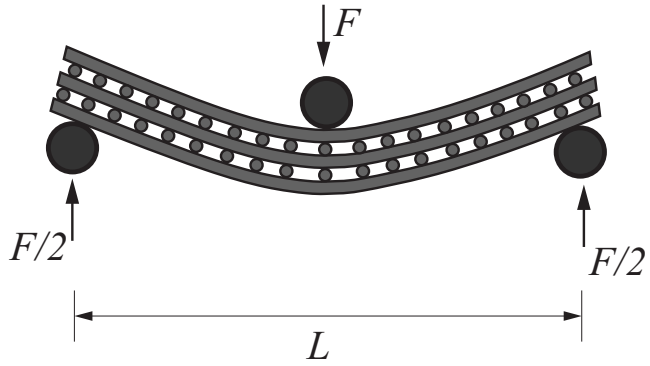

FIGURE 5.18: Schematic of the three-point bending test showing the orientation of the woodpile with respect to the loading direction.

5.5.1 Three-point bending tests

Currently, there are no standards for the testing of FFF produced samples. The tests presented here were performed according to the ASTM D790 standard for flexural properties of polymers. Rollers with diameters of 8 mm and a distance L between supports was kept to be of 88 mm. The machine was set in the "displacement control" mode and the force applied was measured. Figure 5.19 shows the evolution of the deformation of one sample during the tests. Each stage of the test is labelled and can be related to figure 5.20 where the resulting load-deflection curves are presented. Three different displacement controls were set for the first three samples with maximum transverse displacements as follows: (i) for *sample1* 20 mm, (ii) for *sample2* 30 mm and (iii) for *sample3* 15 mm. A displacement of 20 mm is adequate to complete the force-defletion curve up to the point of failure as see in figure 5.20. Therefore, all the samples were tested with the machine having a maximum displacement of 20 mm.

5.5.2 Measured flexural response and validation of analytical models

The measured load-deflection curves are presented in figure 5.20. The numbered labels relate the stage of deformation corresponding to those in figure 5.19. Stage 1 is the initial phase of the test, when both load and deflection are infinitesimally small. A number of the samples suffered an initial slip when the load was first applied. This slip results in the initial part of the load-deflection curve showing deflection with almost no increment in the load. Stage 2 is the end of the linear elastic part, beyond which, the samples

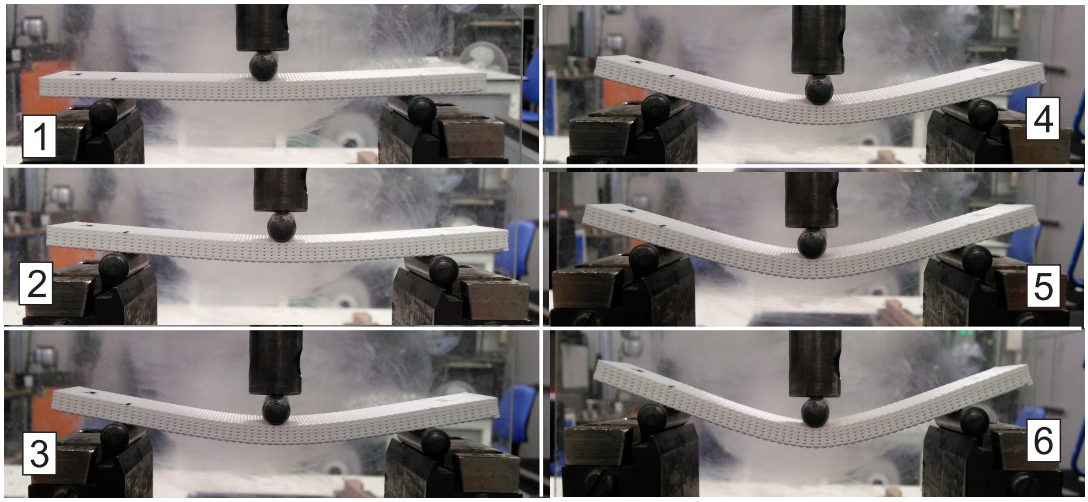

FIGURE 5.19: Three-Point bending test showing the evolution of the sample deflection during the experiment.

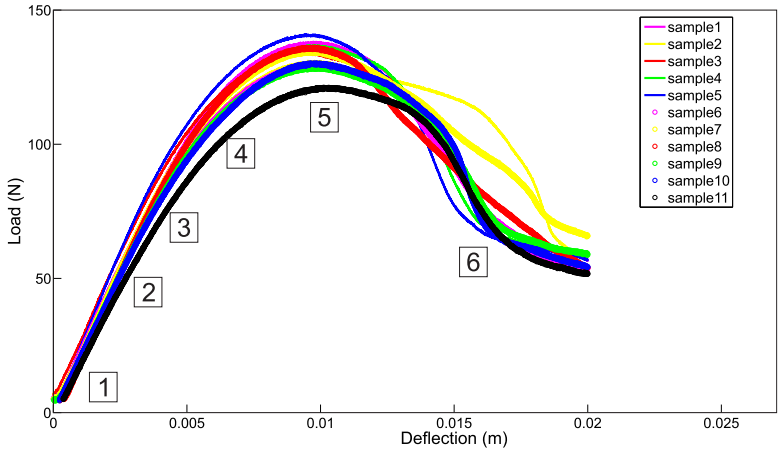

FIGURE 5.20: The resulting Force-elongation curves of the whole set of samples in three-point bending.

move to plastic deformation and the curve becomes non-linear. Stages 3 and 4 are at a displacement of 5.5 and 6.5 mm respectively, where the material has undergo significant plastic deformation. Stage 5 corresponds to a transverse displacement of 8 mm where the maximum load applied to the material is $\approx$ 130 N. During Stages 3-5, the filaments of the bottom layer are under tensile stress, experiencing necking and fracture. Finally, stage 6 is when the material has completely failed, offering no resistance to deform. This can be seen in figure 5.20 by a reduction in the load applied and the continuous increment in the deflection. The comparison between the experimental results and those based on a mechanical model is presented next.

The linear elastic part of the force-deflection curves measured (labels 1-3 in figure 5.20) during the three-point bending tests was then compared with the prediction using the expression described in Section 5.1 . We can now employ equation (5.2) in the formula for the deflection δ of a beam in three-point bending, $\delta = FL^3/48\langle B\rangle$; the material $E = 2290$ MPa, and L is the total length between the supports, in this case $L = 88$ mm. The samples tested had $N_z = 6$ and $N_x = 26$. Here we consider one layer to be composed of two layers of orthogonally stacked filaments. The area of a filament is $a = 0.302$ mm^2. The effective second moment of area was calculated using equation (5.2) as $\langle I\rangle = 138$ mm^4. The predictions and the experimental measurements area compared in figure 5.21. They validate the assumptions stated for woodpile beams, as the prediction is in excellent agreement with the experimental data. The filaments in the other direction do not contribute significantly to the bending stiffness, but they do in the shear deformations. For the samples studied here, shear is unimportant as confirmed by the excellent agreement with experiments. Note that ignoring flexibility due to shear has led to slightly stiffer load-displacement curve in the prediction.

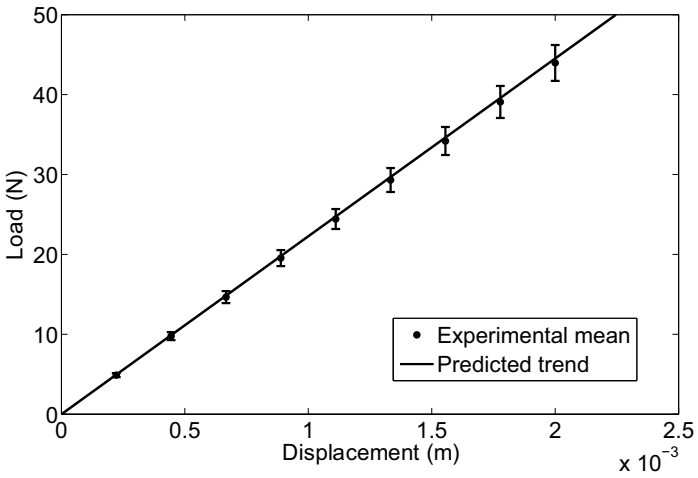

FIGURE 5.21: Linear elastic part of the load-displacement curves from the three-point Bending tests, the mean of these data and the predicted trend calculated using the one-dimensional model derived. The predicted trend shows good agreement with the experimental data.

5.6 Conclusions

In this chapter, the flexural properties of woodpile beams were studied. The role of shear in the transverse deflection was highlighted. Analytical expressions for the apparent elasticity of structures with woodpile architecture were developed when slender lattice structures experience apparent bending and shear. When a slender beam made up of a woodpile of filaments is bent, the filaments running parallel to the axis of the beam experience stretch whereas when the beam is sheared, the filaments experience bending. This fundamental micromechanics of the filaments allows us to derive analytical expressions for finite number of stacks the woodpile and also the dependence of bending and shear stiffness in terms of the relative density of the porous structure. The analytical results for bending stiffness presented for the first time are also expressed in terms of an asymptotic formula for large number of layers. The expressions thus derived indicate that the bending stiffness scales with the relative density as $\sim \bar{\rho}$ whereas the shear stiffness scales as $\sim \bar{\rho}^3$ which is consistent with the primary mechanisms of filament deformation identified for these two respective cases of transverse deflection of the structure. The first of these is also consistent with the apparent Young's modulus scaling $\langle E \rangle \sim \rho$. For the flexure of a woodpile stack with infinite number of layers one can make use of the apparent Young's modulus $\langle E \rangle \sim \rho$ to estimate the apparent bending stiffness. The analytical expression presented here is more accurate for a finite number of layers than the asymptotic formula, as it accounts for their exact number.

For relatively dense lattices, and for long beams, a filament stretch based apparent-bending-only-model which ignores shear of the lattice provides satisfactory agreement with numerical results. However, when the lattice is relatively porous and the beam relatively short, ignoring lattice shear leads to huge errors–up to 1200% for the worst cases considered. Such large influence of shear is a reflection of the lattice microscructure: dense elastic continuum beams require much smaller shear correction than porous beams rending the problem of lattice beams one where shear is not a mere correction but an essential part of the model. The relative significance increasing appreciably with porosity. An excellent quantitative agreement between shear-inclusive bending theory developed here and numerical computation for a large range or porosity and shortness of the beam

is reached–this is demonstrated by identifying a shear adjusted non-dimensional group which collapses all data aligned to a theoretically predicted trend.

Expressions for apparent bending stiffness $\langle B \rangle$ and the apparent shear stiffness $\langle S \rangle$ are derived for two configurations of the woodpile–first when the alternating layers eclipes each other and the latter when they are staggered. The bending stiffness is independent of the configuration whereas the shear stiffness shows a strong differences: for the same porosity, the staggered arrangement is approximately four times as stiff in shear. Finally, the role of the so-called overlap factor is brought out which indicates that the stiffness has an upper bound given by the analytical expressions, which constrain rotation of cylinder over each other. In summary, we provide benchmark results for the transverse response of slender lattice beams, which shows excellent agreement with a shear inclusive model which uses apparent bending and shear stiffnesses.

Finally, three-point bending laboratory experiments on FFF-woodpile beams were carried out. The elastic response of the force-deflection curve was compared to analytical predictions showing excellent agreement.

Chapter 6

Torsional properties of 3D printed woodpile bars

Structures and porous scaffolds manufactured using additive manufacturing could experience complex loading situations. Slender 3D printed lattice bars having woodpile architecture were considered in the previous chapters under tensile and bending loading. In both cases, the primary mechanism of deformation in the filaments is stretch. When bending is accompanied with lattice shear, flexure of filaments contribute additionally. In this chapter, the third most commonly encountered loading scenario is considered– when the lattice structure is subjected to torsion.

6.1 Apparent torsional stiffness of a group of filaments

The apparent torsional stiffness of a group of filaments that run parallel to the twist axis is considered here. An approach based on the polar second moment of the cross-sectional area of the filaments is presented first. The weakness of this approach is brought out. This further leads to the subsequent sections, where is identified that the primary micromechanics of filament deformation originates from lattice shear, which is associated with filament bending.

6.1.1 Torsion of a group of parallel running filaments

Consider the torsion of a group of filaments that run parallel to the twist axis. A similar situation was encountered for the bending of a group of filaments running parallel to the axis of the beam in Chapter 5. When a group filaments is bent, the filaments continue to be in tension or compression–dominant direction of struts being associated with the axis of the beam. This enables us to express the apparent bending stiffness of a group of filaments via the second moment of the area of the filaments about its centroid. However, a similar approach to torsion, i.e. by making use of the apparent second polar moment of area of the filaments is bound to be unsuccessful. The reason for this lies in the patterns of shear flow, which is discussed next.

Slender prismatic solids of the same total area and the same polar second moment of area show huge differences in their torsional stiffness, depending on the topology of the material connectivity on the cross-section. This is highlighted by considering torsion of a complete thin tube of radius R and thickness t (see figure 6.1(b)). Its torsional stiffness is given by $J_{complete} = 2\pi R^3 t$. Compare this with the same tube cut using a thin slit (see figure 6.1(c)) that possesses a torsional constant $J_{cut} = 2\pi R t^3/3$, even though the two sections have approximately the same area and the same polar second moment of area. The ratio of the values of torsional stiffness is given by $J_{complete}/J_{cut} = 3R^2/t^2$ which, for $R/t \gg 1$, is very large.

We are now in a position to extend the argument of a complete tube versus a cut tube to highlight the difference in stiffness between an expression using an effective polar moment of inertia $\langle J \rangle$ derived based on the parallel axis theorem, which overestimates rigidity and the realistic assessment based on the correct shear flow considerations. Consider figures 6.1(d),(e) and (f) progressively. The topology of the tubes is further changed and the shear flow is qualitatively shown for each material domain within the cross-section. Figure 6.1(f) can be viewed as a 'tube' cut in several places so that each short piece gradually becomes a filament. The shear flow is 'broken' at each gap within the cross-section (just as it is broken once by the cut in figure 6.1(c)). The shear flow pattern highlights that the moment of the shear distribution about the centre of a group of fibres is much smaller in a 'cut-topology' as in figures 6.1(c) through to 6.1(f), because

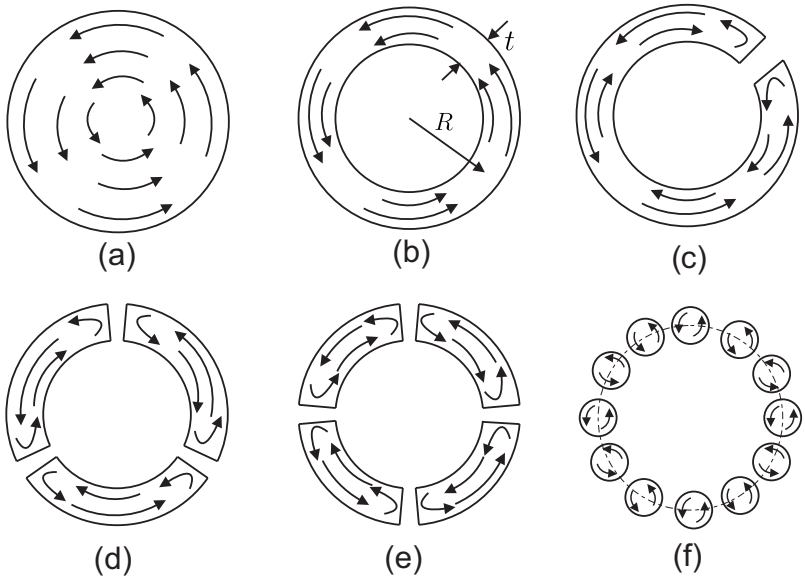

FIGURE 6.1: Comparison of the shear flow due to torsion of several cross-sections. (a) solid circular shaft, (b) closed section circular shaft, commonly known as tube, (c) tube with a zero thickness cut resulting in an open cross section, (d) and (e) have cross-sections with zero thickness cuts at 120° and 90° respectively, and, finally, (f) tube made of circular cross-section filaments. The application of torque will produce an uninterrupted circuit of shear flow in Cross-sections (a) and (b), while (c), (d), (e) and (f) result with a shear flow that does not flow around the cell but within it.

along a radially drawn line from the centre of a filament group, the sign of shear stress switches from the inner-most points to the outer-most points. This is further illustrated in figure 6.2 for the cross-section of a single filament.

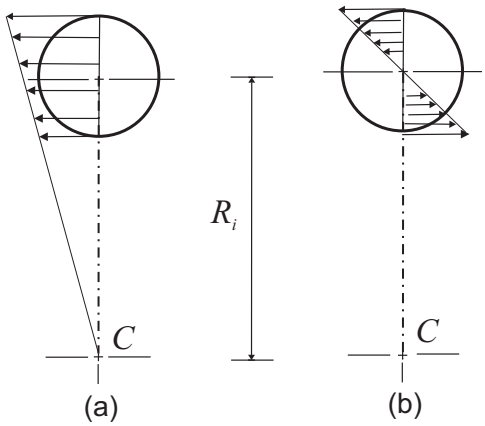

FIGURE 6.2: Shear distribution in a filament twisting about a centre C: (a) The torsion kinematics is assumed to be such that all the fibres rotate rigidly about a centre of rotation C giving rise to an overestimated torque. (b) Shear flow in disconnected fibres twisting about a centre. This comparison of the shear flow highlights the difference of the resulting torques. The net moment in (a) results higher due to the moment arm from the twist axis.

The quantitative difference between the stiffness incorrectly predicted by the kinematics

of the cross-section of the filament bundle twisting as a rigid plane about the centre of twist of the bundle and that predicted by the correct shear flow considerations is huge. The torsional stiffness of a filament bundle is given by $J \sim N2a\overline{\phi}_0^2$ where $\overline{\phi}_0$ is the radius of gyration of area of a circular section of a single filament about its own axis. Compare this with the (incorrect) expression based on parallel axis theorem, which is $Na\overline{\phi}_0^2 + a\overline{\phi}^2$ where $\overline{\phi}^2$ is the radius of gyration of the *filament group*. Clearly, $\overline{\phi} \gg \overline{\phi}_0$, which makes a big difference. The twist of fibres running parallel to the twist axis in a woodpile lattice, behave exactly like a filament bundle discussed here, hence the same is true of the torsional stiffness of a lattice material. Based on the conclusions expressed in this section, we derive an expression for the apparent torsional stiffness of a free bundle of filaments in the next section.

6.1.2 Apparent torsional stiffness of a bundle of filaments

We present the analysis of the torsional properties of woodpile bars, by studying the apparent torsional stiffness of a group of parallel filaments as shown in figure 6.3(a). The ith filament is isolated from the group and shown in figure 6.3(a). The deformation mechanism of the filaments is composed of twist with respect to their own centroid accompanied by the inevitable bending caused by the geometry because the group of filaments are to be kept separated and a distance $\mathbf{R}_i$ from the twist axis. If we consider the filaments as an interconnected group of slender bodies, the shear flow due to the twist response will be 'broken' at each gap within the cross-section of the filament group (as discussed in the previous section). So in a bundle of filaments the strain energy of the ith filament under these loading conditions is given by the contribution of both the twist and flexure. The total strain energy for the ith filament in the bundle is given by a sum of strain energy due to filament twist and filament bending, i.e.

$$U_i = U_{ti} + U_{bi}, \tag{6.1}$$

where U_{ti} and U_{bi} are the strain energies due to torsion and bending respectively. While all the filaments twist by the same amount, the bending contribution depends on its

distance from the twist axis. The strain energy due to the twist of the ith filament is given by $U_{ti} = (1/2)GJ_o\theta^2/L$, where J_o is the torsional constant, L is the length of the filament, and θ is the twist angle. The strain energy due to bending is given by $U_{bi} = (1/2)B\int_L(\kappa''^2)\mathrm{d}x$, where κ is the curvature of the deformed filament. We proceed to parametrise the expression describing the deformed shape due to bending. Take the filament extracted from the twisted bundle of filaments in figure 6.3(a). The relative position of the centroid of the filament cross-sectional area with respect to the twist axis is defined by the vector $\mathbf{R}_i$. The vector is defined in the yz-plane as $\mathbf{R}_i = [y_i, z_i]$. From figure 6.3(b), we know that the location of the ith filament is $y_i = |\mathbf{R}_i|\cos\beta$ and $z_i = |\mathbf{R}_i|\sin\beta$. If we assume small angle displacements θ, the tip displacement δ_t is given by $\delta_t = \mathbf{R}_i\theta$.

Taking one end of the bundle as fully fixed and the cross-section at the loaded end is constrained to remain in the plane, the filaments will bend with the boundary condition as slope = 0 at both ends. For a beam with these boundary conditions, a pre-inscribed tip displacement equal to δ_t, the displacement at any point along the length is given by

$$\delta(x) = \left(\frac{3\delta_t(L)}{L^2}\right)x^2 - \left(\frac{2\delta_t(L)}{L^3}\right)x^3. \tag{6.2}$$

If we take the tip displacement $\delta_i(L) = \delta_{it}$ of the ith filament to be composed of the displacements in the y- and z-axes as $\delta_i = [v_i, w_i]$. Then, taking the displacements at the loaded end as $v_i = -z_i\theta$ and $w_i = y_i\theta$, and substituting them in equation (6.2), the displacement components at any point along the length are given by,

$$v_i(x) = \left(\frac{-2z_i\theta}{L^3}\right)x^3 + \left(\frac{3z_i\theta}{L^2}\right)x^2 \tag{6.3a}$$

$$w_i(x) = \left(\frac{2y_i\theta}{L^3}\right)x^3 - \left(\frac{3y_i\theta}{L^2}\right)x^2. \tag{6.3b}$$

The curvature is equal to the second derivative of the displacement $\kappa = \mathrm{d}^2w/\mathrm{d}x^2$. Therefore, differentiating twice with respect to x and considering the displacements to

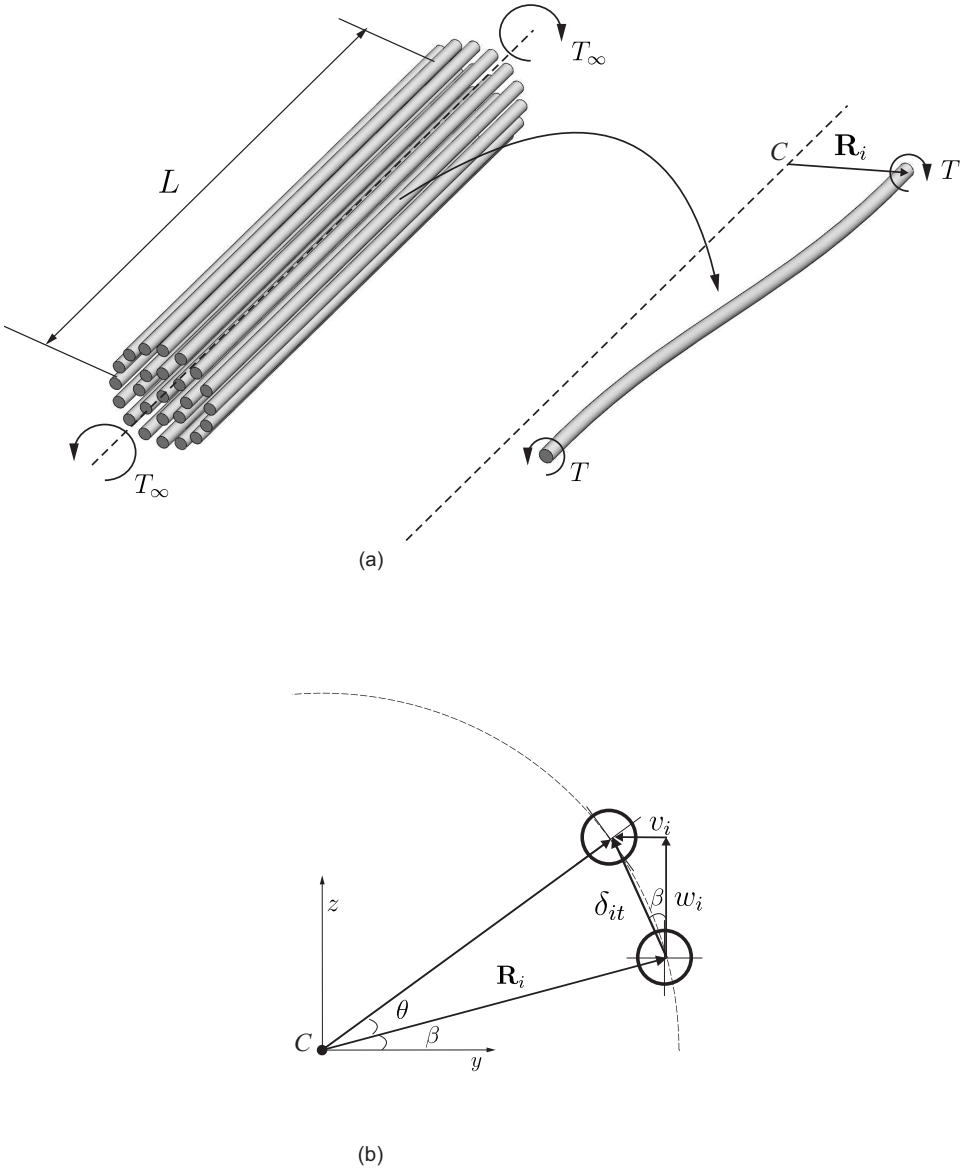

FIGURE 6.3: Schematics of (a) a free bundle of filaments under torque load, showing the deformation of the ith filament; (b) diagram showing a the displacement δ_{it} of the ith filament under twist with respect to an axis at a distance R_i from its central axis.

be equal to $v_i = -z_i \alpha L$ and $w_i = y_i \alpha L$ (α is the rate of twist per unit length and it is defined as $\alpha = \theta/L$) we obtain the following

$$v_i''(x) = \frac{6\alpha y_i}{L}\left(1 - \frac{2x}{L}\right) \tag{6.4a}$$

$$w_i''(x) = \frac{6\alpha z_i}{L}\left(\frac{2x}{L} - 1\right). \tag{6.4b}$$

Considering the contribution of the displacements in the y- and z-axes, the total strain

energy due to bending of the ith filament is given by $U_{bi} = (1/2)B\int_L (v_i''^2 + w_i''^2)\mathrm{d}x$, where B is the bending stiffness of the filament. Using equation (6.4) and integrating over the length L we obtain,

$$U_{bi} = \frac{6B\alpha^2}{L}\left(y_i^2 + z_i^2\right) = 6\frac{B\alpha^2}{L}\mathbf{R}_i^2 \tag{6.5}$$

where $\mathbf{R}_i^2 = y_i^2 + z_i^2$. The total strain energy due to bending is then given by the contribution of the deformation of all filaments as follows,

$$U_B = \frac{6B\alpha^2}{L}\sum_{i=1}^{N}\mathbf{R}_i^2 \tag{6.6}$$

where N is the total number of filaments in the bundle. Now the total strain energy of the bundle including the contributions from both twist and flexure is equal to

$$U = \frac{6B\alpha^2}{L}\sum_{i=1}^{N}\mathbf{R}_i^2 + N\left(\frac{1}{2}GJ_o\alpha^2 L\right) \tag{6.7}$$

where the first term on the right hand side of equation (6.7) corresponds to the flexure while the second term to the twist. The torsional stiffness of a filament with circular cross-section GJ_o can be related to the bending stiffness $B = EI_o$ as $GJ_o = EI_o/(1+\nu)$ so that the total strain energy can be rearrenged as

$$U = \frac{6B\alpha^2}{L}\left[\sum_{i=1}^{N}\mathbf{R}_i^2 + \frac{N}{12}\frac{L^2}{(1+\nu)}\right]. \tag{6.8}$$

The total potential energy is, therefore, a quadratic term in α. The potential energy due to external loading is defined as $V = -T_\infty \alpha L$ which is linear in terms of α. Minimisation of the total potential energy (using the Principle of minimum total potential energy) leads to the expression of the twist rate as function of the applied remote torque

$$\frac{T_\infty}{\alpha} = \frac{12B}{L^2}\left[\sum_{i=1}^{N}\mathbf{R}_i^2 + \frac{NL^2}{12(1+\nu)}\right]. \tag{6.9}$$

The first term on the right side of equation (6.9) corresponds to the stiffness due to the filaments flexure. The second term is associated with the twist of the filaments.

The expression derived for the stiffness of a group of filaments is now validated computationally. A finite element model created in Abaqus/CAE/Standard 6.13® (Simulia, Dassault Systmes, Providence, RI, USA) was used to create the mesh and carry out analysis under torsion. The models in each example consisted of different bundles of filaments that were subjected to torsion. The filaments were modelled as cylinders and meshed using linear tetrahedral elements C3D10. The FEA model is shown in figure 6.4. The nodes at one of the ends are fully fixed in all degrees of freedom. The nodes at the other end are tied to a rigid plate of infinite stiffness. A twist is applied through a point at the centre of the plate. This point is coincident to the centroid of the bundle of filaments. The twist axis of each examples passes through the centroid of each group of filaments, it is marked with a cross in figure 6.5, where the cross-sections of all the models tested are shown. The model in figure 6.5(a) has 25 filaments with radius $r = 0.5$ mm and it consists of a filament with its centroid being coincident to the centroid of the bundle and two circular rings of filaments, the first ring has eight filaments at $|\mathbf{R}_i| = 3$ mm, while the outer ring has 16 filaments at $|\mathbf{R}_i| = 6$ mm. The model of figure 6.5(b) has also 25 filaments: again a central filament, and 3 rings with 8 filaments in each at $|\mathbf{R}_i| = 3, 6$, and 9 mm. Models of figures 6.5(c) and 6.5(d) have the same distribution of filaments as those in model 6.5(a), with the difference that "filaments" have a square cross-sections of 1×1 mm. The difference between 6.5(c) and 6.5(d) is the orientation of the filaments. The purpose was to visually clarify the twist of the filaments. This is not clear with circular cross-sections because rotated circular sections obscure the amount of rotation and the patterns of rotation which rectangular sections do not. In figure 6.5(c), the orientation of the ith filament is normal to the vector $\mathbf{R}_i$. After twisting, the cross-section remains normal to the vector $\mathbf{R}_i$. In figure 6.5(d), all squares have the same orientation, having their orthogonal sides parallel to the y- and z-direction. After twisting, these should not remain aligned to the y- and z-axes.

As the torsional stiffness depends on its relative position with respect to the twist axis, $\mathbf{R}_i$ of all filaments lying on the same ring should contribute equally to the total stiffness. The stiffness of the structure in figure 6.5(b) should result in a higher stiffness than that in figure 6.5(a). This is because the structure in figure 6.5(b) has 8 filaments at a greater

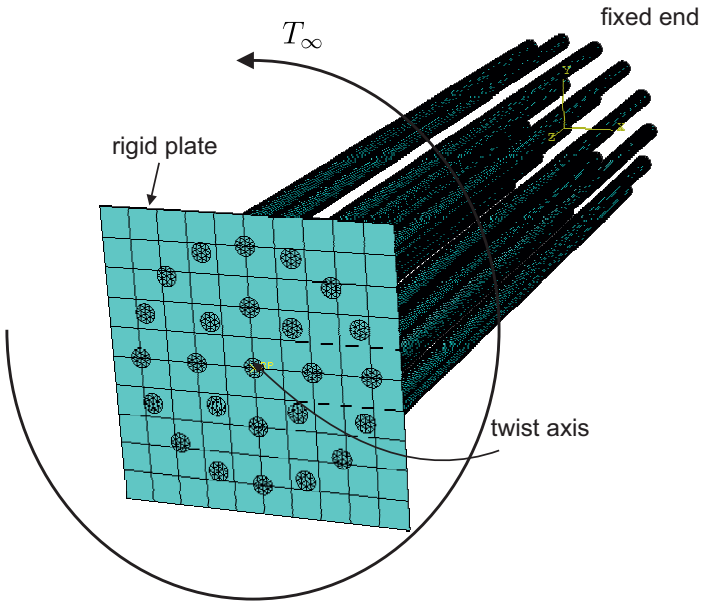

FIGURE 6.4: FEA model of a free bundle of filaments tied to a rigid plate through which a twist displacement is applied.

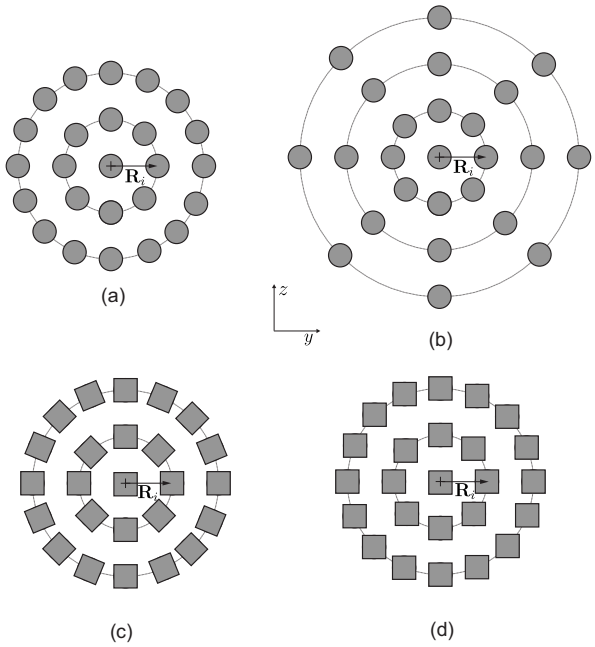

FIGURE 6.5: Schematics of the cross-sections of the samples used to validate the torsional stiffness of a bundle of filaments.

distance away from the twist axis. The models for 6.5(c) and 6.5(d) should result in the same torsional stiffness.

Results calculated using expression (6.9) were compared with those obtained from the FEA data. The comparison of the predicted values and the computational results is

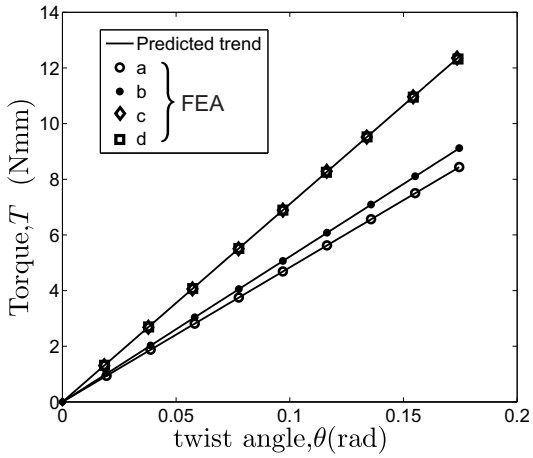

FIGURE 6.6: Comparison of the predicted trend and FEA data for examples described in figure 6.5.

shown in figure 6.6. As expected, model (b) shows a higher torsional stiffness because it has filaments located further away from the twist axis than model (a). Models (c) and (d) offer the same torsional stiffness, validating, the dependence on the relative position $\mathbf{R}_i$. The only difference between model (c) and (d) are the orientation of the filaments cross-section after undergoing twist. The deformed and undeformed shapes of the bundles cross-sections are shown in figure 6.7. Note that the cross-sections after undergoing twist have changed their orientation, validating the assumption that cross-sections do not remain plane. We now proceed to study the torsional stiffness of bar composed of the woodpile lattice, where in addition to the filaments running parallel to the twit-axis, we also have cross-filaments.

6.2 Apparent torsional stiffness of woodpile bars

We now extend the model for the torsional stiffness of the free bundle of filament to that for a slender bar composed of the woodpile stack of filaments. Consider the woodpile bar shown in figure 6.8 under the action of a remote torque T_∞. We assume that the filaments are bonded at a point, so that the relative rotation is allowed. The behaviour under the action of a remote torque T_∞ of the filaments that run parallel to the twist axis (x-axis) is similar to the filaments of the bundle, analysed in Section 6.1.2. Therefore, the strain energy contributed to the torsion of the woodpile bar can be obtained using

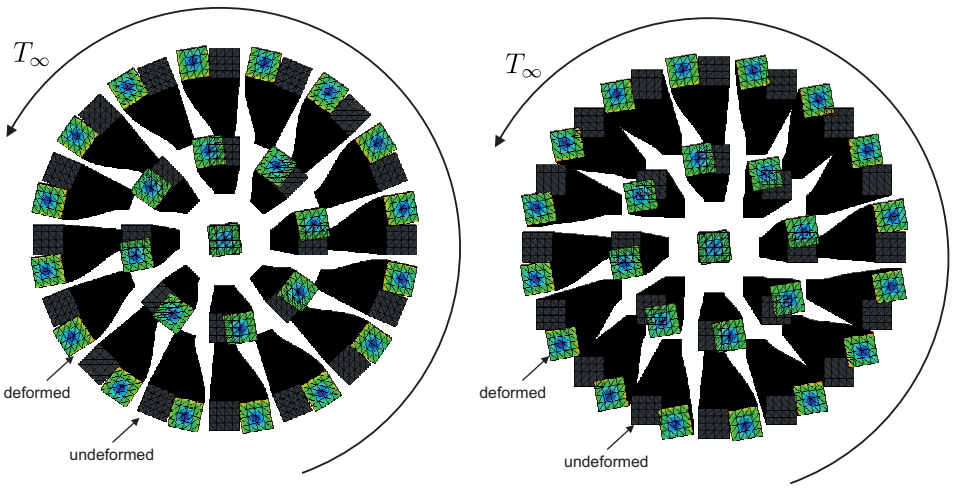

FIGURE 6.7: Comparison of the deformed cross-sections of models right and left from figure 6.5(c) and 6.5(d) respectively. The undeformed cross-section is also shown. The figure corresponds to a front view with perspective of the bundle of the filaments, having the x-axis going out of the paper. Note that the patterns of rotation in rectangular sections exhibit their twist.

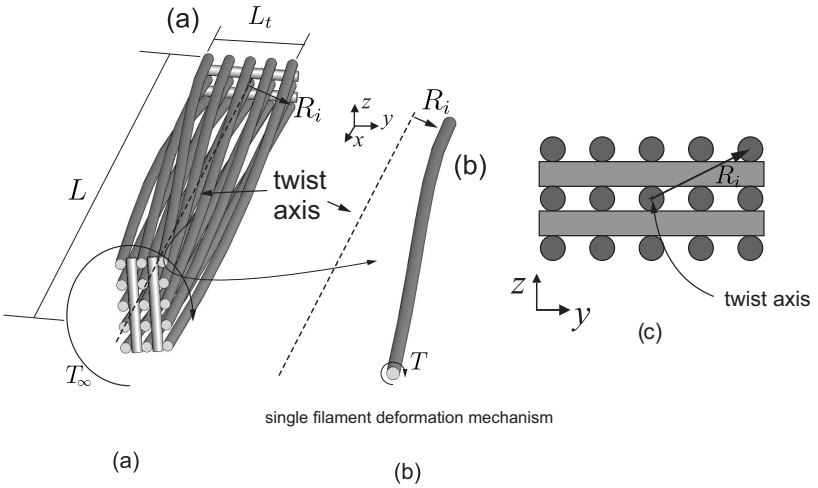

FIGURE 6.8: Schematics showing (a) the lattice subjected to remote torque T_∞, (b) a single filament showing the deformation mechanism resulting from the bending moment, at a distance R_i from the twist axis, and (c) the cross-section of the woodpile bar showing the relative distance of the ith filament.

equation (6.9). Here, the transverse filaments do not only keep the axial filaments at a certain distance from the twist axis, but they also deform at the same time with a twist rate equal to that of the axial filaments. Take the twist angle θ as the displacement w in the z-axis with respect to the width of the bar in the y-axis so that $\theta = \partial w/\partial y$. If we know the rate of twist α is equal to the change of the twist angle with respect to the

length of the bar in the x-axis as

$$\alpha_l = \frac{\partial \theta}{\partial x} = \frac{\partial}{\partial x}\left(\frac{\partial w}{\partial y}\right) \tag{6.10}$$

where the subscript l indicate that the twist rate corresponds to the axial filaments. Now consider the change in displacement w with respect to the length of the bar can be defined as $\partial w/\partial x$ so that its change with respect to the width in the y-axis of the bas is

$$\alpha_t = \frac{\partial}{\partial y}\left(\frac{\partial w}{\partial x}\right) \tag{6.11}$$

where the subscript t indicates that the twist rate corresponds to the transverse filaments. Equations (6.10) and (6.11) lead to $\alpha_l = \alpha_t$ because for a surface $w = w(x, y)$, $\frac{\partial^2 w}{\partial x \partial y} = \frac{\partial^2 w}{\partial y \partial x}$. Equation (6.8) can be extended by incorporating the strain energy due to the twist of the traverse filaments $U_t = (1/2)GJ_o(\alpha L_t)^2/L_t$; where L_t is the length of the transverse filaments.

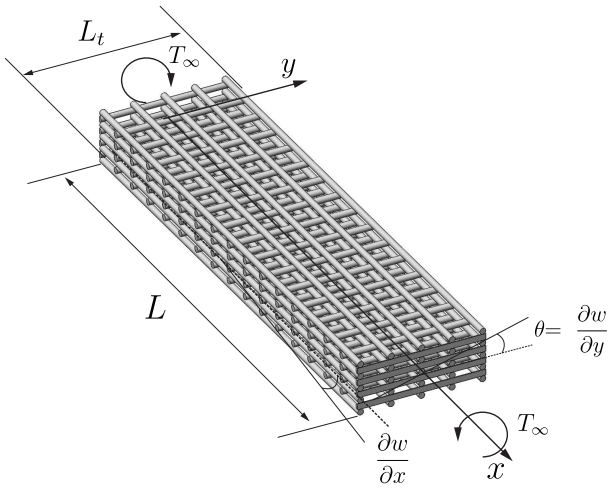

FIGURE 6.9: Strains due to torsion loading in a woodpile bar.

The total strain energy expression for the woodpile bar including the twist of the transverse filaments becomes,

$$U = \frac{6B\alpha^2}{L}\sum_{i=1}^{N}\mathbf{R}_i^2 + N\left(\frac{1}{2}GJ_o\alpha^2 L\right) + N_t\left(\frac{1}{2}GJ_o\alpha^2 L_t\right). \tag{6.12}$$

After grouping similar terms, equation (6.12) is rearranged as

$$U = \frac{6B\alpha^2}{L}\sum_{i=1}^{N} R_i^2 + \frac{1}{2}GJ_o\alpha^2\left(NL + N_tL_t\right). \tag{6.13}$$

After applying PMTPE taking the twist rate α as generalised coordinate, we have the following expression for the apparent torsional stiffness $\langle GJ\rangle_0$

$$\langle GJ\rangle_0 = \frac{T_\infty}{\alpha} = \frac{12B}{L^2}\left[\sum_{i=1}^{N} R_i^2 + \frac{L^2(N + N_tL_t/L)}{12(1+\nu)}\right], \tag{6.14}$$

where the subscript 0 denotes 0% overlap between filamentss, i.e. freely rotating but translationally tied joints. This expression is validated in Section 6.3.3, where the influence of the bonding between filaments is studied via FEA models.

6.3 The apparent torsional stiffness of woodpile bars with bonded filaments

Translationally tied filaments provide a lower bound to the lattice stiffness in twist, because in practice filaments are also restricted rotationally. The bending stiffness B of the axial filaments due to torsion scales with the length as $B \sim 1/L^3$. For woodpile bar with N number of transverse filaments in a single layer, when the joints offer torsional resistance, reducing the effective length at which the axial filaments bend by a factor of N, following the scaling as $B \sim N[1/(L/N)^3]$. The junctions between axial and transverse filaments will then behave as welded-joints. Clearly, counting N of these L/N long pieces of filaments and noting that $N[1/(L/N)^3] \gg 1/L^3$, which is reflected in the increment in apparent torsional stiffness. Such a deformation manifests itself as the apparent shear of a lattice. The apparent shear of the lattice, accounting for these aspects of micromechanics, is analysed in the next subsection.

6.3.1 Torsion of a woodpile and the apparent shear modulus

We analyse the case, when the filaments are considered welded now. This restriction forces the filaments to be at 90° at all times. The response under torque will then

be dominated by the apparent shear of the lattice material. If the woodpile bar is oriented such that the lattice lies in the xy plane, leaving the z-axis to be parallel to the stacking direction, then the relevant apparent shear modulus is $\langle G \rangle_{xy}$. The model for the apparent shear modulus $\langle G \rangle_{xy}$ was derived by Moongkhanklang et al. [8] for flat 2D lattices. They based their derivation on Euler-Bernoulli assumptions to represent the flexure of the filaments. We review the procedure here for the sake of clarity and completion, then we improve the model by using Timoshenko beam theory which is deemed necessary for the woodpile architecture.

Consider a 2D lattice shown in figure 6.10(a) under the action of a remote shear stress τ_∞. This case is equivalent to having the lattice material rotated 45° and loaded biaxially, as shown in figure 6.10(b). Now take the unit cell shown in figure 6.10(c), under the loads as shown. The biaxial loading will produce a deformation given by the flexure of filaments, as sketched in figure 6.10(d). A filament has been extracted from the unit cell and the free body diagram showing the forces acting on it are depicted in figure 6.10(e). The loading acting of the filaments is equivalent to a beam inclined at 45° under a vertical and a horizontal load (see figure 6.10(f)). The resultant force acting of the beam is labelled as F_s, and it is equal to $F_s = F\sqrt{2}$, producing a displacement δ_s. From Euler-Bernoulli beam theory we know that the displacement $\delta_s = F_s\lambda^3/12B$. This is the expression employed by Moongkhanklang et al. [8]. This approach is suitable for lattice with low relative densities, as it requires the filaments to be apart from each other at a distance λ such that EB assumptions are still reasonable. We can now extend the model presented in [8] by including shear deformations in the bending of the filaments. The displacement is now given by $\delta_s = F_s(\lambda^3/12B + \lambda/S)$ when filament shear is accounted for. The force F_s and the displacement δ_s can be related with the apparent stress and strain as

$$\tau_{xy} = \frac{F_s}{4r\lambda} \qquad \text{and} \qquad \frac{\gamma_{xy}}{2} = \frac{\delta_s}{\lambda}. \tag{6.15}$$

Using equation (6.15) and $\langle G \rangle_{xy} = \tau_{xy}/\gamma_{xy}$, the apparent shear modulus is obtained as

$$\langle G \rangle_{xy} = \frac{3BS}{24Br\lambda_x + 2Sr\lambda_x^3} \tag{6.16}$$

For a lattice with cylindrical filaments (i.e. $B = E\pi r^4/4$ and $S = \kappa G\pi r^2$), equation (6.16) can be expressed as a function of the volume fraction $\bar{\rho} = (\pi/2)(r/\lambda)$, given by

$$\langle G \rangle_{xy} = \frac{24EG\kappa\bar{\rho}^3}{96E\bar{\rho}^2 + G\kappa\pi^2}. \tag{6.17}$$

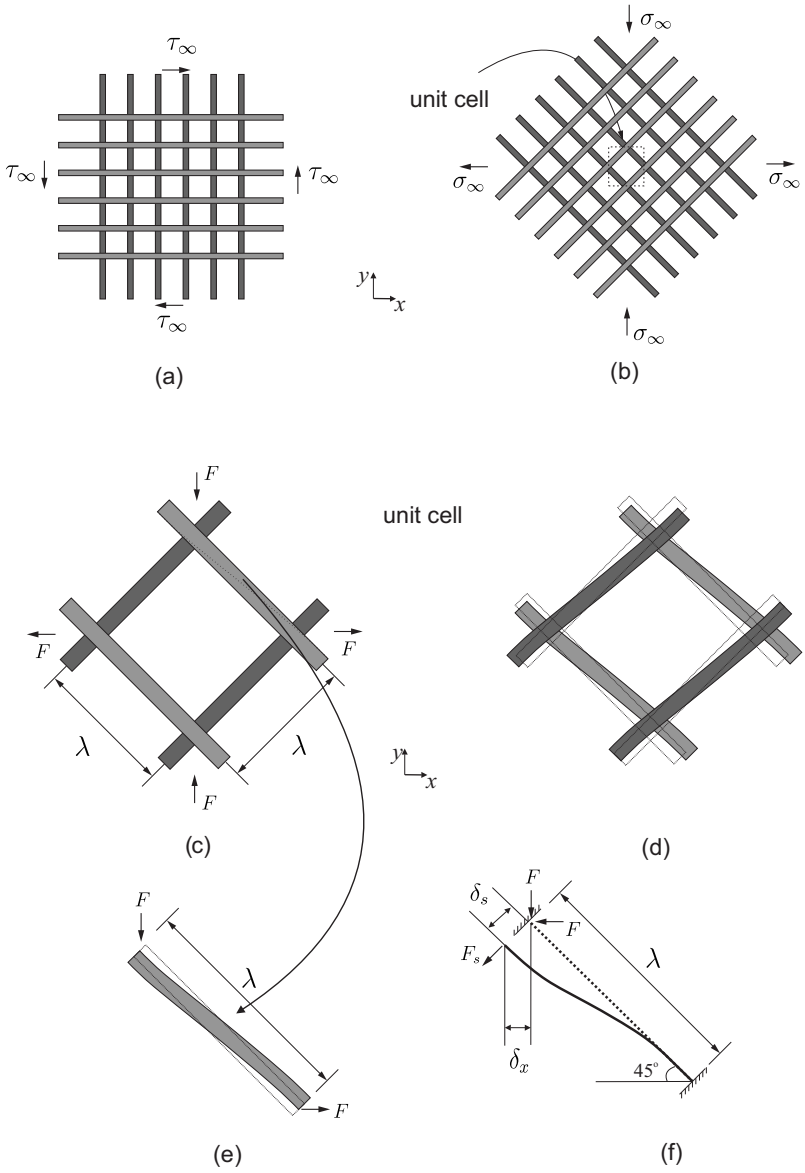

FIGURE 6.10: (a) Lattice material under shear loading in the xy plane, (b) equivalent lattice rotated 45° for analysis purposes, (c)-(d) unit cells showing the loading and deformed shapes qualitatively, and (e)-(f) beam models employed for modelling the bending of the filaments.

Results from the shear-inclusive analytical model presented here were compared against those derived from the model in [8], and against data obtained from computational experiments using FEA. The FEA model consisted of square lattice in one plane, this

was delivered employed in order to ensure that filaments were kept orthogonal between them. The filaments in the lattice were modelled using beam elements (B21) that include shear deformations with Abaqus/CAE/Standard 6.13® (Simulia, Dassault Systmes, Providence, RI, USA). The distance between filaments was kept fixed as $\lambda = 5$ mm and the radius varied $r \in [0.25, 1.25]$ mm to vary the relative density $\bar{\rho}$. The FEA model is shown in figure 6.11, where both the undeformed and the deformed shapes can be observed, confirming the bending deformation of the filaments. The results of the comparison are presented in figure 6.12. Also the shear-inclusive model developed here works for lattice with moderately high relative densities, due to the inclusion of shear correction in the deflection of the filaments as the match with FEA data is remarkable after including shear correction. By contrast, the model presented in [8] is valid only for lattices of low relative densities. Figure 6.12 also confirms the apparent shear modulus scaling relation to the relative density $\langle G \rangle_{xy} \sim \bar{\rho}^3$.

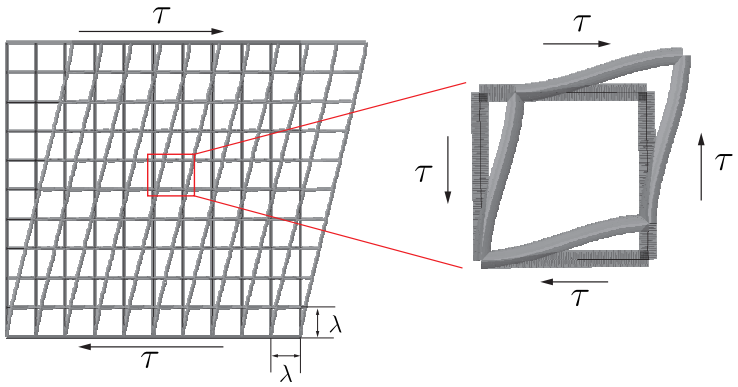

FIGURE 6.11: Deformed and undeformed lattice under shear stress. Deformed shape obtained from the FEA.

6.3.2 Woodpile torsion as lattice shear

If the woodpile bar is treated as a continuum with apparent properties, we can predict the torque-twist response with the well-known formula $T = \langle G \rangle_{xy} J\theta/L$, where J is the torsional constant related to the geometry of the cross-section. This approach does not take into account the twist of the filaments, as it only considers the bending of the filaments due to the shear deformations of the lattice as induced by torsion of the woodpile bar.

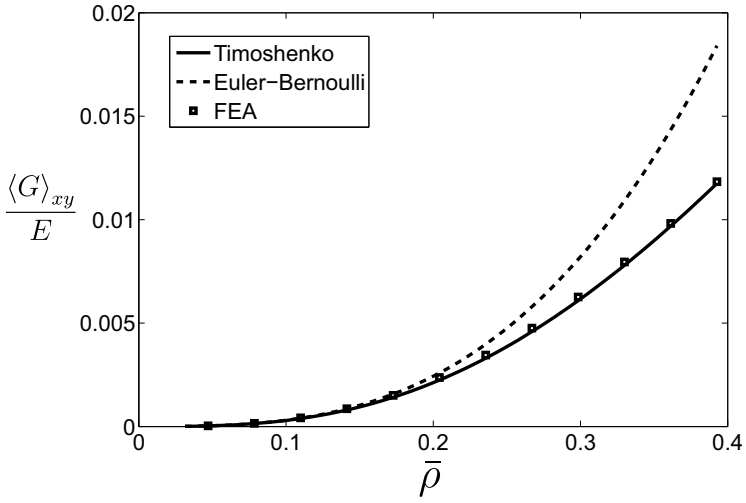

FIGURE 6.12: Analytical models for the apparent shear modulus $\langle G\rangle_{xy}$ as function of the relative density. The dotted line corresponds to the model derived in [8], using EB assumptions to model the bending of the filaments, while the solid line corresponds to the model expanded here including shear correction. The squares corresponds to the data obtained from FEA simulations.

Adding contributions arising from filament bending (which manifest itself as lattice shear) and filament twist, the strain energy expression

$$U = \frac{\alpha^2}{2}\left[\langle G\rangle_{xy} JL + GJ_o(N_a L + N_t L_t)\right] \tag{6.18}$$

is a quadratic expression in α. In equation (6.18) N_a and N_t correspond to the total number of axial and transverse filaments respectively. Combining this with the expression for the potential energy of external loading $V = -T_\infty L\alpha$ and apply PMTPE as before we obtain an expression for the apparent torsional stiffness as,

$$\langle GJ\rangle = \frac{T_\infty}{\alpha} = \left[\langle G\rangle_{xy} J + GJ_o(N_a L + N_t L_t)\right]. \tag{6.19}$$

The first term in equation (6.19) is based on the bending of filaments with an effective length of λ, while the second term is based on the twist of filaments with a length of L. The first term is significant because $\langle G\rangle_{xy}$ dominates the expression when the filament separation is not much grater than the filament radius.

6.3.3 Sensitivity to overlap

The sensitivity of twist response to the overlap factor OL, introduced in earlier chapters, is systematically studied here. We make use of an FEA model to assess the torsional stiffness as the overlap at the joints is increased.

The models were composed of a stack of filaments where the overlap was increased. The model consisted of a woodpile bar of length $L = 40$ mm, a width of $L_t = 10$ mm, and 5 layers giving a thickness of ≈ 3.6 mm. The model has 25 (5 layers made of 5 filaments each, separated at $\lambda = 2.5$ mm) filaments parallel to the twist axis, and a total of 64 filaments running transversally. The filaments of the lattice were modelled as cylinders of diameter $d = 0.5$ mm and meshed using linear tetrahedral elements C3D10. PLA material properties were used–the values chosen here are $E = 2290$ MPa (measured from the single filament tensile tests), $\nu = 0.36$ [101]. All the models tested made use of the boundary conditions described in Section 6.1.2 and were subjected to a twist of 1 degree.

The apparent torsional stiffness $\langle GJ \rangle$ assessed from FEA simulations is plotted in figure 6.13. Notice the significant increment in torsional stiffness, highlighting the sensitivity to the overlap. In practice, filaments are bonded in such a way that their rotation with respect to each other is restricted. The region of filament adhesion, which increases the apparent torsional stiffness now act as welded-joints. When the filaments are considered to be bonded with only translationally, we know that the bending of the axial filaments due to torsion scales with the length as $B \sim 1/L^3$. Whereas, for woodpile bar with N number of transverse filaments, the welded-joints reduce the effective length at which the axial filaments bend following the scaling as $B \sim N[1/(L/N)^3]$. The junctions between axial and transverse filaments define the welded-joints and the overhang $L/N = \lambda$. Clearly, $N[1/(L/N)^3] \gg 1/L^3$, reflected in the increment in apparent torsional stiffness.

The initial value of the curve in figure 6.13 that corresponds to the 0% overlap was predicted using equation (6.14). Using equation (6.19) the uper bound of the total strain energy was calculated. The prediction of the lower bound is in excellent agreement with the FEA data. Torsional stifness data exceeding the “upper bound” can be attributed

to two reasons–(i) the upper bound assumes restriction in relative displacement and rotation at a single point of adhesion; in the FEA model this is over a small partch of nodes, hus incresing the sitffness of the FEA model; (ii) theoretical results are for infinite lattices wheres FE model is finite.

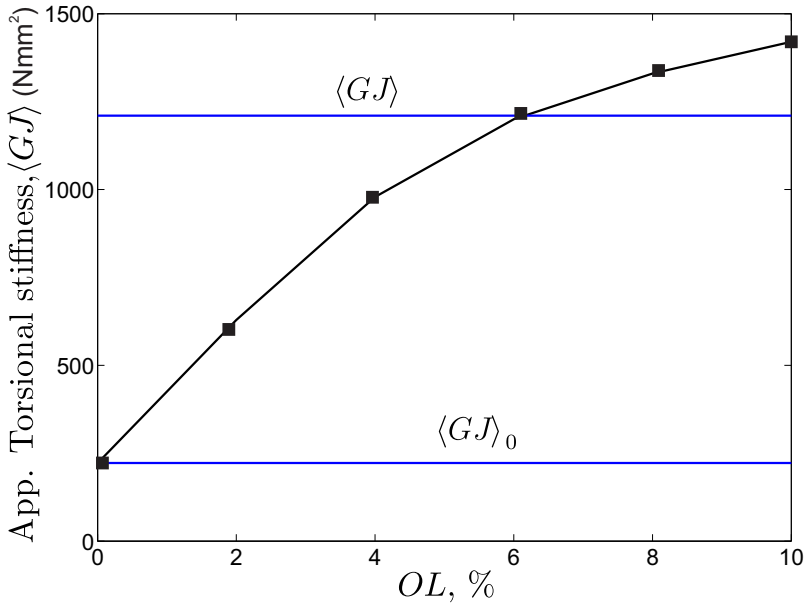

FIGURE 6.13: The resulting apparent $\langle GJ \rangle$ as function of the overlap between filaments. The value $\langle GJ \rangle_0$ corresponds to the torsional stiffness when the overlap is 0%. The curve converges to the value assuming fixed-joints between filaments.

6.4 Experimental determination of torsional stiffness of woodpile lattices

Torsional stiffness was measured for samples of FFF-manufactured slender structures. A schematic diagram of the test showing the orientation of the lattice under twist deformation is shown in figure 6.14. The measured torque-twist curves are presented and compared with analytical expressions.

6.4.1 Description of the machine used for torsional testing

The tensile testing machine used for tensile and bending tests in the previous chapters is not capable of applying torque. Therefore, INSTRON 8874 was used instead. This machine has a servohydraulic actuator capable of axial and torsional loading. This

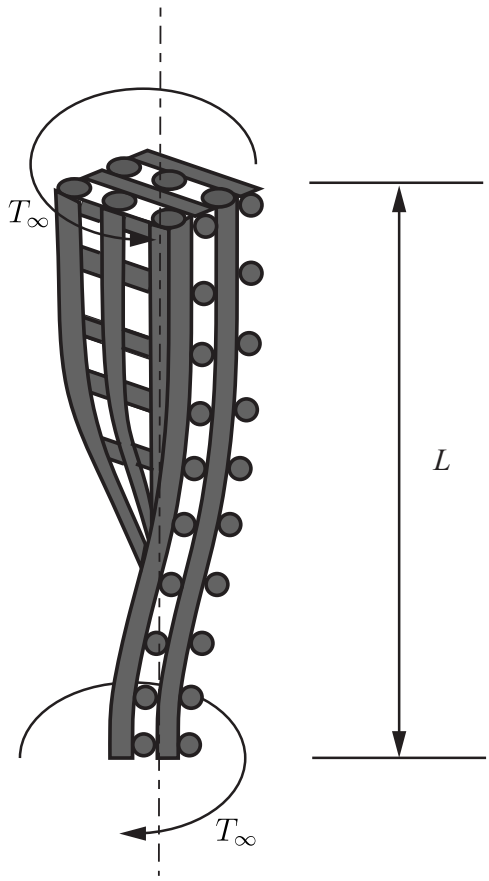

FIGURE 6.14: Schematic of the torsion test showing the orientation of the woodpile with respect to the twisting moment.

machine can be used for static and dynamic testing. Only the static and torque features were employed. The actuator is mounted on a twin-column frame, providing precision and stability. The performance parameters of this machine are summarised in Table 6.1 [110].

TABLE 6.1: INSTRON 8874 Performance Parameters.

Axial force capacity (kN)	25
Torque capacity (Nm)	100
Max. axial stroke (mm)	100
Max. rotation (deg)	130
Dynamic load capacity (kN)	10

6.4.2 Fabrication of the additively manufactured samples

A set of 10 dogbone samples comprising the lattice material were fabricated following the manufacturing procedure that has been described previously. The PLA samples

consisted of 6 layers so that $N_z = 6$ (1 layer is considered as 2 consecutive layers of the orthogonally stacked filaments). The section of the dogbone samples had a cuboid shape with dimensions of 85×17×6 mm. This narrow section is composed of a total of 18 filaments in the longitudinal axis ($N_x = 18$) and 85 in traverse axis ($N_y = 85$), in each layer. These filaments are extruded with a separation of 1 mm; parameter specified in the G-code. Details on the manufacturing parameters, such as the nozzle speed, extrusion speed, extrusion temperature, among others were presented in Chapter 3.

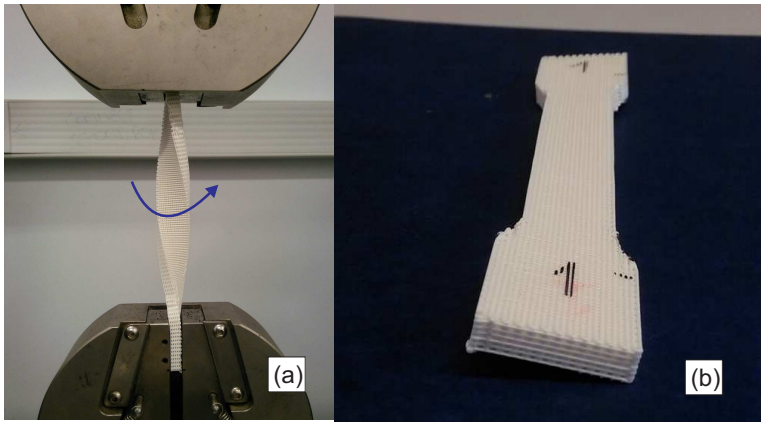

FIGURE 6.15: Photograph showing (a) a sample during the test where the deformation of axial filaments into a helix shape can be observed, and (b) a sample after the test, showing permanent deformation but no fracture.

6.4.3 Measurement of torsional response and comparisons with results from analytical models

The machine was used under twist control mode, setting the maximum rotation to 90°. The torque generated to twist the samples to the specified rotation was then recorded. A sample under torque load is shown in figure 6.15(a). The arrow indicates de torque direction. From figure 6.15(a), the deformation mechanism of the axial filaments can be clearly observed. As stated before, the axially running filaments undergo simultaneous twist and bending, deforming in a curved shape with resemblance to a space helix. The torque-twist curves measured of the set samples are shown in figure 6.16. In measured data for torque-twist, peaks were observed, presented at $\theta \approx 0.89$ rad and $\theta \approx 1.57$ rad, and were produced when cables hit the grippers that hold the samples. The sensitivity of the load cell is such that this impacts reflected in the measured data with the sudden raised in the torque. These noisy peak values were filtered out by obtaining the

local average value at the twist value where the peek occurred. The filtered curves are presented in figure 6.16.

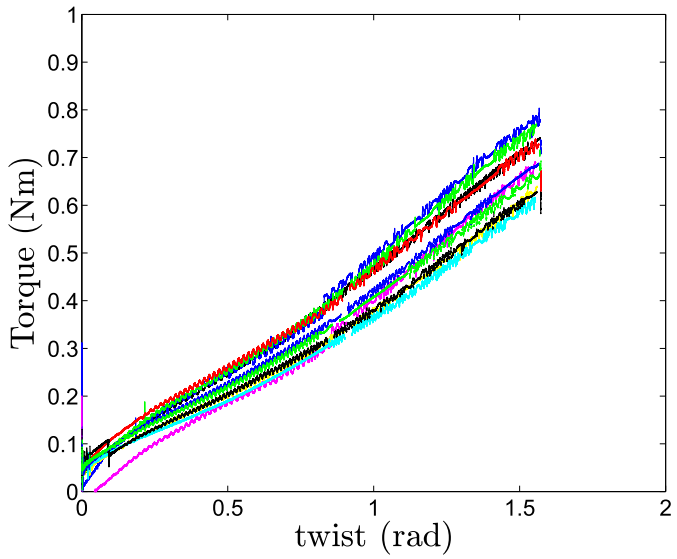

FIGURE 6.16: The resulting torque-twist curves of the whole set of samples.

Within the range of test (0° to 90° twist) none of the samples fractured. Despite the large angle of rotation applied, the samples showed nearly complete elastic recovery and almost no permanent deformation was observed upon removing the load. A photograph of a sample dismounted after the test is presented in figure 6.15(b), The sample can be observed to be slightly twisted, but the original shape was recovered almost completely.

The results presented in figure 6.16 were interpolated using the tool option in the software MATLAB. The mean of the linearised data is shown now with dots in figure 6.17, showing with error bars the distribution of the data. Using equations (6.14) (dotted) and (6.19) (solid), two predicted trends are presented in figure 6.17. Equation (6.19) gives a better prediction, as FFF-samples have cross-links that restrict the bending of the filaments.

We used the analytical model given in equation (6.19) to predict the torque-twist curve. For $\lambda = 1$ mm, and the material properties $E = 2290$ MPa, $\nu = 0.36$ [101], $G = 841.11$ MPa, the apparent shear modulus was calculated as $\langle G \rangle_{xy} = 40.1$ MPa, and $L = 88$ mm, J was calculated for a rectangular cross-section with dimensions 17×6 mm as $J = 877.6$ mm^4 [109]. This prediction was compared against the experimental data in figure 6.17.The prediction is in good agreement with the experimental data, confirming

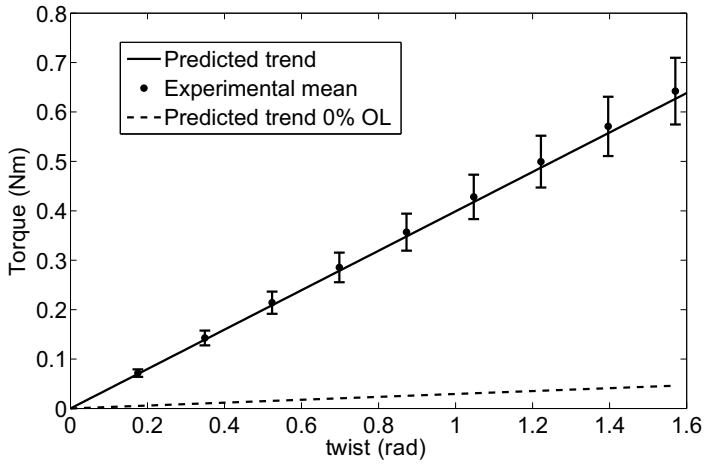

FIGURE 6.17: Comparison of the mean of the experimental data with the predicted trends. The dotted line corresponds to the model assuming the bonding to pin-jointed, and the solid line corresponds to the model assuming welded joints. The error bars are shown the distribution of the experimental data.

that the bonding between the filaments is such that it can be considered fully-fixed. This was also confirmed from the SEM of the samples cross-section as shown in figure 6.18.

The SEM micrograph of the cross-section of the woodpile samples used in the torsion tests is shown in figure 6.18. To observe the adhesion at the interface of alternating layers, the structure was fractured by dipping it in liquid nitrogen and impacting. In figure 6.18, we can observe that the bonding between the filaments is considerable. This suggests that the rotation between filaments is restricted, suggesting that the shear modulus presented in Section 6.3.2 dominates the torsional response of the woodpile bar.

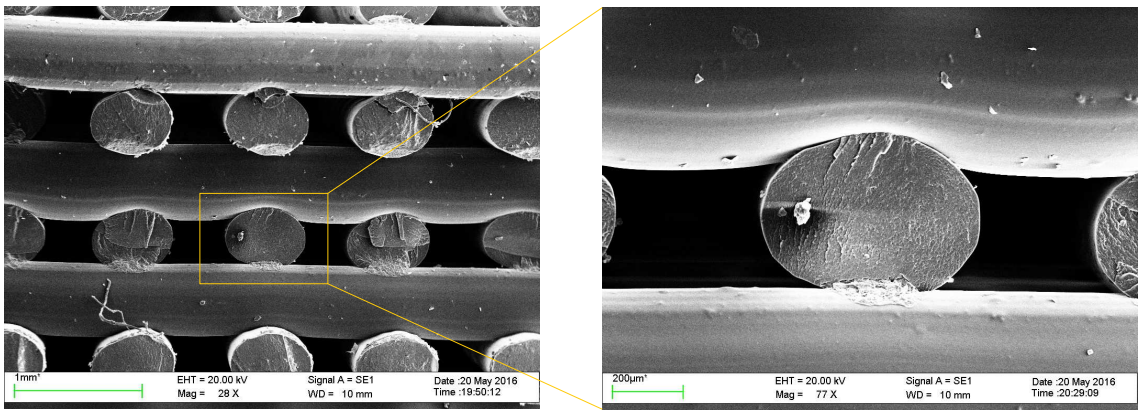

FIGURE 6.18: SEM micrograph of a section of the cross-sectional area in the torsion samples.

6.5 Conclusions

The torsional properties of woodpile bars were studied in this chapter. The deformation mechanism of the filaments is identified as twist and flexure of filaments. The micromechanics thus identified enabled us to develop analytical models to predict the apparent torsional stiffness. Two models considering different adhesion between filaments were developed. The first model presented assumed the filaments to be constrained translationally at a point, while allowing relative rotation. The second model presented assumes the filaments to be welded, and the torsional stiffness is dominated by the apparent shear modulus of the lattice material. The apparent shear modulus is that on the plane of the filaments, and showed a scaling relation with relative density as $\langle G \rangle \sim \bar{\rho}^3$.

The two models are the lower and upper bounds of the apparent torsional stiffness, respectively. When the adhesion between restricts the rotation between filaments, the effective length for flexural deformation is reduced. This is reflected in an increment of the torsional stiffness. The results of the two models developed were compared to experimentally measured data. Woodpile samples fabricated with FFF were subjected to torsional tests. The model that assumes welded filaments showed a good prediction of the torque-twist curve. An SEM micrograpgh of a section of the FFF-bar was presented to corroborate that the filaments were bonded in such a way that the relative rotation between them is restricted.

Chapter 7

The apparent elasticity of woodpile lattices in the stacking direction

In this chapter, the compressive elastic stiffness in the stacking direction of the 3D-printed woodpile lattice is studied. When lattices of arrangements shown in figure 7.1(a) and 7.1(b) are remotely loaded in the x- or $y-$axes, the elastic response is given by the elastic tension or compression of the filaments parallel to the loading direction. This elastic response was considered in Chapter 4. By contrast, the apparent Young's modulus along the stacking direction z is compared for the two arrangements now. Controlled deposition of matter in AM techniques enables the production of both configurations with almost no change in the manufacturing process. These two considered arrangements show significant differences in their apparent stiffness. They are taken up in turn next.

7.1 Symmetric staggered arrangement

Consider the compression of a 3D-printed lattice of the staggered arrangement under a remote stress σ_∞, as shown in figure 7.1(a). The staggered of the filaments is such that cross-linking filaments belonging to the neighbouring layers are located centrally

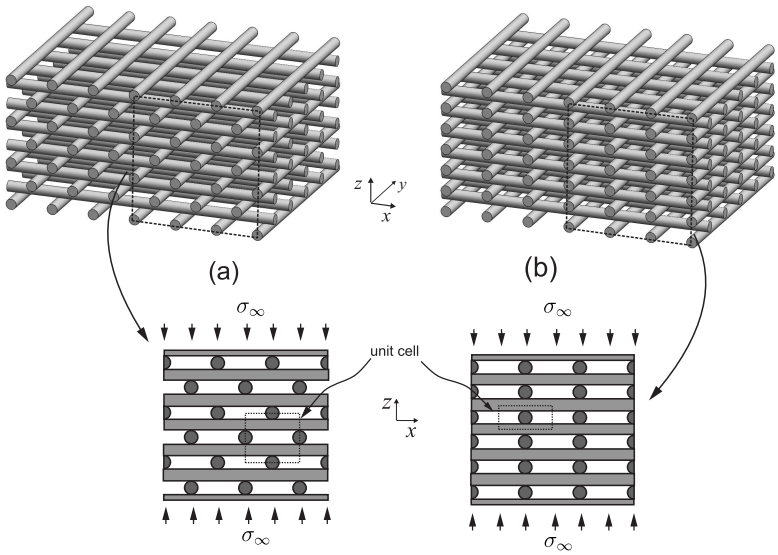

FIGURE 7.1: Schematics of the two woodpile arrangements studied: (a) staggered and (b) aligned configuration.

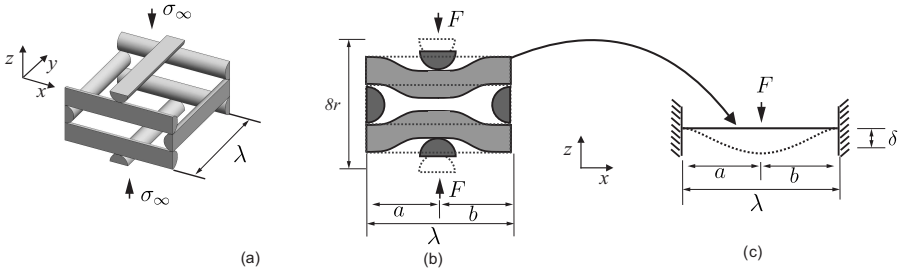

FIGURE 7.2: (a) 3D and (b) 2D schematics of the unit cell corresponding to the symmetric staggered arrangement. The dotted contour represents the undeformed unit cell. (c) the representative beam used to model the bending of the filaments.

over filament segments overhanging between support filaments underneath them. The filaments that are parallel to the x-axis bend because of the constraints imposed by the filaments that are parallel to the y-axis (appearing as circles in figure 7.1(a)). To analyse the flexure of the filaments we take a unit cell as shown in figure 7.2(a). The bending of the four half-cylinders that appear parallel to the x-axis in figure 7.2(a) can be simplified to the equivalent "2D" case as shown in figure 7.2(b). Due to the conditions imposed by the periodicity and symmetry of the structure the filaments can be treated as beams fixed at both ends under a transverse force F acting at the mid-point of the overhang. A thin beam model of this is shown in figure 7.2(c). From elementary beam theory, a beam of length L under these boundary conditions experiences the maximum transverse displacement at the point of application of the load and it is given by $\delta = FL^3/192EI$, where E the Young's modulus and I the second moment of area. For the woodpile

lattice, the effective length of the filaments in flexure is equal to the overhang $L = \lambda$. To obtain the apparent stress $\langle\sigma\rangle$ consider that the force F is distributed on the apparent area of the unit cell of figure 7.2(a) $A = \lambda^2$. The apparent strain $\langle\varepsilon\rangle$ is obtained by considering the original length in the z-axis is considered as $8r$ so that the apparent stress and strain are obtained as

$$\langle\sigma\rangle = \frac{F}{\lambda^2} \qquad \text{and} \qquad \langle\varepsilon\rangle = \frac{2\delta}{8r}. \tag{7.1}$$

Using equation (7.1) and making use of the identity $\langle E\rangle_s = \langle\sigma\rangle/\langle\varepsilon\rangle$, the expression for the apparent Young's modulus is obtained as

$$\langle E\rangle_s = \frac{768EIr}{\lambda^5}. \tag{7.2}$$

The subscript s indicates that the apparent property corresponds to the staggered configuration. For filaments with circular cross-section, $I = r^4(\pi/4)$. Substituting this in expression (7.2), we obtain the relation $\langle E\rangle_s \sim (r/\lambda)^5$. This allow us to express the apparent Young's modulus as function of the volume fraction $\bar{\rho}$, given by

$$\langle E\rangle_s = CE\bar{\rho}^5 \tag{7.3}$$

where $C = 6144/\pi^4$ is a non-dimensional constant. Equation (7.3) is suitable for lattices with low relative density, as it is based on the deflection of slender beams. We further extend the applicability of the equation (7.3) by taking into account the shear deformations in the flexure of relatively short overhang. Considering Timoshenko correction, the traverse displacement of a beam shown in 7.2(c) is given by $\delta = \frac{FL^3}{192EI} + \frac{FL}{4S}$, where S is the shear stiffness given by $S = \kappa G a_0$. Here G is the shear modulus of the filament material, κ is the shear correction factor, and a_0 is the cross-sectional area of the filament. Using the expression for the displacement described in equation (7.1), the apparent Young's modulus is now obtained as,

$$\langle E\rangle_{sT} = \frac{768rEIS}{48EI\lambda^3 + S\lambda^5}. \tag{7.4}$$

The subscript sT denotes that the property refers to the staggered arrangement developed incorporating Timoshenko shear correction. We can establish a relationship between equations (7.2) and (7.4), by taking $S = \kappa G \pi r^2$ and dividing the numerator and denominator of equation (7.4) by $\kappa G \lambda^5$. For materials with large porosity, i.e. $\bar{\rho} << 1$, the expressions coincide. This demonstrates that for low relative densities, Euler-Bernoulli micromechanics are adequate to predict the apparent Young's modulus. Rearranging terms, $\langle E \rangle_{sT} = \langle E \rangle_s / (1 + \epsilon)$, where $\epsilon = 48 E \bar{\rho}^2 / (\kappa G \pi^2)$. E and G can be related via the Poisson's ratio ν as $E/G = 2(1 + \nu)$. Taking $\nu = 0.36$ for PLA [101], and shear coefficient for circular cross-sections of $\kappa = 0.9$ [109] we obtain $\epsilon \approx 14.70 \bar{\rho}^2$. Using Taylor series expansion the apparent Young's modulus including shear correction can be expressed as,

$$\langle E \rangle_{sT} \approx \langle E \rangle_s (1 - 14.70 \bar{\rho}^2) + \mathrm{O}(\bar{\rho}^4). \tag{7.5}$$

The enhancement of equation (7.2) by the inclusion of shear within the filaments of the woodpile is exposed with the following examples. For example, for $r/\lambda = 1/10$, $\bar{\rho} = \pi/20$, which gives an $\langle E \rangle_{sT}$ equal to 63% of modulus predicted using Euler-Bernoulli model for filaments i.e. $\langle E \rangle_{sT} \approx 0.63 \langle E \rangle_s$, indicating a correction of 37% for lattices with $\bar{\rho} < 0.15$.

The model developed here neglects the deformation at the joints, as it assumes the dominant deformation mechanism under loading conditions studied, is that of the flexural response of the filaments. The model is restricted to lattices where the distance between filaments is such that they can still be treated as beams and when the filaments of adjacent layers are located at the midpoint between filaments of subsequent layers. The next section contains a general case for different staggered arrangements.

7.2 Asymmetric staggered arrangement

Consider now the lattice geometry shown in figure 7.3(a), where the staggered of the filaments is not symmetric. This structure is also dominated by the bending of the filaments. A beam with fixed-fixed end conditions demands a zero slope at both ends, which is not satisfied by for the asymmetric configuration. Each horizontally running beam is periodically supported as shown in figure 7.3(b). The asymmetrically loaded

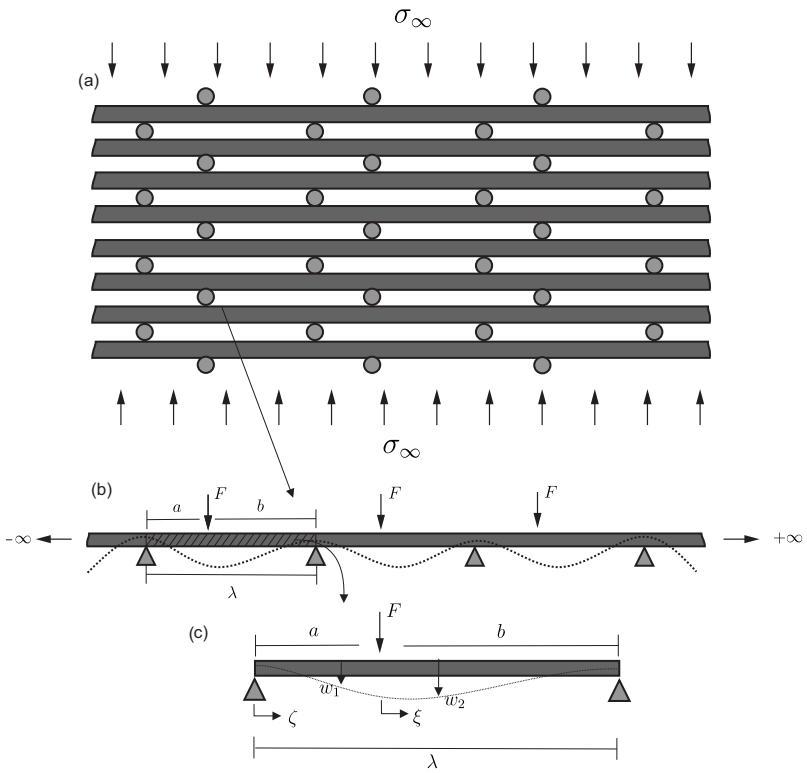

FIGURE 7.3: (a) Schematic of the asymmetric staggered arrangement, (b) and (c) showing the periodic beam and free body diagram for the analyis.

span is shown in figure 7.3(b). Periodic support ensures no deflection at these locations. However, the slope at these support points cannot be prescribed. There are additional conditions due to periodicity that need accounting for. Consider one span within the periodic beam as shown in figure 7.3(c). Except at the point of loading, the beam is free of external loading. So the beam can be analysed by splitting it into parts, the left beam has a length of a, while the length of that on the right is b. We define the coordinate system for the left beam as $\zeta = 0$ to be at the left support, and the load is applied at $\zeta = a$. For the right beam the load is applied at $\xi = 0$ and the support at the right end is at $\xi = b$. The deflection of the two beams with Euler-Bernoulli assumptions is given by

$$EI\frac{\mathrm{d}^4 w_1}{\mathrm{d}\zeta^4} = 0, \qquad 0 \leq \zeta \leq a \tag{7.6a}$$

$$EI\frac{\mathrm{d}^4 w_2}{\mathrm{d}\xi^4} = 0, \qquad 0 \leq \xi \leq b. \tag{7.6b}$$

Note that the right side of the above two equations is zero. The displacement for left and right beams is expressed as $w_1(\zeta)$ and $w_2(\xi)$. The solution of the 4th order differential equations is given by the two cubic expressions in the terms of the local coordinates ζ and ξ:

$$w_1(\zeta) = a_0 + a_1\zeta + a_2\zeta^2 + a_3\zeta^3 \tag{7.7a}$$

$$w_2(\xi) = b_0 + b_1\xi + b_2\xi^2 + b_3\xi^3. \tag{7.7b}$$

These two solutions require 8 boundary conditions to determine the yet unknown constants a_0 to a_3 and b_0 to b_3. Displacement at the supports must be zero i.e.

$$w_1(\zeta = 0) = 0 \qquad \text{and} \qquad w_2(\xi = b) = 0. \tag{7.8}$$

Due to the periodicity, at the supports there should have slope continuity so that slope $\partial w_1/\partial\zeta$ coming from the left $\zeta = 0^-$ should be equal to the slope $\partial w_1/\partial\zeta$ from the right $\zeta = 0^+$. Because of translational symmetry, the slope at the left support $\zeta = 0$ must be equal to the slope at the right support $\xi = b$ as,

$$\left(\frac{\mathrm{d}w_1}{\mathrm{d}\zeta}\right)_{\zeta=0} = \left(\frac{\mathrm{d}w_2}{\mathrm{d}\xi}\right)_{\xi=b} \tag{7.9}$$

Similarly, due to moment continuity at the supports gives

$$\left(\frac{\mathrm{d}^2w_1}{\mathrm{d}\zeta^2}\right)_{\zeta=0} = \left(\frac{\mathrm{d}^2w_2}{\mathrm{d}\xi^2}\right)_{\xi=b}. \tag{7.10}$$

Applying (7.8), (7.9) and (7.10) to (7.7) we obtain the following set of equations:

$$a_0 = 0, \tag{7.11a}$$

$$b_0 = -(b_1 b + b_2 b^2 + b_3 b^3), \tag{7.11b}$$

$$a_1 = b_1 + 2b_2 b + 3b_3 b^2, \tag{7.11c}$$

$$a_2 = b_2 + 3b_3 b. \tag{7.11d}$$

We require 4 further conditions. They are provided by the continuity of displacement, slope, moment and the shear fore at the point of application of the externally applied transverse force F:

$$w_1(\zeta = a) = w_2(\xi = 0), \tag{7.12a}$$

$$\left(\frac{\mathrm{d}w_1}{\mathrm{d}\zeta}\right)_{\zeta=a} = \left(\frac{\mathrm{d}w_2}{\mathrm{d}\xi}\right)_{\xi=0}, \tag{7.12b}$$

$$\left(\frac{\mathrm{d}^2 w_1}{\mathrm{d}\zeta^2}\right)_{\zeta=a} = \left(\frac{\mathrm{d}^2 w_2}{\mathrm{d}\xi^2}\right)_{\xi=0}, \tag{7.12c}$$

$$EI\left(\frac{\mathrm{d}^3 w_1}{\mathrm{d}\zeta^3}\right)_{\zeta=a} = EI\left(\frac{\mathrm{d}^3 w_2}{\mathrm{d}\xi^3}\right)_{\xi=0} + F. \tag{7.13}$$

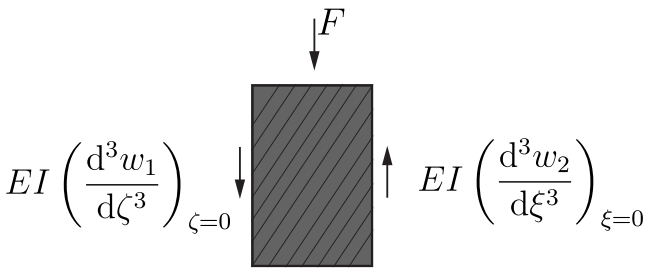

FIGURE 7.4: Free body diagram showing the shear force continuity at the poin where the force F is applied.

Note that the differential on the above expression is with respect to the local coordinates ζ or ξ as appropriate. The last of the above four conditions arises from the force body diagram at the point of application of the external force F (see figure 7.4). Applying

(7.12) and (7.13) to (7.7), we obtain the following set of equations

$$a_3 = \frac{b_0 - a_1 a - a_2 a^2}{a^3}, \tag{7.14a}$$

$$b_1 = a_1 b + 2a_2 a + 3a_3 a^2, \tag{7.14b}$$

$$b_2 = a_2 + 3a_3 a, \tag{7.14c}$$

$$b_3 = a_3 + \frac{F}{6EI}. \tag{7.14d}$$

Combining (7.11) and (7.14) leads to a system of 8 equations with 8 unkowns, that can be arrange in the following matrix form

$$[\mathbf{K}]\{\mathbf{q}\} = \{\mathbf{f}\} \tag{7.15}$$

where $\{\mathbf{q}\} = \{a_0, \cdots, a_3, b_0, \cdots, b_3\}^T$, $\{\mathbf{f}\} = \{0, 0, 0, 0, 0, 0, 0, F/6EI\}^T$ and the coefficient matrix is given by

$$[\mathbf{K}] = \begin{bmatrix} 1 & 0 & 0 & 0 & \hat{0} & 0 & 0 & 0 \\ 0 & 0 & 0 & 0 & 1 & b & b^2 & b^3 \\ 0 & 1 & 0 & 0 & 0 & -1 & -2b & -3b^2 \\ 0 & 0 & 1 & 0 & 0 & 0 & -1 & -3b \\ 1 & a & a^2 & a^3 & -1 & 0 & 0 & 0 \\ 0 & 1 & 2a & 3a^2 & 0 & -1 & 0 & 0 \\ 0 & 0 & 1 & 3a & 0 & 0 & -1 & 0 \\ 0 & 0 & 0 & 1 & 0 & 0 & 0 & -1 \end{bmatrix}. \tag{7.16}$$

The system of equations (7.15) was solved symbolically using *Mathematica*®. The solution for the displacement at the point of the application of load $w_1(a) = w_2(0) = b_0$ provides information to calculate the apparent strain to calculate the apparent Young's modulus $\langle E \rangle_s$. So, from the solution to the system of equation we obtain b_0, as

$$\delta = b_0 = \frac{a^2 b^2 F}{12(a+b)EI} \tag{7.17}$$

where δ is the displacement under the load F. Substituting equation (7.17) into equation (7.1), and using $b = \lambda - a$ we obtain an expression for the apparent Young's modulus as

$$\langle E \rangle_s = \frac{48EIr}{a^2\lambda(\lambda - a)^2}. \tag{7.18}$$

This expression contains the dependence of $\langle E \rangle_s$ on the position of the filaments. The denominator in equation equation (7.18) is a 4th degree polynomial and, therefore, $\langle E \rangle_s \sim a^4$. Note that in the limit of $a/\lambda = 0.5$ equation (7.18) coincides with equation (7.2). The lowest value for the apparent Young's with respect to a is obtained when $a/\lambda = 0.5$. As the filaments are located further away from the mid-point, the structure becomes stiffer following the scaling relation as $\langle E \rangle_s \sim a^4$. The increment in stiffness is given by the reduction of the length of one of the sides of the filament in flexure, increasing its resistance to bend. The model developed here is limited to positions in which the parameter b is such that it still gives enough length for the filament to bend, when b is approaching to zero but still not exactly 0 the prediction of $\langle E \rangle_s$ becomes far more complex. We do not cover this extreme case here. But, in the limit of $(a/\lambda) = 1$, the expression (7.18) becomes singular. The ratio $(a/\lambda) = 1$ corresponds to the arrangement where the filaments are aligned in the stacking direction. The deformation mechanism is different in this configuration and it is analysed in the next section.

7.3 The apparent Young's modulus for the aligned arrangement

In the previous section, we addressed the sensitivity of the apparent Young's modulus to the relative position of the filaments. Also the limit of the applicability of equation (7.18) was brought out. When $a = 0$ or $a = \lambda$, the configuration corresponds to the aligned arrangement.

The elastic response of structures with the aligned arrangement, under the action of a remote stress, is given by the deformation at point of adhesion between filaments. The analysis in this section is divided in two parts: firstly, we assume that the filaments are

in pure contact bonded at one point, and then the bonding between them is represented by an overlap of finite size.

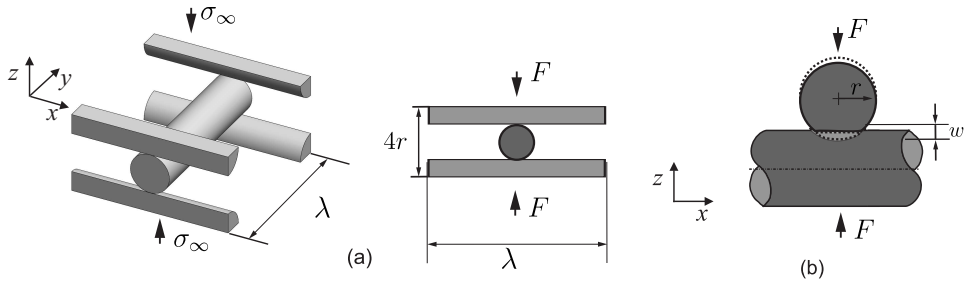

FIGURE 7.5: (a) Unit cell for the aligned arrangement, and (b) the schematic of the elastic compression of two equal diameter cylinders orthogonally stacked. The dotted contour represents the undeformed shape.

7.3.1 Filaments bonded at one point

It has been shown that the woodpile is obtained with having the filaments bonded with an overlap between them [53]. The case of pure contact between filaments is presented here for completeness. Consider the lattice presented in figure 7.1(b), subjected to a remote compressive stress σ_∞ as shown in figure 7.5. The response is dominated by the local elastic deformation at each junction of adjacent filaments. We start the analysis by considering the unit cell depicted in figure 7.5(a). The filaments, represented by cylinders, are compressed in the direction of the stacking by the force F. This problem can be studied by comparing it with point contact between two cylinders orientated at 90°. The two cylinders in contact are made of the same material (E, ν) and with the same cross-sections. The contact mechanics of this problem were studied by Puttock and Thwaite [111]. A summary of the derivation in [111] is presented here. Puttock and Thwaite obtained a solution by making use of the expression derived by Prescott in [112] for the displacement w at the point (x, y) of a plane, induced by the pressure p applied at (x',y'),

$$w(x,y) = \frac{1-\nu^2}{\pi E}\frac{p(x',y')}{r_0}\mathrm{dx'dy'} \tag{7.19}$$

where r_0 is the distance from the point (x',y') to the point (x, y) where the displacement w is calculated. They obtained a closed form solution based on the assumptions of frictionless contact of perfectly smooth 2^{nd} degree surfaces. Parametrising the expression that describe the curvatures of the two bodies in contact, the equation relating the total

deformation at the contact surface to the pressure is given by

$$\left(\frac{1-\nu_1^2}{\pi E_1}+\frac{1-\nu_2^2}{\pi E_2}\right)\int\int_A \frac{p(x',y')}{r_0}\mathrm{d}x'\mathrm{d}y' = w - Ax^2 - By^2 \tag{7.20}$$

where ν_1, ν_2, E_1, E_2 are the Poisson's ratio and Young's moduli of the two bodies in contact. The right side of equation (7.20), corresponds to the parametric expression of curvatures of the bodies in contact, so that parameters A and B contain the information relating the principal radii of curvature of the surfaces in contact, and the terms to describe curvatures in same coordinate system. In the case of the two cylinders in contact, these parameters contain the radii of the cylinders cross-sections. The objective now is to obtain the solution to equation (7.20). This is achieved by using an analogy with the ellipsoid problem in potential theory. The solution by potential theory involves integrals to obtain some of the parameters defining the contact area. This leads to a non-linear relation between the force F and the displacement w. Using the solution presented in [111] the centre of the two cylinders are brought to each other by a distance w, as

$$w = \left(\frac{9}{2}\right)^{1/3}\left(\frac{1-\nu^2}{E}\right)^{2/3}\left(\frac{1}{2r}\right)^{1/3}F^{2/3}. \tag{7.21}$$

We now proceed to incorporate this in the study of the apparent Young's modulus of woodpile lattices. Take the unit cell in figure 7.5(a), filaments are compressed each other from neighbouring layers, each filament in an infinite lattice will be under the loading from the top and the bottom layers. In other words, in each unit cell the compression in the axis perpendicular to the printing plane is equal $2w$. The apparent strain is calculated as

$$\langle\varepsilon\rangle = \frac{w}{2r}. \tag{7.22}$$

The apparent stress is defined as $\langle\sigma\rangle = F/\lambda^2$ and the apparent Young's modulus obtained as $\langle E\rangle_a = \langle\sigma\rangle/\langle\varepsilon\rangle$.

$$\langle E\rangle_a(\varepsilon) = \frac{\Delta\sigma}{\Delta\varepsilon}, \tag{7.23}$$

where $\Delta\langle\sigma\rangle$ and $\Delta\langle\varepsilon\rangle$ represent differential increments of the apparent stress and apparent strain. This non-linear behaviour of lattice response resulting from the contact mechanics was not mentioned before in the literature. Recall that, in practice, bonding between two filaments within 3D printed lattices occurs over an area of overlap rather than at a point. This is taken up next.

7.3.2 Filaments bonded with overlap: flattened disc model

Filaments are stacked and bonded to adjacent layers due to the fabrication procedure employed to produce them. This bonding can be most simplified by an overlap between adjacent filaments. The overlap is an unavoidable structural characteristic that affect the stiffness properties, as shown in Chapters 5 and 6. Here we develop a model for the apparent Young's modulus along the stacking direction accounting for the overlap. This apparent property was previously studied by Norato and Wagoner-Johnson [30], their model consisted of the interpolation of plane stress and plane strain models of a disc under diametrical loads, the constants required for the interpolation were obtained using a geometry projection model. The model developed here, uses the plane stress response of a flat disc coupled with FEA to obtain the effective thickness of the disc required to predict the apparent Young's modulus.

When adjacent filaments are fused, the problem cannot longer be treated using contact mechanics. The elastic response is now given by the filaments being squashed at the location of overlap. The squashing of the filaments is produced by the pressure exerted by the filaments in subsequent layers. The compression of the filaments takes place locally. Therefore, it appears reasonable to propose a model based on the plane stress compression of a disc. The end-view of a filament, appearing as circle, between two filaments appearing as two sets of lines above and below the central filament, is shown in figure 7.6(a). Recall that the overlap is defined here as $OL = (2r - \lambda_z/2)/2r$. Note that the overlap OL becomes 0 when $\lambda_z/2 = 2r$, when $\lambda_z/2 < 2r$ the analysis is approximated

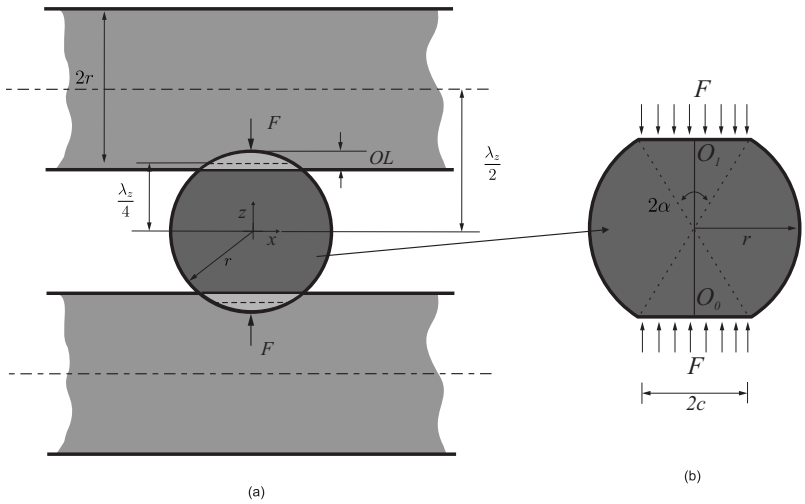

FIGURE 7.6: Schematics of (a) the cross-section of a filament between adjacent filaments and (b) the geometry of the flattened disc used to model the elastic compression.

to the case of a flattened disc under the action of the resultant force F as shown in figure 7.6(b). The vertical location of the flat overlap interface is approximately taken midway between the centre-to-centre distance between the two overlapping cylinders. This is a distance $\lambda_z/4$, since the centre-to-centre distance is $\lambda_z/2$ (see figure 7.6(b)). The expression for the elastic displacement w for the flattened end in a disc was derived by Wang et al. [113] as,

$$w = \frac{2F}{\pi E \langle t \rangle} \left\{ (1-\nu) - \ln\left(1 + \frac{4}{\sin^2(\alpha)}\right) \right\} \frac{\alpha}{\sin(\alpha)}. \tag{7.24}$$

where $\langle t \rangle$ is the thickness of the disc, and $\sin(\alpha) = 2c/2r$, having $2c$ as the width of the flat end. Equation (7.24) tends infinity when α tends to 0. This asymptotic behaviour was addressed in the previous section with the contact model presented. The vertical line O_0O_1 shown in figure 7.6(b) has an original length equal to $2r\cos(\alpha)$, so that using equation (7.24) the apparent strain $\langle \varepsilon \rangle$ can be define as the change of length w over the original of the dimension O_0O_1 as,

$$\langle \varepsilon \rangle = \frac{w}{2r\cos(\alpha)} \tag{7.25}$$

The apparent stress is again $\langle \sigma \rangle = F/\lambda^2$, so the apparent Young's modulus is obtained as $\langle E \rangle_a = \langle \sigma \rangle / \langle \varepsilon \rangle$. The model is coupled with FEA computations to determine the effective thickness $\langle t \rangle$ to be considered in the model proposed. A schematic diagram of

the apparent $\langle t \rangle$ is depicted in figure 7.7, where it is represented by the shaded section of the filament. This is determined numerically in the following section.

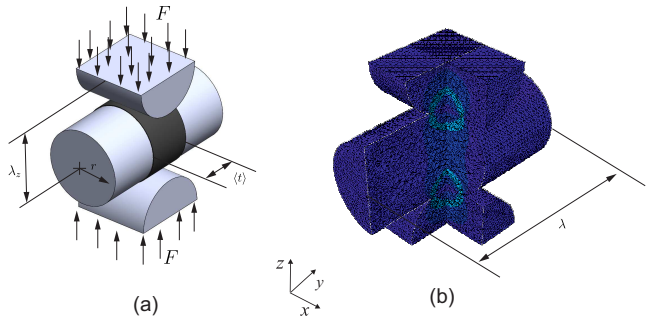

FIGURE 7.7: (a) Schematic of a section of the lattice under the action of load F. The shaded section of the filament represents the effective thickness $\langle t \rangle$. (b) The deformed shape obtained from the FEA model.

7.4 Results and discussions

Finite element model

The analytical results obtained in this chapter are reconciled with computation using finite element software Abaqus/CAE/Standard 6.13® (Simulia, Dassault Systmes, Providence, RI, USA). The filaments were modelled as cylinders and meshed using tetrahedral elements C3D10; the bonding between them was modelled by considering an overlap in the volumes of adjacent cylinders. The diameter of the cylinders was used as $2r = 0.5$ mm (this was deliberately chosen as a common size for FFF nozzles is 0.5 mm), while the rest of the parameters such as separation between filaments λ, were changed systematically to study their influence in the apparent properties. By changing λ, porous lattices of varying relative density $\bar{\rho}$ were simulated. The material properties used correspond to those for PLA, i.e. $E = 2290$ MPa (data measured from tensile tests on single FFF-filaments Chapter 4), and the Poisson's ratio $\nu = 0.36$ [101].

7.4.1 Lattices with staggered stack of filaments

Finite element modelling of the symmetric staggered arrangement

The deformed shape obtained from the FEA computations of the staggered lattice under compressive loading is presented in figure 7.8. A single unit cell was extracted from the deformed model and is shown separately in the magnified view. Note a clear bending deformation of the filaments lying horizontally. The distance between the cylinders λ was varied, in order to observe the relation between the apparent property $\langle E \rangle_s$ and the relative density $\bar{\rho}$. Various unit cells, like the one shown in figure 7.8, were modelled a subjected to compressive forces. In each simulation, a rigid plate (infinite stiffness), was tied to the nodes on the top surface. The compressive load was applied on this plate, so it is uniformly distributed on all the nodes of the top surface. The nodes on the bottom surface were constrained in all DoF, while due to periodicity of the structure, all the nodes lying in the vertical surfaces were constrained to remain in their plane, allowing the vertical displacement. The apparent Young's modulus is calculated by dividing the total force applied by the area of the unit cell $A = \lambda^2$, while the resulting deflection was divided by the original length of the unit cell $\approx 8r$. The values for various apparent Young's modulii calculated from simulations are plotted as function of the relative density in figure 7.9. Note that the apparent property scales $\langle E \rangle_s \sim \bar{\rho}^5$ as expected from the analytical model equation (7.4). This is reflected in a straight line with slope equal to 5 in the log-log plot 7.9. The scaling relation for the apparent Young's modulus obtained with Timoshenko shear correction scaled with relative density as $\langle E \rangle_s \sim \bar{\rho}^{4.8}$, while the FEA results scaled $\langle E \rangle_s \sim \bar{\rho}^{4.7}$. In figure 7.9, results for the apparent Young's modulus obtained from the analytical model is compared with those obtained from FEA showing excellent agreement for lattice with high porosity. Lattices with low relative density have separations between filaments that make them relatively long compared with the radius of the filaments. As the $\bar{\rho}$ increases, the ratio r/λ increases resulting in short and thick filaments, where the beam theories are not appropriate. Inclusion of shear significantly improves the agreement between numerically obtained results and the analytical model.

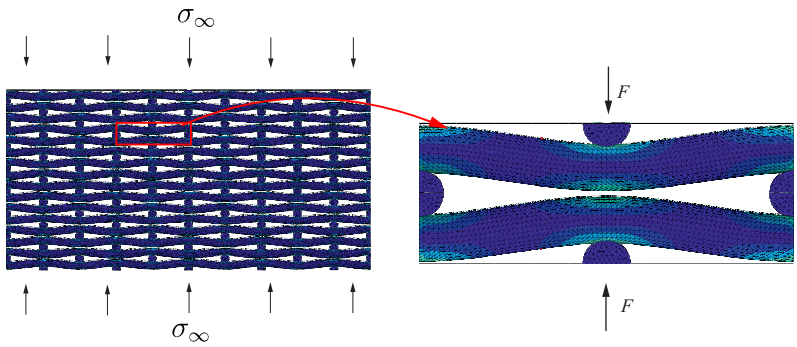

FIGURE 7.8: Deformed shapes obtained from the computational experiments of the staggered arrangement and the unit cell used for the comparison with the analytical model. Note that the deformed shapes have been scaled so that the deformation becomes visually accesible.

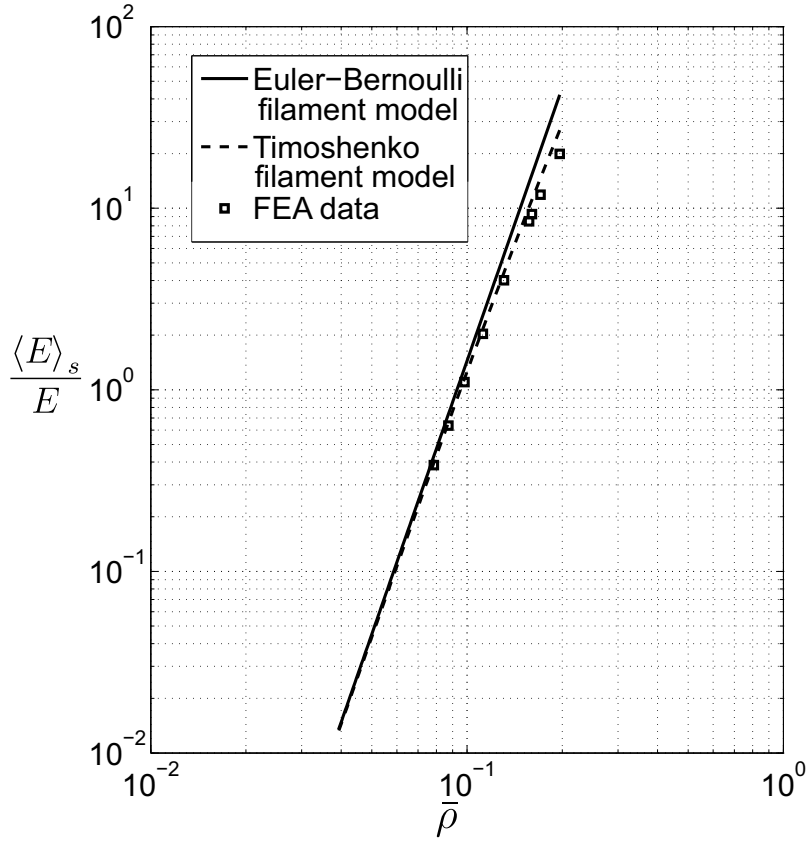

FIGURE 7.9: Comparison of the predicted value using the analytical models developed and the FEA results for the Apparent Young's modulus $\langle E \rangle_s$ as function of the relative density. Both the models using Euler-Bernoulli and Timoshenko theories for the filament flexure are presented.

Complete displacement of a given periodic beam

We plotted the complete displacement of a periodic beam in figure 7.10, the beam is made of PLA having the Young's modulus $E = 2290$ MPa, an overhang of $\lambda = 10$ mm, a circular cross-section with radius $r = 0.5$, and it is subjected to a force $F = 1$ N. We

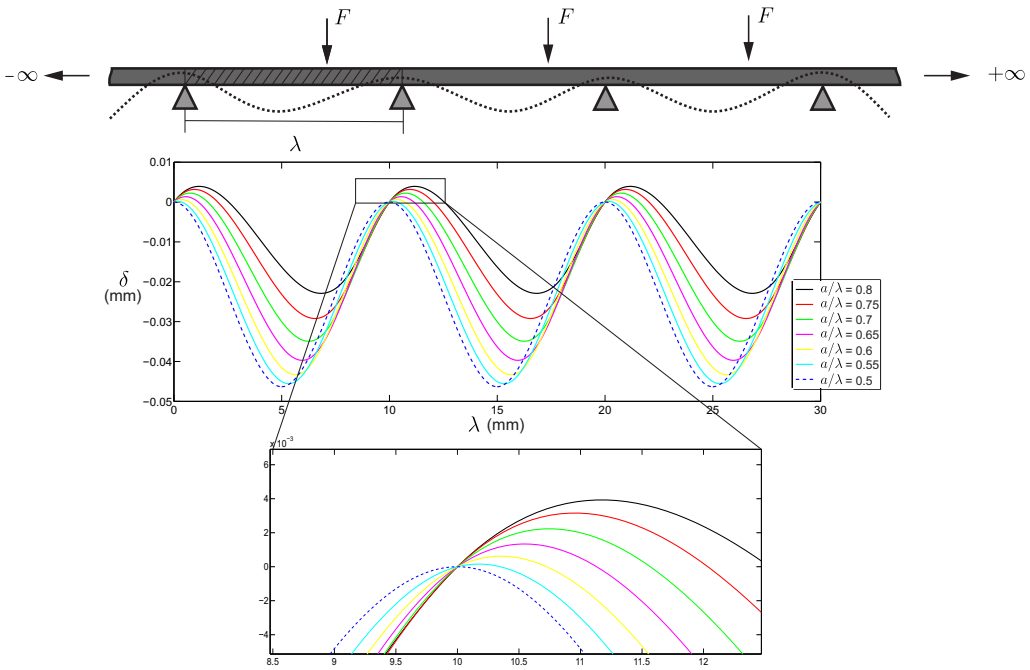

FIGURE 7.10: Deflection curves for several values of a. Note that the non-zero slope at the supports. Note also, that the the maximum displacement of the curves is not at the point of force application, except for the symmetric case $a/\lambda = 0.5$.

used the solution of equation (7.15) to calculate coefficients in the cubic transverse displacement profiles observed in equations (7.7). Deflected shapes for different positions for the points where the force is applied were plotted. Note the zoomed view of displacements at one of the supports, showing the increment in the slope as the force is being applied further away from the mid-point of the overhang. Also note, that the maximum displacement is obtained for the $a/\lambda = 0.5$, which is the softest response of the woodpile. For the configuration where $a/\lambda = 0.5$, the location of the maximum displacement is coincident with force application point. On the other hand, the maximum displacement for the asymmetric configuration is not at the point where the force in being applied.

Finite element modelling of the asymmetric staggered arrangement

Woodpiles as shown in figure 7.11(a) were subjected to compressive loading. The structures were composed of filaments with diameters of $2r = 1$ mm, and the overhang between filaments was of $\lambda = 10$ mm. The arrangements were such that filaments do not lie at the mid-point of the overhang. This location was controlled using the parameter a, which is defined as length from the left filament to the location of the staggered

filament. The lattice shown in figure 7.11 corresponds to the ratio $a/\lambda = 0.7$. The compressive force was divided by the apparent area to obtain the apparent stress $\langle\sigma\rangle$. The resulting displacement was divided by the total height of the woodpile to obtain the strain ε. The apparent Young's modulus obtained from the FEA data was compared against the predicted trends calculated using the expression (7.18). The comparison is presented in figure 7.12. The importance of the correct slope continuity at the supports is brought out in figure 7.12 where three trends correspond to three different boundary conditions for the unit cell of the a periodic beam. The top dotted line corresponds to an analytical model developed under the assumption that the filaments at the supports have slopes equal to zero. The bottom dotted line corresponds to an analytical model developed under the assumptions pinned supports at the ends. The solid line corresponds to the model based on the periodic beam, developed in Section 7.2. The agreement between the periodic beam model and the FEA data validates the correct boundary conditions used to develop the model. The dotted lines in figure 7.12 are the upper and the lower bounds for the apparent Young's modulus. The correct response lies between these two, and thus predicted with the model developed in Section 7.2. The non-zero slope at the support filaments is observed in figure 7.11(b). Zero slope in the deformation of the filaments will result in red lines that are completely horizontal, note that this is not the case in figure 7.11(b).

The lowest value for $\langle E\rangle_s$ in figure 7.12 corresponds to the symmetric staggered configuration corresponding to $a/\lambda = 0.5$. As expected $\langle E\rangle_s$ increases as the ratio a/λ approaches to 1. Equation (7.18) is sigular when $a/\lambda = 1$, as this case corresponds to the aligned case, and the analysis of the elastic response is significantly different. Results and discussions for the aligned configuration corresponding to $a/\lambda = 0$ or $a/\lambda = 1$ are presented next.

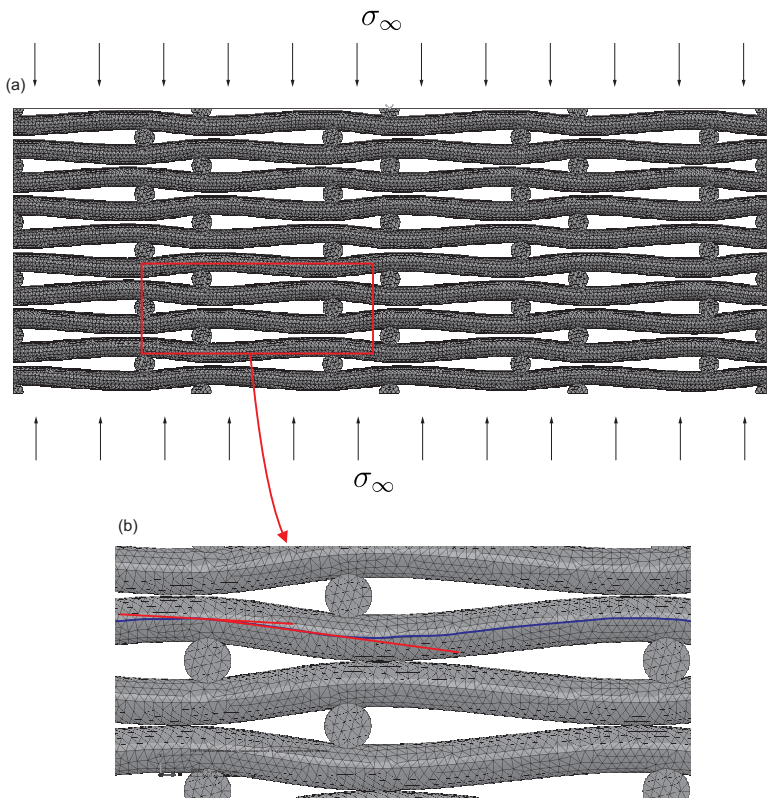

FIGURE 7.11: Deformed shape obtained from the FEA model, showing the deflection of the filaments. Note the non-zero slope at the supports and load application point indicated with red lines in the zoomed figure.

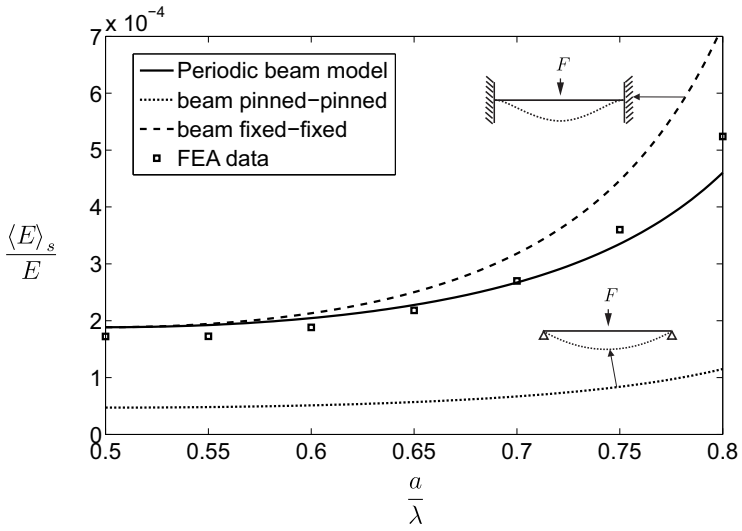

FIGURE 7.12: Curve showing the relation between the apparent Young's modulus and the relative position of the filaments in the staggered configuration.

7.4.2 Lattices with aligned stack of filaments

Two idealisations are considered here–first when the filaments are bonded at a single point and second when they adhere over a patch.

Filaments bonded at one point: pure contact

The model proposed in Section 7.3.1, where the filaments are bonded at a single point was validated against FEA simulations. The deformed shape and the stress patterns obtained from the computations of the aligned arrangement are shown in figure 7.13, an arbitrary unit cell is extracted to show the deformation. The lattice parameters are $\lambda = 2$ mm, $r = 0.5$ mm, and $\lambda_z/2 = 2r$ (pure contact case). A point contact that ties the displacement (*non-friction interaction* option in the FE software) between the surfaces of the adjacent cylinders was specified. The force was applied on a rigid surface attached to the top nodes of the model, and the total deformation in the vertical axis obtained. The nodes at the bottom surface were constrained in all DoF, while the nodes in the side surfaces were constrained to remain in the plane. The force-displacement curve was obtained from the computational experiments and then scaled to apparent stress-apparent strain. The force was divided by the area of the unit cell equal to λ^2, and the displacement by original length of the unit cell in the stacking direction $4r$. The comparison exhibits good agreement and it is shown in figure 7.14.

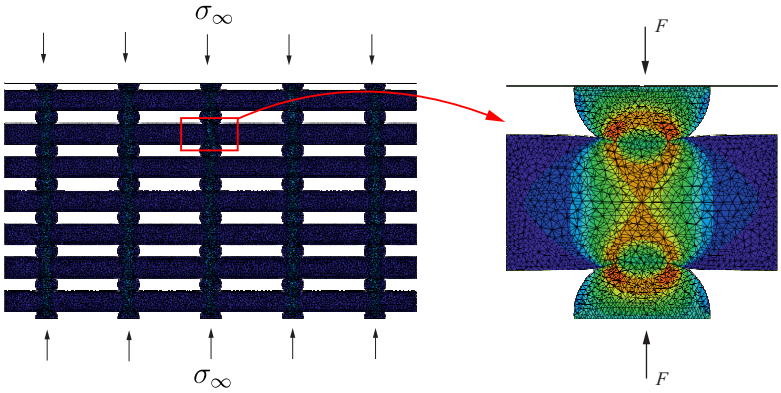

FIGURE 7.13: Deformed shapes from the computational experiments of the aligned arrangement and the unit cell used for the comparison with the analytical model.

Filaments bonded over an overlap

The sensitivity to overlap was studied with a similar unit cell as the one employed in the previous section. The difference now is that the distance from centre-to-centre of the filaments is $\lambda_z/2 < 2r$. This parameter will result in an overlap between the cylinders. First various simulations were carried out on unit cells with cylinders of diameter $2r =$

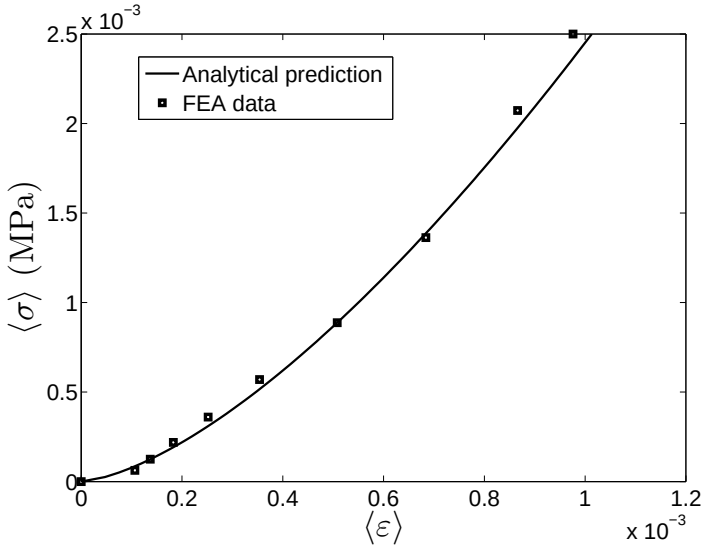

FIGURE 7.14: Non-linear relationship between the apparent stress and the apparent strain for the aligned configuration with filaments bonded at a single point.

0.5 mm, different values of λ and λ_z. Changes in these parameters changed the relative density $\bar{\rho}$ and overlap, respectively. The boundary conditions employed were those described in the previous section. The apparent stress $\langle\sigma\rangle$ was obtained by dividing the total force applied over the area of the unit cell λ^2. The apparent strain $\langle\varepsilon\rangle$ was obtained using the deformation in the vertical axis obtained from the simulation and equation (7.24). The apparent Young's modulus was calculated using $\langle E\rangle_a = \langle\sigma\rangle/\langle\varepsilon\rangle$. The results were employed with model developed in Section 7.3.2 to obtain the effective thickness $\langle t\rangle$ required for this model to match the FEA results. These results allow us to plot the effective thickness $\langle t\rangle$ against the overlap. The relation is presented in figure 7.15 where the apparent thickness was normalised with the diameter of the filaments. To corroborate the correctness of the curve in figure 7.15, we run a second set of computational experiments. The models consisted of a unit cell with $2r = 1$ mm, and again several separations between filaments λ and λ_z were used. The results of these computations are plotted in figure 7.16, using different symbols for different values of OL. An excellent agreement is observed between the semi-analytical model and the FEA simulations.

Figure 7.16 shows that as OL increases, $\langle E\rangle_a$ increases for lattices having the same parameters r and λ. This is explained because an increase in OL increases the area

of the flattened section corresponding to the filament at the joints. This makes the so-called flattened disc, shorter and therefore stiffer to the compressive loadings. The series of simulations presented in this section exhibit the sensitivity of the apparent Young's modulus for the aligned configuration to the bonding between filaments. Making this apparent property not only dependent of the architecture or structural parameters such as r and λ, but also to the manner in which the filaments are joint.

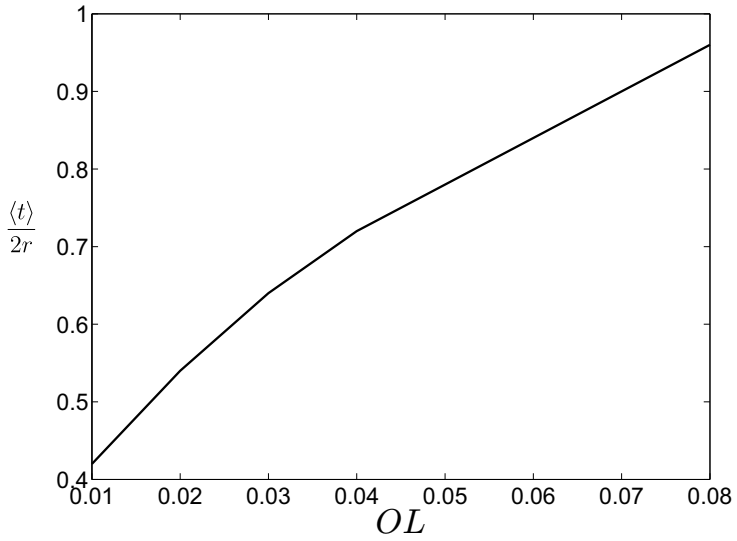

FIGURE 7.15: The fraction of apparent thickness over the diameter of the filaments as function of the Overlap. This relation is used to complete the analytical model proposed in order to be able to fully predict the apparent Young's modulus.

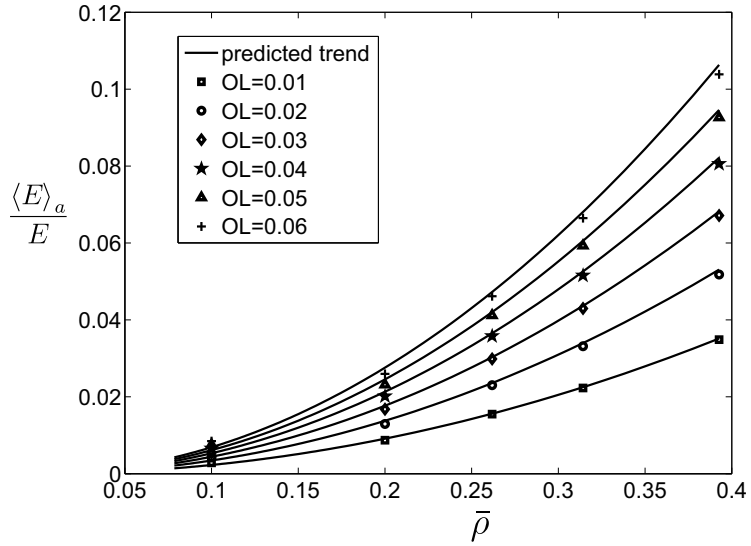

FIGURE 7.16: Apparent Young's modulus as function of the relative density for different overlaps.

7.5 Conclusions

The stiffness of woodpile lattices along the stacking direction of two arrangements of the woodpile was studied. The difference in stiffness of the structure for these two arrangements was studied using analytical models based on a periodic beam theory to describe the filament mechanics. The computational results were compared against analytical predictions. When a woodpile structure with staggered filaments is loaded remotely, the filaments predominantly experience bending. On the other hand, when a structure with aligned woodpile configuration is loaded, the response is dominated by local elastic deformations close to the region of fibre adhesion. The fundamental micromechanics of the filaments enabled us to develop analytical expressions to for the apparent structure-property relationship.

The dependence of the apparent Young's modulus with respect to changes in the position of the filaments in the woodpile was brought out. Symmetric and asymmetric staggered configurations were studied. The apparent Young's modulus based on a periodic beam theory for filaments showed a scaling relation with the volume fraction as $\langle E \rangle_s \sim \bar{\rho}^5$. The upper and lower bounds of the apparent Young's modulus were identified to be for fixed-fixed and pined-pined boundary conditions at the beam supports. Results from the analytical models developed here were validated against FEA computations, showing excellent agreement.

Structures in the aligned configuration show a strong dependence on the overlap between filaments. A simple model based on the point contact between cylindrical filaments was developed. The apparent Young's modulus showed a non-linearity due to the contact mechanics involved. The apparent Young's modulus of aligned configuration with filament overlapping was studied analytically and numerically. The model developed was based on the elastic compression of a flatten disc. An increment in the apparent stiffness was observed as the fraction of overlap increases.

For the same volume fraction structures with the aligned configuration are stiffer, than that with the staggered arrangement. The latter case is softer as it is bending-dominated.

Woodpile lattices with the staggered arrangement more suitable for applications of energy absorption. On the contrary, the aligned configuration requires very high stress to achieve the same strains for the staggered arrangement. This suggests that when filaments are aligned, the lattice material is suited for high stiffness applications.

Chapter 8

Conclusions and future work

Conclusions were presented at the end of each chapter. Here we summarise them in the broader perspective of the mechanics of 3D printed lattice materials. Further we present new research possibilities for the future.

8.1 General conclusions

The apparent elastic properties of 3D printed material in the woodpile arrangement were studied within this dissertation. The woodpile lattice studied is composed of alternating stack of filaments orthogonally oriented. This arrangement is commonly found in parts fabricated using fused filament fabrication. A methodology to print bespoke lattice structures using FFF was successfully implemented. The methodology was used to produce FFF-parts with controlled structural parameters, which, in turn, will allow tailoring mechanical properties. Several samples for mechanical testing were fabricated using this methodology. The structure-property relationship of woodpile lattice materials was successfully studied with analytical models and experimental characterisation. These brought out important aspects of the micromechanics involved in various loading scenarios. The models and analysis developed in this research work provide the basis for the understanding of the apparent mechanical properties of 3D printed materials and strucutres bye means of simple but robust mechanics and new scaling relationships.

When the lattice is loaded along one of the filament axes, the elastic response was shown to be dominated by the elongation or compression of the filaments parallel to the loading direction. An expression for the apparent Young's modulus of elasticity was developed. It shows a linear scaling relation with the volume fraction. For high porosity the Young's modulus equals half of the modulus of the filament material for square lattices. Computational and laboratory experiments on FFF-fabricated samples were used to validate this. The computationally obtained apparent Young's modulus is in excellent agreement with the results of the analytical model as well as experimental measurements. The differences with the experimentally measured data are attributed to manufacturing variability and the presence of sag in the filament overhangs. The latter resulted in a slightly softer response of the real material.

The limitations of employing the apparent elastic modulus in the prediction of the transverse deflection of woodpile beams were brought out. Unlike solid homogeneous beams, where the shear deformations are included as a mere *correction*, for woodpile beams, this is highly significant. When the lattice is relatively porous and the beam relatively short, ignoring lattice shear leads to huge errors and therefore, its importance is much more significant than for solid non-porous structures. Expressions for apparent bending stiffness and the apparent shear stiffness were developed for two configurations of the woodpile–first when the alternating layers are aligned and when they are staggered. It was shown that the bending stiffness is independent of these two configurations whereas the shear stiffness shows strong differences. For the same porosity, the staggered arrangement is approximately four times stiffer in shear. The apparent shear stiffness is dominated by the bending of the filaments. This mechanism of deformation was successfully employed in the development of an analytical expression. A shear inclusive model was developed to predict the transverse deflection of woodpile beams. The results obtained from the analytical model were validated against FEA simulations. The apparent bending stiffness expression was also compared with laboratory experiments. FFF-samples were tested in three-point bending, and response in the elastic region was accurately predicted.

Torsional stiffness of lattice rods was studied analytically, computationally and experimentally. A crucial aspect in the apparent torsional stiffness of woodpile structures is the adhesion between filaments. A sensitivity analysis carried out here shows these huge differences that can be obtained in the apparent torsional stiffness because of differences in the area of overlap between adhering filaments. Models were developed assuming two different types of adhesion and taking the filament deformation mechanisms into account. The primary deformation mechanisms identified were twist and flexure of the filaments. The first model assumes the filaments are bonded at a point, allowing rotation with respect to each other. When this is the case, the filaments bend from one end to the other of the woodpile bar. The second model assumes the filaments are welded, restricting the relative displacement as well as the rotation; the filaments now bend at each overhang between consecutive supporting filaments. When the filaments are welded, the torsional stiffness is primarily governed by the apparent shear modulus of the lattice. This apparent shear modulus is in turned dominated by the bending of the filaments. However, significant filament shear contributions were also observed when the filament spacing is small to moderate. The torque-twist response of FFF-samples was accurately predicted using the expression that assumes filaments are welded at the joints.

Elastic compression in the direction of stacking was studied next. Different distributions of the filaments produce material arrangements with different mechanisms of deformation. Two structural examples were considered that highlight these significant differences. The elasticity of the lattices with staggered arrangement is dominated by the filaments in flexure, while that in the aligned configuration is governed by local elastic deformation at the filament bonding locations. Hence, for the same volume fraction, the staggered configuration is significantly softer. Analytical expressions were developed on the basis of beam bending theories for the staggered configurations. Symmetric and asymmetric staggered arrangements were considered. Lattices with symmetric staggered distribution of filaments are softer than those with asymmetric arrangement. In a symmetric arrangement, the filaments are located at the mid-point of the overhang between supporting filaments, making them very soft in flexure. Analytical models developed here were compared with FEA computations showing good agreement.

The sensitivity of the apparent elasticity to the overlap factor in elastic compression of the woodpile with aligned filaments was studied. Two models were proposed; the first is one of point contact between filaments and the second where the filaments overlap. The case of point contact showed a non-linear stiffness due to the contact mechanics deformation involved in the response. The inclusion of overlap between filaments increases the apparent stiffness of the woodpile. The apparent Young's modulus for the woodpile lattice with overlapping filaments was predicted analytically and numerically, with a model based on the elastic compression of a flattened disc. The models results were reconciled with FEA computations, showing good agreement.

The main contributions of this thesis are the following:

- A manufacturing procedure to fabricate bespoke lattices with controlled porosity using FFF (Chapter 3) was developed. This procedure has open new research opportunities, by enabling to produce lattices other than the square woodpile studied here.
- The mechanical properties of slender FFF-parts in flexural and torsional tests are presented here for the first time (Chapters 5 and 6). These brought out interesting characteristics of the deformation mechanisms of FFF-parts to more practical loadings such as beams in bending and torsion.
- For dense and long woodpile beams, the apparent Young's modulus was successfully employed to predict the transverse deflection. For porous and short beams, a novel shear inclusive model was developed (Chapter 5). Analytical models for the apparent bending and shear moduli were presented for the first time in this dissertation.
- Analytical and numerical models were developed for the apparent shear modulus and apparent Young's modulus along the stacking direction (Chapters 5 and 7). The elastic properties of lattices in the staggered arrangement of filaments were studied for the first time and accurate predictive models were successfully developed.

- The torsional properties of woodpile bars were studied for the first time in this dissertation. The deformation mechanisms in woodpile bars undergoing twist were presented in Chapter 6. Analytical models to predict the apparent torsional stiffness of a bundle of filaments, and woodpile bars were also developed successfully for the first time.
- A sensitivity study to show the dependence of the apparent properties studied to the overlap was carried.

8.2 Future work

There are several aspects of the mechanics of the woodpile architecture that require further study or that are open issues. These are itemised below:

- Experimental characterisation of slender samples made of the staggered arrangement. The models presented here were validated with computational simulations using FEA.
- Laboratory experiments on the compression along the stacking axis for the aligned configuration. The models proposed here were validated computationally.
- Laboratory characterisation of the overlap sensitiveness is still an open issue. The FEA models exposed the change in apparent stiffness as function of the overlap.
- The above item suggests that a manufacturing adaptation to control the overlap fraction between adjacent filaments is required to have full control on the apparent properties of the woodpile lattice.
- This dissertation only covered the $[0°/90°]$ stacking of filaments. The study of different orientations of the woodpile are still open issues. Markedly different properties are expected for different orientations. Anisotropy needs to be fully characterised. An initial attempt to study this has been looking at. The procedure is based on the rotation of the stiffness matrix, as it has been used previously for composite materials. Woodpile lattices with different orientations of the filaments can be studied with this method. Research on this in currently underway.

- Lattices that have been produced with the manufacturing procedure developed are: functionally graded woodpile lattices, honeycombs, among others. The mechanical characterisation of these is underway.

- The present thesis characterises the apparent elastic properties of the woodpile lattice for static problems, the plastic, strength and dynamics properties of the lattice are still an open issue. An attempt to study the failure, fracture and strength of woodpile lattice materials could make use of statistical tools such as Monte Carlo, incorporated along with simple mode I fracture mechanics models. All this when the woodpile lattice is loaded a long the filaments direction.

- Slender samples of lattice structures manufactured using FFF process were studied here. This could be extended for many practical situations where beams and rods are stubby rather than thin and long. This would require careful consideration to lattice shear, for example, while dealing with bending of such lattice bars.

Appendix A

G-code Generator

The following code is used to generate the *Gcode* for the RepRap machine.

```
%--------------------------------------------------------------------------
%                Gcode Generator
%Author: Enrique Cuan Urquizo
%Description: The following code uses as inputs the number of struts in the
%X and Y axes, the number of layers in the Zaxis and the separation
%between the struts. The code gives as output a .Gcode file ready to use in
%the RepRap machine.
%--------------------------------------------------------------------------

address=strcat('\\soton.ac.uk\ude\PersonalFiles\Users\ecu1g12.....',
'example','.gcode');

%Printing of the first lines of the gcode corresponding to the
%inicialization manufacturing parameters
E=1.00000;
Ei=1.00000;
fid = fopen(Direccion,'wt');
fprintf(fid,'M190 S70 ; wait for bed temperature to be reached\n');
```

```
fprintf(fid,'M104 S210 ; set temperature\n');
fprintf(fid,'G28 ; home all axes\n');
fprintf(fid,'G92 E0  ;reset extruder\n');
fprintf(fid,'G1 E3 F1200 ;Prime extruder 3mm\n');
fprintf(fid,'G1 E2 F1200 ;retract extruder 1mm\n');
fprintf(fid,'G92 E0  ;reset extruder\n');
fprintf(fid,'M109 S210 ; wait for temperature to be reached\n');
fprintf(fid,'G90 ; use absolute coordinates\n');
fprintf(fid,'G21 ; set units to millimeters\n');
fprintf(fid,'G92 E0\n');
fprintf(fid,'M82 ; use absolute distances for extrusion\n');
%separation in X
sx=1.0;
%separation in Y
sy=2.0;
%# of fibers in x and y - axes
nx=31; ny=12;
%# of layers in the z axis
nz=1;
%Position vectors inicialization
x=zeros(1,ny); y=zeros(1,nx);
%points generator
x(1)=90; y(1)=62; yi=y(1); xi=x(1);
zi=0.3;
for i=1:ny-1
   x(i+1)=x(i)+sy;
end
for i=1:nx-1
  y(i+1)=y(i)+sx;
end
j=1;
```

```
fprintf(fid,'G1 F1800.000 E-1.00000\n');
fprintf(fid,'G1 Z0.600 F7800.000\n');
fprintf(fid,'G92 E0\n');
fprintf(fid,'G1 X%0.5f',xi-8.0);
fprintf(fid,' Y%0.5f\n',yi-8.0);
fprintf(fid,'G1 Z0.300\n');
fprintf(fid,'G1 F1800.000 E1.00000\n');
e=1;
%intial movements to ensure the proper extrusion of the material
fprintf(fid,'G1 X%0.5f',xi-10.0);
fprintf(fid,' Y%0.5f',yi-10.0);
fprintf(fid,' E%0.6f\n',e);
fprintf(fid,'G1 X%0.5f',max(x)+10.0);
fprintf(fid,' Y%0.5f',yi-10.0);
e=e+(sqrt((((xi-10)-(max(x)+10))^2)+(((yi-10)-(yi-10))^2))/36)+0.5;
fprintf(fid,' E%0.6f\n',e);
fprintf(fid,'G1 X%0.5f',max(x)+10.0);
fprintf(fid,' Y%0.5f',max(y)+10.0);
e=e+(sqrt((((max(x)+10)-(max(x)+10))^2)+(((yi-10)-(max(y)+10))^2))/36);
fprintf(fid,' E%0.6f\n',e);
fprintf(fid,'G1 X%0.5f',xi-10.0);
fprintf(fid,' Y%0.5f',max(y)+10.0);
e=e+(sqrt((((max(x)+10)-(xi-10))^2)+(((max(y)+10)-(max(y)+10))^2))/36);
fprintf(fid,' E%0.6f\n',e);
fprintf(fid,'G1 X%0.5f',xi-10.0);
fprintf(fid,' Y%0.5f',yi-6);
e=e+(sqrt((((xi-10.0)-(xi-10.0))^2)+(((max(y)+10.0)-(yi-6.0))^2))/36);
fprintf(fid,' E%0.6f\n',e);
fprintf(fid,'G1 F1800.000 E%0.6f\n',e-1);
fprintf(fid,'G1 Z0.600 F7800.000\n');
fprintf(fid,'G92 E0\n');
```

Appendix B

G-code obtained

This appendix presents the resulting *.Gcode* obtained from the code presented in Appendix A.

```
M190 S70 ; wait for bed temperature to be reached
M104 S210 ; set temperature
G28 ; home all axes
G92 E0  ;reset extruder
G1 E3 F1200 ;Prime extruder 3mm
G1 E2 F1200 ;retract extruder 1mm
G92 E0  ;reset extruder
M109 S210 ; wait for temperature to be reached
G90 ; use absolute coordinates
G21 ; set units to millimeters
G92 E0
M82 ; use absolute distances for extrusion
G1 F1800.000 E-1.00000
G1 Z0.600 F7800.000
G92 E0
G1 X82.00000 Y54.00000
```

```
G1 Z0.300
G1 F1800.000 E1.00000
G1 X80.00000 Y52.00000 E1.000000
G1 X122.00000 Y52.00000 E2.666667
G1 X122.00000 Y102.00000 E4.055556
G1 X80.00000 Y102.00000 E5.222222
G1 X80.00000 Y56.00000 E6.500000
G1 F1800.000 E5.500000
G1 Z0.600 F7800.000
G92 E0
G1 Z0.300
G1 F1800.000
G1 X90 Y62
G1 Z0.600 F1800.00 E1.00000
G92 E0
G1 X90.0 Y62.0 Z0.300
G1 F300.00 E1.00000
G1 X112.0 Y62.0 E1.611111
G1 X112.0 Y63.0 E1.638889
G1 X90.0 Y63.0 E2.250000
G1 X90.0 Y64.0 E2.277778
G1 X112.0 Y64.0 E2.888889
G1 X112.0 Y65.0 E2.916667
G1 X90.0 Y65.0 E3.527778
G1 X90.0 Y66.0 E3.555556
...
```

Appendix C

Complete solution for the displacement of the periodic beam model

This appendix presents the solution to all the unknowns of the system of equations obtained in Section 7.2. Recall the system is in the form

$$[\mathbf{K}]\{\mathbf{q}\} = \{\mathbf{f}\} \tag{C.1}$$

where $\{\mathbf{q}\} = \{a_0, \cdots, a_3, b_0, \cdots, b_3\}^T$, $\{\mathbf{f}\} = \{0, 0, 0, 0, 0, 0, 0, F/6EI\}^T$ and

$$[\mathbf{K}] = \begin{bmatrix} 1 & 0 & 0 & 0 & \hat{0} & 0 & 0 & 0 \\ 0 & 0 & 0 & 0 & 1 & b & b^2 & b^3 \\ 0 & 1 & 0 & 0 & 0 & -1 & -2b & -3b^2 \\ 0 & 0 & 1 & 0 & 0 & 0 & -1 & -3b \\ 1 & a & a^2 & a^3 & -1 & 0 & 0 & 0 \\ 0 & 1 & 2a & 3a^2 & 0 & -1 & 0 & 0 \\ 0 & 0 & 1 & 3a & 0 & 0 & -1 & 0 \\ 0 & 0 & 0 & 1 & 0 & 0 & 0 & -1 \end{bmatrix} \tag{C.2}$$

Using the software Mathematica to solve equation (C.1) leads to the following solutions

$$a_0 = 0 \tag{C.3a}$$

$$a_1 = \frac{\left(-a^2 b + a b^2\right) F}{12(a+b)EI} \tag{C.3b}$$

$$a_2 = \frac{abF}{4(a+b)EI} \tag{C.3c}$$

$$a_3 = -\frac{bF}{6(a+b)EI} \tag{C.3d}$$

$$b_0 = \frac{a^2 b^2 F}{12(a+b)EI} \tag{C.3e}$$

$$b_1 = -\frac{a^2 bF - a b^2 F}{12(a+b)EI} \tag{C.3f}$$

$$b_2 = -\frac{abF}{4(a+b)EI)} \tag{C.3g}$$

$$b_3 = \frac{F}{6EI} - \frac{bF}{6(a+b)EI} \tag{C.3h}$$

Bibliography

[1] Dental tribune. http://www.dental-tribune.com/articles/news/europe/17375. Accessed: 04-02-2017.

[2] P Moongkhamklang. *Titanium-silicon carbide composite lattice structures*. 2009.

[3] S. Yang. Private communication. -, 2015.

[4] L. J. Gibson and M. F. Ashby. *Cellular Solids: Structure and properties*. Cambrige University Press, second edition, 1997.

[5] FA Costa Oliveira, S Dias, M Fátima Vaz, and J Cruz Fernandes. Behaviour of open-cell cordierite foams under compression. *Journal of the European Ceramic Society*, 26(1):179–186, 2006.

[6] O Cansizoglu, D Cormier, O Harrysson, H West, and T Mahale. An evaluation of non-stochastic lattice structures fabricateed via electron beam melting. *Solid Freeform Fabrication*, pages 209–2119, 2006.

[7] Liang Hao, David Raymond, Chunze Yan, Ahmed Hussein, and Philippe Young. Design and additive manufacturing of cellular lattice structures. In *The International Conference on Advanced Research in Virtual and Rapid Prototyping (VRAP). Taylor & Francis Group, Leiria*, pages 249–254, 2011.

[8] P. Moongkhamklang, V.S. Deshpande, and H.N.G. Wadley. The compressive and shear response of titanium matrix composite lattice structures. *Acta Materialia*, 58:2822–2835, 2010.

[9] M. F. Ashby. The mechanical properties of cellular solids. *Metallurgical Transactions A*, 14A:1755–1769, 1983.

[10] HNG Wadley. Multifunctional periodic cellular metals. *Philosophical Transactions of the Royal Society of London A: Mathematical, Physical and Engineering Sciences*, 364(1838):31–68, 2006.

[11] Tim BF Woodfield, Jos Malda, J De Wijn, Fabienne Peters, Jens Riesle, and Clemens A van Blitterswijk. Design of porous scaffolds for cartilage tissue engineering using a three-dimensional fiber-deposition technique. *Biomaterials*, 25 (18):4149–4161, 2004.

[12] Makerbot. http://www.makerbot.com/blog/2013/06/26. Accessed: 21-03-2016.

[13] Michael F Ashby. *Materials selection in Mechanical Design*. Butterworth-Heinemann, 2010.

[14] J-P Kruth, Ming-Chuan Leu, and T Nakagawa. Progress in additive manufacturing and rapid prototyping. *CIRP Annals-Manufacturing Technology*, 47(2):525–540, 1998.

[15] S. Banerjee and A. Bhaskar. Free vibration of cellular structures using continuum modes. *Journal of Sound and Vibration*, 287:77–100, 2005.

[16] K. Hofstetter, C. Hellmich, and J. Eberhardsteiner. Development and experimental validation of a continuum micromechanics model for the elasticity of wood. *European Journal of Mechanics A/Solids*, 25:1030–1053, 2005.

[17] V. A. Lubarda, E. E. Novitskaya, J. McKittrick, S. G. Bodde, and P.-Y. Chen. Elastic properties of cancellous bone in terms of elastic properties of its mineral and protein phases with application to their osteoporotic degradation. *Mechanics of Materials*, 44:139–150, 2005.

[18] L. J. Gibson. Biomechanics of cellular solids. *Journal of Biomechanics*, 38:377–1–399, 2005.

[19] H. H. Bayraktar and T. M. Keaveny. Mechanisms of uniformity of yield strains for trabecular bone. *Journal of Biomechanics*, 37:1671–1678, 2004.

[20] Z. Miller and M. B. Fuchs. Effect of trabecular curvature on the stiffness of trabecular bone. *Journal of Biomechanics*, 38:1855–1864, 2005.

[21] S Yang, K-F Leong, Z Du, and C-K Chua. The design of scaffolds for use in tissue engineering. part i. traditional factors. *Tissue engineering*, 7(6):679–689, 2001.

[22] S Yang, K-F Leong, Z Du, and C-K Chua. The design of scaffolds for use in tissue engineering. part ii. rapid prototyping techniques. *Tissue engineering*, 8(1):1–11, 2002.

[23] A. Bhaskar. The effective poisson ratio of random cellular matter having bending dominated architecture. *A Letters Journal Exploring the Frontiers of Physics*, 87: 18004–p1–18004–p6, 2009.

[24] J. Zhou, A. Bhaskar, and X. Zhang. Sound transmission through a double-panel construction lined with poroelastic material in the presence of mean flow. *Journal of Sound and Vibration*, 332:3724–3734, 2013.

[25] L Lü, JYH Fuh, and Y-S Wong. Selective laser sintering. In *Laser-Induced Materials and Processes for Rapid Prototyping*, pages 89–142. Springer, 2001.

[26] PF Jacobs. *Stereolithography and other RP&M technologies: from rapid prototyping to rapid tooling*. Society of Manufacturing Engineers, 1995.

[27] Arcam AB. http://www.arcam.com/technology/electron-beam-melting/. Accessed: 21-03-2016.

[28] P. Miranda, A. Pajares, E. Saiz, A. P. Tomsia, and F. Guiberteau. Fracture modes under uniaxial compression in hydroxyapatite scaffolds fabricated by robocasting. *J. Biomedical Materials Wiley InterScience Periodicals*, 83A:646–655, 2007.

[29] P. Miranda, A. Pajares, and F. Guiberteau. Finite element modeling as a tool for predicting the fracture behavior of robocast scaffolds. *Acta Biomaterialia*, 4: 1715–1724, 2008.

[30] J. Norato and A. J. Wagoner Johnson. A computational and cellular solids approach to the stiffness-based design of bone scaffolds. *Journal of Biomechanical Engineering*, 133:091003–1–091003–7, 2011.

[31] X Lu, Y Lee, S Yang, Y Hao, J Evans, and C Parini. Extrusion freeforming of millimeter wave electromagnetic bandgap (EBG) structures. *Rapid Prototyping Journal*, 15(1):42–51, 2009.

[32] A Kruisova, H Seiner, P Sedlak, B Landa, M nad Roman-Manso, P Miranzo, and M Belmonte. Acoustic metamaterial behavior of three-dimensional periodic architectures assembled by robocasting. *Applied Physics Letters*, 105:211904–1–211904–4, 2014.

[33] E Cuan-Urquizo, S Yang, and A Bhaskar. Mechanical characterisation of additively manufactured material having lattice microstructure. *IOP Conference Series: Materials Science and Engineering*, 2014.

[34] E Cuan-Urquizo and A Bhaskar. Elastic properties of additively manufactured lattice materials: measurements and models. *Materials and Design*, manuscript in preparation, 2016.

[35] O Iyibilgin, C Yigit, and MC Leu. Experimental investigation of different cellular lattice structures manufactured by fused deposition modeling. In *Proceedings of Solid Freeform Fabrication Symposium, Austin, TX*, pages 895–907, 2012.

[36] Douglas T Queheillalt and Haydn NG Wadley. Cellular metal lattices with hollow trusses. *Acta Materialia*, 53(2):303–313, 2005.

[37] P. Miranda, A. Pajares, E. Saiz, A. P. Tomsia, and F. Guiberteau. Mechanical properties of calcium phosphate scaffolds fabricated by robocasting. *Journal of Biomedical Materials Research*, 85:218–227, 2008.

[38] S. Cahill, S. Lohfeld, and P. E. McHugh. Finite element predictions compared to experimental results for the effective modulus of bone tissue engineering scaffolds fabricated by selective laser sintering. *Journal of Materials Science: Materials in Medicine*, 20:1255–1262, 2009.

[39] N. Sudarmadji, J. Y. Tan, K. F. Leong, C. K. Chua, and Y. T. Loh. Investigation of the mechanical properties and porosity relationships in selective laser-sintered polyhedral for functionally graded scaffold. *Acta Biomaterialia*, 7:530–537, 2011.

[40] T. Serra, J. A. Planell, and M. Navarro. High-resolution pla-based composite scaffold via 3-d printing technology. *Acta Biomaterialia*, 9:5521–5530, 2013.

[41] M Suard, P Lhuissier, R Dendievel, J-J Blandin, F Vignat, and F Villeneuve. Towards stiffness prediction of cellular structures made by electron beam melting (EBM). *Powder Metallurgy*, 57(3):190–195, 2014.

[42] MR Karamooz Ravari, M Kadkhodaei, M Badrossamay, and R Rezaei. Numerical investigation on mechanical properties of cellular lattice structures fabricated by fused deposition modeling. *International Journal of Mechanical Sciences*, 88:154–161, 2014.

[43] VS Deshpande, MF Ashby, and NA Fleck. Foam topology: bending versus stretching dominated architectures. *Acta Materialia*, 49(6):1035–1040, 2001.

[44] L. J. Gibson and M. F. Ashby. The mechanics of two-dimensional cellular materials. *Proceedings of the Royal Society of London*, A382:25–42, 1982.

[45] L. J. Gibson and M. F. Ashby. The mechanics of three-dimensional cellular materials. *Proceedings of the Royal Society of London*, A382:43–59, 1982.

[46] VS Deshpande and NA Fleck. Collapse of truss core sandwich beams in 3-point bending. *International Journal of Solids and Structures*, 38(36):6275–6305, 2001.

[47] Vikram S Deshpande, Norman A Fleck, and Michael F Ashby. Effective properties of the octet-truss lattice material. *Journal of the Mechanics and Physics of Solids*, 49(8):1747–1769, 2001.

[48] JC Wallach and LJ Gibson. Mechanical behavior of a three-dimensional truss material. *International Journal of Solids and Structures*, 38(40):7181–7196, 2001.

[49] L.E. Murr, S.M. Gaytan, F. Medina, E. Martinez, J.L. Martinez, D.H. Hernandez, B.I. Machado, D.A. Ramirez, and R.B. Wicker. Characterization of ti-6al-4v open cellular foams fabricated by additive manufacturing using electron beam melting. *Material Science and Engineering A*, 527:1861–1868, 2013.

[50] J Parthasarathy, B Starly, S Raman, and A Christensen. Mechanical evaluation of porous titanium (ti6al4v) structures with electron beam melting (ebm). *Journal of the mechanical behavior of biomedical materials*, 3(3):249–259, 2010.

[51] G. Campoli, M.S. Borlefss, S. Amin Yavari, R Wauthle, H Weinans, and A.A. Zadpoor. Mechanical properties of open-cell metallic biomaterials manufactured using additive manufacturing. *Materials and Design*, 49:957–965, 2013.

[52] S McKown, Y Shen, WK Brookes, CJ Sutcliffe, WJ Cantwell, GS Langdon, GN Nurick, and MD Theobald. The quasi-static and blast loading response of lattice structures. *International Journal of Impact Engineering*, 35(8):795–810, 2008.

[53] S Naghieh, MR Karamooz Ravari, M Badrossamay, E Foroozmehr, and M Kadkhodaei. Numerical investigation of the mechanical properties of the additive manufactured bone scaffolds fabricated by fdm: The effect of layer penetration and post-heating. *Journal of the mechanical behavior of biomedical materials*, 59: 241–250, 2016.

[54] D Queheillalt, V Deshpande, and H Wadley. Truss waviness effects in cellular lattice structures. *Journal of Mechanics of Materials and Structures*, 2(9):1657–1675, 2007.

[55] P Moongkhamklang, DM Elzey, and HNG Wadley. Titanium matrix composite lattice structures. *Composites Part A: applied science and manufacturing*, 39(2): 176–187, 2008.

[56] DW Hutmacher, T Schantz, I Zein, KW Ng, SH Teoh, and K C Tan. Mechanical properties and cell cultural response of polycaprolactone scaffolds designed and fabricated via fused deposition modeling. *Journal of biomedical materials research*, 55(2):203–216, 2001.

[57] I Zein, DW Hutmacher, KC Tan, and SH Teoh. Fused deposition modeling of novel scaffold architectures for tissue engineering applications. *Biomaterials*, 23 (4):1169–1185, 2002.

[58] JM Sobral, SG Caridade, RA Sousa, JF Mano, and RL Reis. Three-dimensional plotted scaffolds with controlled pore size gradients: effect of scaffold geometry on mechanical performance and cell seeding efficiency. *Acta Biomaterialia*, 7(3): 1009–1018, 2011.

[59] M Yeo, CG Simon, and GH Kim. Effects of offset values of solid freeform fabricated pcl–β-tcp scaffolds on mechanical properties and cellular activities in bone tissue regeneration. *Journal of Materials Chemistry*, 22(40):21636–21646, 2012.

[60] FJ Martínez-Vázquez, A Pajares, F Guiberteau, and P Miranda. Effect of polymer infiltration on the flexural behavior of β-tricalcium phosphate robocast scaffolds. *Materials*, 7(5):4001–4018, 2014.

[61] X Liu, MN Rahaman, GE Hilmas, and BS Bal. Mechanical properties of bioactive glass (13-93) scaffolds fabricated by robotic deposition for structural bone repair. *Acta biomaterialia*, 9(6):7025–7034, 2013.

[62] S Eqtesadi, A Motealleh, A Pajares, F Guiberteau, and P Miranda. Improving mechanical properties of 13–93 bioactive glass robocast scaffold by poly (lactic acid) and poly (ε-caprolactone) melt infiltration. *Journal of Non-Crystalline Solids*, 432: 111–119, 2016.

[63] J.F. Rodríguez, J.P. Thomas, and J.E. Renaud. Characterization of the mesostructure of fused-deposition acrylonitrile-butadienestyrene materials. *Rapid Prototyping Journal*, 6:175–185, 2000.

[64] J.F. Rodríguez, J.P. Thomas, and J.E. Renaud. Mechanical behavior of acrylonitrile butadiene styrene (abs) fused deposition materials . experimental investigation. *Rapid Prototyping Journal*, 7:148–158, 2001.

[65] M Montero, S Roundy, D Odell, S-H Ahn, and PK Wright. Material characterization of fused deposition modeling (FDM) ABS by designed experiments. In *Proceedings of rapid prototyping and manufacturing conference, SME*, pages 1–21, 2001.

[66] S. Ahn, M. Montero, D. Odell, S. Roundy, and P.K. Wright. Anisotropic material properties of fused deposition modeling ABS. *Rapid Prototyping Journal*, 8:248–257, 2002.

[67] Anoop Kumar Sood, RK Ohdar, and SS Mahapatra. Parametric appraisal of mechanical property of fused deposition modelling processed parts. *Materials & Design*, 31(1):287–295, 2010.

[68] GC Onwubolu and F Rayegani. Characterization and optimization of mechanical properties of abs parts manufactured by the fused deposition modelling process. *International Journal of Manufacturing Engineering*, 2014, 2014.

[69] A. Bellini and S. Güçeri. Mechanical characterization of parts fabricated using fused deposition modeling. *Rapid Prototyping Journal*, 9:252–264, 2003.

[70] R Jones, P Haufe, E Sells, P Iravani, V Olliver, C Palmer, and A Bowyer. Reprap–the replicating rapid prototyper. *Robotica*, 29(01):177–191, 2011.

[71] BM Tymrak, M Kreiger, and JM Pearce. Mechanical properties of components fabricated with open-source 3-D printers under realistic environmental conditions. *Materials & Design*, 58:242–246, 2014.

[72] P. Kulkarni and D. Dutta. Deposition strategies and resulting part stiffnesses in fused deposition modeling. *Journal of Manufacturing Science and Engineering*, 121:93–103, 1999.

[73] L. Li, Q.Sun, C. Bellehumeur, and P. Gu. Composite modeling and analysis for fabrication of fdm prototypes with locally controlled properties. *Journal of Manufacturing Processes*, 4:129–141, 2002.

[74] C Casavola, A Cazzato, V Moramarco, and C Pappalettere. Orthotropic mechanical properties of fused deposition modelling parts described by classical laminate theory. *Materials & Design*, 90:453–458, 2016.

[75] CW Ziemian, RD Ziemian, and KV Haile. Characterization of stiffness degradation caused by fatigue damage of additive manufactured parts. *Materials & Design*, 109:209–218, 2016.

[76] L.C. Magalhaes, N. Volpato, and M.A. Luersen. Evaluation of stiffness and strength in fused deposition sandwich specimens. *Journal of the Brazilian Society of Mechanical Sciences and Engineering*, 36:449–459, 2014.

[77] D Croccolo, M De Agostinis, and G Olmi. Experimental characterization and analytical modelling of the mechanical behaviour of fused deposition processed parts made of ABS-M30. *Computational Materials Science*, 79:506–518, 2013.

[78] B Huang and S Singamneni. Raster angle mechanics in fused deposition modelling. *Journal of Composite Materials*, page 0021998313519153, 2014.

[79] J Wang, H Xie, Z Weng, T Senthil, and L Wu. A novel approach to improve mechanical properties of parts fabricated by fused deposition modelling. *Materials & Design*, 105:152–159, 2016.

[80] Z Weng, J Wang, T Senthil, and L Wu. Mechanical and thermal properties of ABS/montmorillonite nanocomposites for fused deposition modelling 3d printing. *Materials & Design*, 102:276–283, 2016.

[81] M Domingo-Espin, JM Puigoriol-Forcada, A-A Garcia-Granada, J Llumà, S Borros, and G Reyes. Mechanical property characterization and simulation of fused deposition modeling polycarbonate parts. *Materials & Design*, 83:670–677, 2015.

[82] Grimm T. *User's guide to rapid prototyping*. Society of Manufacturing Engineers, first edition, 2004.

[83] C.W. Hull. Apparatus for production of three-dimensional objects by stereolithography, March 11 1986. URL http://www.google.co.uk/patents/US4575330. US Patent 4,575,330.

[84] A Bowyer. Reprapproject.

[85] BM Tymrak, M Kreiger, and JM Pearce. Mechanical properties of components fabricated with open-source 3-d printers under realistic environmental conditions. *Materials & Design*, 58:242–246, 2014.

[86] R Bogue. 3D printing: the dawn of a new era in manufacturing? *Assembly Automation*, 33(4):307–311, 2013.

[87] THRE3D. https://thre3d.com/category/printers. *Consulted OnLine*, 2014.

[88] UP 3D printer. https://www.up3d.com/. Accessed: 23-03-2016.

[89] Ultimaker. https://ultimaker.com/. Accessed: 23-03-2016.

[90] GC Anzalone, C Zhang, B Wijnen, PG Sanders, and JM Pearce. A low-cost open-source metal 3-d printer. *Access, IEEE*, 1:803–810, 2013.

[91] CocoJet 3D printer. http://www.3dsystems.com/media/cocojet-3d-printer. Accessed: 23-03-2016.

[92] FPW Melchels, J Feijen, and DW Grijpma. A review on stereolithography and its applications in biomedical engineering. *Biomaterials*, 31(24):6121–6130, 2010.

[93] What is Selective Laser Sintering? http://www.livescience.com/. Accessed: 10-09-2016.

[94] A. Butscher, M. Bohner, S. Hofmann, L. Gauckler, and R. Muller. Structural and material approaches to bone tissue engineering in powder-based three-dimensional printing. *Acta Biomaterialia*, 7:907–920, 2011.

[95] K. F. Leong, C. M. Cheah, and C. K. Chua. Solid freeform fabrication of three-dimensional scaffolds for engineering replacement tissues and organs. *Biomaterials*, 24:2363–2378, 2003.

[96] T. Billiet, M. Vandenhaute, J. Schelfhout, S. Van Vlierberghe, and P. Dubruel. A review of trends and limitations in hydrogel-rapid prototyping for tissue engineering. *Biomaterials*, 33:6020–6041, 2012.

[97] Michael Montero, Shad Roundy, Dan Odell, Sung-Hoon Ahn, and Paul K Wright. Material characterization of fused deposition modeling (fdm) abs by designed experiments. In *Proceedings of Rapid Prototyping and Manufacturing Conference, SME*, 2001.

[98] A Bagsik, V Schoeppner, and E Klemp. Fdm part quality manufactured with ultem* 9085. In *14th International Scientific Conference on Polymeric Materials, September*, volume 15, 2010.

[99] A. Bagsik and V. Schoppner. Mechanical properties of fused deposition modeling parts manufactured with ultem * 9085. *ANTEC 2011 Conference Proceedings*, 2011.

[100] C. Liu, Z. Xia, and J. T. Czernuszka. Design and development of three-dimensional scaffolds for tissue engineering. *Chemical Engineering Research and Design*, 85: 1051–1064, 2007.

[101] M. Jamshidian, E. A. Tehrany, M. Imran, M. Jacquot, and S. Desobry. Poly-lactic acid: Production, applications, nanocomposites, and release studies. *Comprehensive Reviews in Food Science and Food Safety*, 9:552–571, 2010.

[102] R. Auras, L-T Lim, S. E. M. Selke, and H. Tsuji. *Poly(Lactic Acid): Synthesis, Structures, Properties, Processing, and Applications.* John Wiley & Sons, first edition, 2010.

[103] C Bellehumeur, L Li, Q Sun, and P Gu. Modeling of bond formation between polymer filaments in the fused deposition modeling process. *Journal of Manufacturing Processes*, 6(2):170–178, 2004.

[104] Q Sun, GM Rizvi, CT Bellehumeur, and P Gu. Effect of processing conditions on the bonding quality of fdm polymer filaments. *Rapid Prototyping Journal*, 14(2): 72–80, 2008.

[105] JF Rodrıguez. *Modeling the Mechanical Behavior of Fused Deposition Acrylonitrile-Butadiene-Styrene Polymer Components.* PhD thesis, Doctoral Dissertation, University of Notre Dame, Aerospace & Mechanical Engineering Department, Notre Dame, IN, 1999.

[106] Instron. Instron series 5500 load frames. *Reference Manual Equipment*, 2005.

[107] S. P. Timoshenko. On the correction of shear of the differential equation for transverse vibration of prismatic bars. 41.

[108] A. Bhaskar. Elastic waves in timoshenko beams: the lost and found of an eigenmode.

[109] JM Gere and SP Timoshenko. Mechanics of materials brooks. *Cole, Pacific Grove, CA*, pages 815–39, 2001.

[110] Instron. http://www.instron.co.uk/wa/product/8874-axialtorsion-fatigue-testing-system.aspx. *Consulted OnLine*, 2014.

[111] MJ Puttock and EG Thwaite. *Elastic compression of spheres and cylinders at point and line contact*. Commonwealth Scientific and Industrial Research Organization Melbourne, VIC, Australia, 1969.

[112] John Prescott. *Applied elasticity*. Longmans, Green and Co., 1924.

[113] QZ Wang, XM Jia, SQ Kou, ZX Zhang, and P-A Lindqvist. The flattened brazilian disc specimen used for testing elastic modulus, tensile strength and fracture toughness of brittle rocks: analytical and numerical results. *International Journal of Rock Mechanics and Mining Sciences*, 41(2):245–253, 2004.